

SUPERCONDUCTING HALF WAVE RESONATORS FOR HEAVY ION LINEAR  
ACCELERATORS

By

Jeremiah Paul Holzbauer

A DISSERTATION

Submitted to  
Michigan State University  
in partial fulfillment of the requirements  
for the degree of

DOCTOR OF PHILOSOPHY

Physics

2011

UMI Number: 3489879

All rights reserved

INFORMATION TO ALL USERS

The quality of this reproduction is dependent on the quality of the copy submitted.

In the unlikely event that the author did not send a complete manuscript and there are missing pages, these will be noted. Also, if material had to be removed, a note will indicate the deletion.



UMI 3489879

Copyright 2011 by ProQuest LLC.

All rights reserved. This edition of the work is protected against unauthorized copying under Title 17, United States Code.



ProQuest LLC.  
789 East Eisenhower Parkway  
P.O. Box 1346  
Ann Arbor, MI 48106 - 1346

## ABSTRACT

# SUPERCONDUCTING HALF WAVE RESONATORS FOR HEAVY ION LINEAR ACCELERATORS

By

**Jeremiah Paul Holzbauer**

Advanced heavy ion/rare isotope accelerators present very different challenges compared to traditional electron and proton machines. The range of particle velocities that must be accepted for a wide variety of accelerated ions implies a robust system various accelerating cavity types. The Facility for Rare Isotope Beams (FRIB) project requires such a system and research and development of new techniques and technologies to address these issues in a timely and practical manner have been undertaken at Michigan State University. While the low-energy section of the FRIB linear accelerator uses more established superconducting Quarter-Wave Resonators (QWRs), the decision was made to pursue two different types of superconducting Half-Wave Resonators (HWRs) for the high-energy accelerating section of FRIB. In this document, we begin with a brief overview of the FRIB project and its use of HWRs followed by the theory of superconducting accelerator cavities that can be applied in this context. We then present details of the process of electromagnetic and mechanical HWR design, including the theory and practice of electromagnetic and mechanical simulations. Additionally, the fabrication procedures and testing results of a prototype HWR will be presented, as well as a short discussion of the future of HWR and simulation technology.

Copyright by  
JEREMIAH PAUL HOLZBAUER  
2011

“All opinions are not equal. Some are a very great deal more robust, sophisticated and well supported in logic and argument than others.”

“The world is a thing of utter inordinate complexity and richness and strangeness that is absolutely awesome.”

“We are stuck with technology when what we really want is just stuff that works.”

-Douglas Adams

## ACKNOWLEDGMENTS

I would like to acknowledge several people who have supported me, personally and professionally, along my journey to this point.

First and foremost is my wife, Jenny, who's steady encouragement and love (even as she goes through the same struggles) has not only made the work easier, but has also made me a better man in the process. I would also like to thank my parents, their love and support helped form the core of who I am today.

Next are my advisors who spent tremendous time and effort making me the physicist I am today. First is Walter Hartung, who taught me almost everything I know about our chosen field. Second is Michael J. Syphers, who's leap of faith has turned out better than, I believe, either one of us could have expected.

Lastly, I want to thank all the people who I worked with who taught me all the little things that only get noticed if they aren't there, especially Jon Wlodarczak, John Popielarski, and Lee Harle.

# TABLE OF CONTENTS

List of Tables . . . . .	x
List of Figures . . . . .	xi
Key to Symbols and Abbreviations . . . . .	xvii
<b>1 Particle Accelerators and Nuclear Physics</b>	<b>1</b>
1.1 The Origins of Nuclear Physics . . . . .	2
1.2 Atoms as a Probe . . . . .	3
1.3 Rutherford’s Address to the Royal Society . . . . .	4
1.4 Electrostatic Accelerators . . . . .	5
1.5 The Radio-Frequency Revolution . . . . .	6
1.6 The Chart of the Nuclides . . . . .	8
1.7 Rare Isotope Production . . . . .	10
1.8 Seeking the Answers to Fundamental Questions . . . . .	11
1.9 The Benefits of Understanding . . . . .	12
1.10 Purpose of Research . . . . .	12
<b>2 The Physics of Particle Accelerators</b>	<b>14</b>
2.1 The Basic Structure of a Particle Accelerator . . . . .	14
2.1.1 Charged Particle Source . . . . .	15
2.1.2 Acceleration Mechanism . . . . .	16
2.1.3 Particle Transportation and Confinement . . . . .	17
2.1.4 Subsystems . . . . .	17
2.2 Resonator Theory . . . . .	19
2.2.1 The Ideal Harmonic Oscillator . . . . .	20
2.2.2 The Driven, Damped Harmonic Oscillator . . . . .	20
2.2.3 Oscillator Behavior Near Resonance . . . . .	22
2.2.4 Special Case: The Duffing Equation . . . . .	25
2.2.5 Electromagnetic Fields as a Harmonic Oscillator . . . . .	27
2.3 A Simple Electromagnetic Resonator - The Pillbox Cavity . . . . .	30
2.3.1 Cylindrical Waveguide Modes . . . . .	31
2.3.2 From Traveling Waves to Standing Waves . . . . .	33
2.3.3 The “Fundamental Mode” and its Properties . . . . .	35
2.3.4 The Interaction of Conductors and Electromagnetic Fields . . . . .	36
2.3.5 Cavity Figures of Merit - Accelerating Voltage . . . . .	38
2.3.6 Cavity Figures of Merit - Transit Time Factor . . . . .	39

2.3.7	Cavity Figures of Merit - Peak Surface Electric and Magnetic Field . . . . .	42
2.3.8	Cavity Figures of Merit - Geometry and Quality Factor . . . . .	43
2.3.9	Cavity Figures of Merit - R/Q . . . . .	46
2.3.10	Pillbox Cavities for Low Velocity Particles . . . . .	46
2.4	Coaxial Resonators . . . . .	47
2.4.1	Coaxial Transmission Line Geometry . . . . .	48
2.4.2	The Ideal Quarter Wave Resonator . . . . .	49
2.4.3	The Ideal Half Wave Resonator . . . . .	55
2.4.4	Coaxial Cavity Efficiency at Low Velocity . . . . .	58
2.4.5	An Aside: The Three-Quarter Wave Resonator . . . . .	59
2.4.6	Another Aside: Power Transmission Choices Based on Frequency . . . . .	60
2.5	Superconducting Material Properties . . . . .	61
2.5.1	Superconducting Material Theory . . . . .	61
2.5.2	The Advantages of Superconductivity . . . . .	64
2.5.3	The Challenges of Superconducting Materials . . . . .	65
2.5.4	Practical Concerns: RRR and Impurities . . . . .	66
2.6	Coupler Theory and Design . . . . .	66
2.6.1	Coupler Figures of Merit . . . . .	67
2.6.2	Bandwidth Considerations . . . . .	70
2.6.3	High Power Concerns . . . . .	71
2.7	Parameter Scaling and Resonator Selection Based on Application . . . . .	72
2.7.1	What Type of Charged Particle? . . . . .	72
2.7.2	What Energy? . . . . .	73
2.7.3	How Much Beam Power? . . . . .	73
2.7.4	The Transit Time Factor . . . . .	73
2.8	Operational Experience with Low-Beta Cavities . . . . .	74
2.8.1	Quarter Wave Resonators . . . . .	74
2.8.2	Half Wave Resonators . . . . .	75
<b>3</b>	<b>Electromagnetic and Mechanical Design of a Half Wave Resonator</b>	<b>76</b>
3.1	Electromagnetic Cavity Simulation . . . . .	76
3.1.1	Finite Element Solvers . . . . .	77
3.1.2	Geometry Creation . . . . .	79
3.1.3	Simulation Procedure . . . . .	79
3.1.4	An Aside - Computer Resource Management . . . . .	80
3.1.5	Simulation - Setup . . . . .	81
3.1.6	Simulation - Meshing . . . . .	82
3.1.7	Simulation - Solving . . . . .	87
3.1.8	Simulation - Post Processing . . . . .	88
3.2	Design of a Beta = 0.29, 322 MHz HWR . . . . .	92
3.2.1	The Ideal Half Wave Resonator - Revisited . . . . .	93
3.2.2	Beam Tubes and Drift Tubes . . . . .	93
3.2.3	Cavity Geometrical Features and Parameterization . . . . .	95
3.2.4	Cavity Performance Optimization Procedure . . . . .	100



3.2.5	Initial Geometry . . . . .	103
3.2.6	Large Scale Optimization . . . . .	104
3.2.7	Cavity Refinement and Final Results . . . . .	108
3.2.8	Coupling Power to the Cavity . . . . .	109
3.2.9	On the Subject of Rinse Ports . . . . .	115
3.2.10	Beam Port Cup Positioning Sensitivity . . . . .	116
3.2.11	Etching Coefficient Estimation . . . . .	117
3.3	Coupled Electromagnetic and Mechanical Simulations . . . . .	119
3.3.1	Generalized Procedure . . . . .	120
3.3.2	Geometry Modification for Simulation . . . . .	123
3.3.3	Accuracy Level . . . . .	125
3.3.4	An Aside: Slater's Theorem . . . . .	125
3.3.5	Pressure Sensitivity . . . . .	127
3.3.6	Lorentz Force Detuning . . . . .	129
3.3.7	Cavity Tuning . . . . .	131
3.3.8	Cavity Stiffening . . . . .	131
<b>4</b>	<b>Prototyping and Testing of Advanced Half Wave Resonators at Michigan State University</b>	<b>135</b>
4.1	Cavity Fabrication and Processing . . . . .	136
4.1.1	Material Selection through Subassembly Fabrication . . . . .	137
4.2	Cavity Testing Theory and Setup . . . . .	140
4.2.1	Testing Theory . . . . .	141
4.2.2	Measurement Procedure . . . . .	145
4.2.3	Calibration of the RF Network . . . . .	147
4.3	Challenges for Cavities in Testing and Operation . . . . .	150
4.3.1	Multipacting . . . . .	150
4.3.2	Avoiding Multipacting Before Testing/Operation . . . . .	151
4.3.3	Dealing with Multipacting During Testing/Operation . . . . .	152
4.3.4	Field Emission . . . . .	152
4.3.5	Q-Disease . . . . .	154
4.4	The Testing of a Prototype $\beta = 0.53$ HWR . . . . .	154
4.4.1	Cavity Description . . . . .	155
4.4.2	Test Goals . . . . .	157
4.4.3	Test Results and Implications . . . . .	157
<b>5</b>	<b>Conclusions</b>	<b>164</b>
5.1	Electromagnetic and Mechanical Simulations . . . . .	164
5.2	On Simulation Scripting and Optimization . . . . .	165
5.3	On the Practicality of Half Wave Resonators . . . . .	167
5.4	Future Designs and Applications of Half Wave Resonators . . . . .	168

<b>6 ANSYS-APDL Scripting and Discussion</b>	<b>170</b>
6.1 ANSYS-APDL Electromagnetic Script . . . . .	170
6.2 ANSYS-APDL Mechanical Script . . . . .	183
<b>Bibliography . . . . .</b>	<b>204</b>

## LIST OF TABLES

3.1	Initial cavity geometrical variables. . . . .	104
3.2	Initial Cavity Figures of Merit. . . . .	104
3.3	Outer Conductor Radius Parameter Scan Results. . . . .	105
3.4	Cavity Performance Change due to Hemispherical Short Plate Profile. . . . .	108
3.5	Inner Conductor Magnetic Field Region Radius Parameter Scan Results. . . . .	108
3.6	Inner Conductor Electric Field Region Width Parameter Scan Results. . . . .	109
3.7	Cavity Figures of Merit. . . . .	109
3.8	Cavity Figure of Merit Sensitivity to Beam Port Cup Position. Cup displacement ( $X$ ) is the distance each cup is symmetrically moved from nominal with the positive direction being towards the inner conductor. . . . .	117
3.9	Material Properties used for Simulation. . . . .	121
3.10	Electromechanical Properties for different beam port cup thicknesses. . . . .	132
3.11	Optimized Electromechanical Properties. . . . .	134
4.1	External Quality Factors used during Testing. . . . .	159

## LIST OF FIGURES

1.1	Top: Alpha particles passing through the less dense bread pudding model of the atom, Bottom: Alpha particles being deflected by Rutherford's model of a small, dense nucleus. For interpretation of the references to color in this and all other figures, the reader is referred to the electronic version of this dissertation. . . . .	4
1.2	Schematic of an RF accelerator with particle source (left), voltage source (bottom right), and repeating drift tubes/gaps for acceleration. Note the increased length of the drift tubes as the particles gain energy. . . . .	6
1.3	Schematic of Wideroe's Demonstration Accelerator . . . . .	7
1.4	Chart of the Nucleotides . . . . .	9
2.1	Resonant curves for damped, driven harmonic oscillator with $\gamma = 0.5, 0.2, 0.1, 0$	23
2.2	Oscillator phase shift compared to driving term versus detuning. Note the nearly linear region near resonance. . . . .	24
2.3	Van der Pol coordinate transformation into a frame rotating at $\omega$ . . . . .	25
2.4	Oscillator amplitude versus detuning. Circles represent $\alpha = -0.002$ , crosses represent $\alpha = 0$ . . . . .	28
2.5	Oscillator phase versus detuning. Circles represent $\alpha = -0.002$ , crosses represent $\alpha = 0$ . . . . .	29
2.6	An example of pillbox type cavities coupled together. . . . .	40
2.7	The Transit Time Factor (TTF) for 2, 4, and 8 cavities in series with $\beta_{opt} = 0.50$ .	41
2.8	Schematic of the ideal QWR. . . . .	50
2.9	An example of the accelerating electric field for an ideal coaxial resonator. The beam axis passes radially through the cavity at $z = 0$ . . . . .	51

2.10	$R/Q$ and $G$ versus gap size for an ideal 80.5 MHz, $\beta = 0.041$ QWR. . . . .	54
2.11	FRIB Quarter Wave Resonator designs. . . . .	55
2.12	Schematic of an ideal HWR. . . . .	56
2.13	Geometry Factor plotted versus $\beta$ for the ideal cavity geometries. . . . .	60
2.14	Magnetic field just inside superconducting material around transition for Type 1 and 2 materials. Note the sudden penetration for Type 1 and the gradual break down for Type 2. . . . .	64
3.1	A cavity vacuum space meshed with tetrahedral elements, a coupler probe is in the foreground with a beam port cup visible in the background. . . . .	77
3.2	Structure of a first order (linear) tetrahedral element. Image credit to F. Krawczyk. . . . .	78
3.3	HWR vacuum model. Symmetry planes can be seen in blue, Perfect Electric Boundaries can be seen in gray, the cavity origin is marked in red. . . . .	82
3.4	Comparison of different meshing on a curved surface. Left: Poor meshing on a curved surface. Right: Same surface with improved mesh density. Images generated using ANSYS. . . . .	83
3.5	Fractional frequency error for different mesh densities in identical geometries for first and second order elements. . . . .	85
3.6	The intersection of four surfaces can force excess mesh density, indicated by the red arrow. Images generated using ANSYS. . . . .	86
3.7	Top Left: Poorly meshed cavity, beam axis marked in red. Top Right: Resulting accelerating electric field. Note the non-physical roughness that results from the large element size. Bottom Left: Cavity with improved meshing on beam axis which is marked in red. Bottom Right: Resulting accelerating electric field. Note the improved field profile that results. Images generated in ANSYS. . . . .	87
3.8	Left: Magnitude of the surface electric field on a beam port cup with inadequate meshing for surface field accuracy. Right: Identical geometry with improved meshing and more realistic surface fields. . . . .	89

3.9	Plot of transit time factor versus particle beta. . . . .	91
3.10	Beam port and drift tube position in a HWR with a red arrow indicating the beam axis. One of the RF ports can be seen on the cavity midplane in the background. . . . .	94
3.11	HWR vacuum space cut on three symmetry planes. . . . .	95
3.12	Left: Sketch determining the bulk of the cavity vacuum space with dimensions in mm. Right: Resulting volume after the sketch is rotated about the symmetric axis of the cavity. Three symmetric planes assumed. . . . .	96
3.13	Left: Sketch determining the high electric field region with dimensions in mm. Right: Resulting volume after the sketch is cut from the bulk of the cavity. Three symmetric planes assumed. . . . .	97
3.14	Left: Setup for the loft cut to complete the inner conductor shape. Automatic spline guide curves for the cut can be seen in black with the tangential boundary condition shown by purple arrows. Center: Resulting inner conductor shape with smooth transition between magnetic and electric field regions. Three symmetric planes assumed. Right: Resulting inner conductor geometry. . . . .	99
3.15	After the addition of the drift tube, a fillet is introduced to reduce the field enhancement on the inner conductor. Three symmetric planes assumed. . . . .	100
3.16	Left: Sketch determining the beam port cup with dimensions in mm. Right: Resulting beam port geometry with the beam axis in red. Three symmetric planes assumed. . . . .	101
3.17	The work flow for optimization of a geometric variable. . . . .	102
3.18	Contour plot of surface magnetic field magnitude. The peak magnetic field can be seen where the inner conductor meets the short plate. A change in geometry may improve the peak field value. . . . .	106
3.19	New cavity geometry with a hemisphere for the short plate profile. . . . .	107
3.20	Contour plot of surface magnetic field magnitude. Left: Magnitude of the Electric Field after Tier 1 optimization. Right: Magnitude of the Magnetic Field after Tier 1 optimization. Note the high electric fields on the beam port cup. . . . .	110

3.21	Left: Final beam port cup geometry. Right: Magnitude of the Electric Field after optimization. . . . .	111
3.22	The coupler probe can be seen in the foreground connected to the RF port by the surface indicated by the red arrow. This is a quarter of the geometry cut on the symmetry planes. . . . .	112
3.23	Plot of the magnitude of the magnetic field on the PEC termination of a coupler port. Simulated with planes of symmetry in x and y. . . . .	113
3.24	Plot of measured and simulated Q-externals for a 0.53 HWR prototype. The simulated data is represented by the large black squares. The rest are repeated rounds of measured data. . . . .	114
3.25	Left: Rinse port on a HWR short plate with fillet. Right: Plot of surface magnetic field on the rinse port versus radius of the fillet. The red line indicates the peak surface magnetic field in the rest of the cavity. . . . .	115
3.26	Plot of simulated etching coefficient for a prototype $\beta = 0.53$ HWR filled with acid to different levels. The blue diamonds represent simulation data, and the red squares are this data mirrored assuming symmetry. . . . .	119
3.27	Material space after importation into ANSYS-APDL. . . . .	122
3.28	Left: Flange before simplification for simulation. Bolt holes are indicated by red arrows, fillets and chamfers by green arrows, and a complex feature (vacuum seal knife edge) is indicated by a blue arrow. Right: Simplified flange ready for inclusion in a simulation. . . . .	125
3.29	Frequency shift versus applied pressure for a mechanical simulation. Note the linearity down to very small frequency shifts. . . . .	126
3.30	Left: Deformation of the inner conductor due to pressure differential. Right: Deformation of the outer conductor due to a pressure differential (5000 Pa). . . . .	128
3.31	Deformation of the cavity with the Lorentz Force applied at full accelerating voltage. . . . .	130
3.32	Simulation of cavity deformation for an applied tuning force. . . . .	132
3.33	Left: Stiffening ring added to the inner conductor in section view. Right: Top down view of the stiffening ring with full cavity. . . . .	133

4.1	Prototype $\beta = 0.53$ HWR manufactured and tested at MSU with helium vessel.	136
4.2	Left: Half of an inner conductor after forming with coined drift tube fillet. Middle: Two inner conductor halves ready to be welded to a drift tube. Right: Fully fabricated inner conductor. . . . .	138
4.3	Left: Completed short plate subassemblies, with and without rinse ports. Middle: Rinse port milled from a niobium billet, ready to be welded to the short plate. Right: Fully fabricated outer conductor. . . . .	139
4.4	Left: The inner conductor is welded to a short plate. Middle: The outer conductor with RF ports is welded to the opposite short plate. Right: The final two large subassemblies ready to be welded together. . . . .	140
4.5	The beam port cups are positioned to achieve the final frequency. The cup on the right is in the ideal (design) position. . . . .	141
4.6	Transient behavior of the reverse power for different coupling strengths. All curves are in response to the shown forward power behavior. Image credit to Tom Powers, TJNAF. . . . .	143
4.7	Basic RF circuit for a phase lock loop for cavity testing with the calibration points marked. . . . .	148
4.8	Prototype $\beta = 0.53$ HWR manufactured and tested at MSU. . . . .	155
4.9	Left: Mechanical design of the prototype $\beta = 0.53$ HWR, manufactured and tested at MSU. Right: More recent mechanical design of a $\beta = 0.53$ HWR that shares many design features with the HWR designed in this document. . . . .	156
4.10	Mechanical Drawing of the NSCL large test Dewar, where this cavity test was performed. . . . .	158
4.11	Both days of testing data plotted on the Duality Triangle to verify self consistency. . . . .	160
4.12	Cavity Quality Factor ( $Q_0$ ) plotted versus Peak Surface Electric Field for both testing days. . . . .	161
4.13	One half of the RF circuit for a phase lock loop for cavity testing (circulator, isolators, and RF diodes excluded). Letters in Red connect to the other half of the RF circuit, seen on the next page. . . . .	162



4.14 One half of the RF circuit for a phase lock loop for cavity testing (circulator, isolators, and RF diodes excluded). Letters in Red connect to the other half of the RF circuit, seen on the previous page. . . . . 163

## KEY TO SYMBOLS AND ABBREVIATIONS

ANL - Argonne National Laboratory (Argonne IL, USA)

ATLAS - Argonne Tandem Linear Accelerator System (ANL)

BCP - Buffered Chemical Processing

BPM - Beam Position Monitor

CAD - Computer Aided Design

CERN - European Center for Nuclear Research (Geneva, Switzerland)

CW - Continuous Wave

DC - Direct Current

DoE - Department of Energy

FRIB - The Facility for Rare Isotope Beams (East Lansing MI, USA)

HWR - Half Wave Resonator

IC - Inner Conductor

ILC - International Linear Collider

ISAC II - Isotope Separator and Accelerator II (TRIUMF)

LEBT - Low Energy Beam Transport

Linac - Linear Accelerator

LFD - Lorentz Force Detuning

LHC - Large Hadron Collider (CERN)

MSU - Michigan State University (East Lansing MI, USA)

NSCL - National Superconducting Cyclotron Laboratory (MSU)

NSF - National Science Foundation

OC - Outer Conductor

OFHC - Oxygen Free High Conductivity

PEC - Perfect Electric Conductor

PMC - Perfect Magnetic Conductor

QWR - Quarter Wave Resonator

ReA3 - Re-Accelerator, 3 MeV

RF - Radio Frequency

RRR - Residual Resistance Ratio

SARAF - Soreq Applied Research Accelerator Facility (Soreq NRC, Israel)

SEY - Secondary Emission Yield

SRF - Superconducting Radio Frequency

TE - Transverse Electric

TEM - Transverse Electric and Magnetic

TJNAF - Thomas Jefferson National Accelerator Facility (Newport News VA, USA)

TM - Transverse Magnetic

TTF - Transit Time Factor

TRIUMF - Tri-University Meson Facility (Vancouver)

VNA - Vector Network Analyzer

$\beta$  - Particle velocity divided by the speed of light

$\beta_n$  - Coupling factor of port  $n$

$\beta_{opt}$  - Cavity optimum particle velocity divided by the speed of light

$\omega$  - Angular Frequency

$a$  - Inner conductor diameter m

$b$  - Outer conductor diameter m

$B_{pk}$  - Peak surface Magnetic field mT  
 $BW$  - Bandwidth Hz  
 $c$  - Speed of light ( $2.998 \times 10^8$  m/s)  
 $\delta$  - RF skin depth m  
 $e$  - Charge of the electron  
 $\eta$  - Impedance of free space ( $\sim 377 \Omega$ )  
 $E_{acc}$  - Accelerating Electric field MV/m  
 $E_{pk}$  - Peak surface Electric field MV/m  
 $f_0$  - Cavity resonant frequency MHz  
 $G$  - Geometry Factor  
 $\gamma$  - Relativistic Lorentz Factor  
 $H_{pk}$  - Peak surface Magnetizing field A/m  
 $\lambda$  - Cavity wavelength m  
 $\lambda_L$  - London Length m  
 $P_d$  - Cavity dissipated power W  
 $P_e$  - Emitted power W  
 $P_t$  - Transmitted power W  
 $Q_0$  - Cavity Quality Factor  
 $Q_{ext,n}$  - External Quality Factor for port  $n$   
 $Q_L$  - Cavity Loaded Quality Factor  
 $R_{BCS}$  - BCS surface resistance  $\Omega$   
 $R_s$  - RF surface resistance  $\Omega$   
 $R/Q$  - Effective Shunt Impedance divided by the Quality Factor

$U$  - Cavity stored energy J

$V_{acc}$  - Accelerating Voltage MV

# Chapter 1

## Particle Accelerators and Nuclear Physics

Science is the process of understanding the world around us through systematic investigation and testing. While passive observation has provided many insights into the inner workings of nature, modern scientists regularly use a wide variety of instrumentation and other experimental tools to perform their work. These tools have had to grow in complexity with science's understanding, with the theory and development of some of these tools becoming fields of study in their own right. An example of this is the science of particle accelerators. These devices were developed in the 1920s to aid in the study of the atomic nucleus and its properties. Since then, the study of particle accelerators has become a branch of physics itself, and like the field of nuclear physics itself, has grown far more complex and subtle since its conception. In this chapter, the evolution of particle accelerators and their usage for nuclear physics will be described with a look to the future of both fields.

## 1.1 The Origins of Nuclear Physics

Atoms are the basic building blocks from which all matter is constructed. Although atoms, as a concept, were first theorized almost 2500 years ago, their discovery and study would not begin until the 1700s. The first hints of this structure began with the study of chemistry when it was discovered that there was a limit to how much any chemical could be broken down through chemical reaction. What had been discovered was the existence of the elements that we know today like oxygen, carbon, titanium. While this led to the modern atomic theory, it would not be experimentally verified until the study and description of Brownian Motion at the turn of the 20th century. Brownian Motion is the name given to the random motion of small particles suspended in a fluid (say, small dust particles in a still glass of water). It was theorized that this motion was caused by the random thermal oscillations of the atoms in the water. In 1905, Albert Einstein described the mathematics of this process, and this work was used to experimentally predict the size and mass of atoms. What was not known, however, was the internal structure of atoms. Around this time, the discovery of radioactivity had given scientists a power tool of investigation. The products of radioactive decay were small enough and high enough in energy that they could penetrate into materials, giving scientists the first glimpse of their internal structure. One of these types of radiation was called alpha radiation. Ernest Rutherford passed this radiation through a thin foil of gold and discovered that a surprising number of the alpha particles were deflected at great angles from their original trajectory, almost backwards. The most common model for the structure of the atom up to this point was the “bread pudding” model, the positive charge spread evenly through the whole volume of the atom with the negatively charged electrons scattered around (like the raisins in bread pudding). If this was the case, then it would be expected that the

alpha particles would have passed through the gold atoms without encountering anything dense enough to deflect them that significantly. This model and behavior can be seen in Figure 1.1 (top). The discovery that some of the alphas were significantly deflected meant that there must be some part of the atomic structure that was very dense, dense enough to significantly deflect them, as can be seen in Figure 1.1 (bottom). According to Rutherford, this discovery was “quite the most incredible event that has ever happened to me in my life. It was almost as incredible as if you fired a 15-inch shell at a piece of tissue paper and it came back and hit you” [1]. From this experiment, Rutherford theorized that all of the positive charge in the atom was bound to this small, dense body at the center of the atom, which he called the nucleus. His model of a dense, positively charged nucleus surrounded by orbiting electrons was the beginning of modern nuclear physics.

## 1.2 Atoms as a Probe

The crucial fact that allowed Rutherford’s experiment was the use of an experimental tool that was small enough to be sensitive to the structure he wanted to observe. Alpha particles had been demonstrated earlier to be ionized helium atoms, and with this experiment, they were shown to be nuclei as well. This was the beginning of the usage of atomic and subatomic particles (protons, neutrons, electrons, etc.) as experimental tools themselves. While alpha (helium nuclei), beta (electrons), and gamma (photons) radiation could be generated from radioactive material, it was soon clear that there was much to be gained if the intensity and power of the beams of particles could be increased. More intense beams would, like a brighter flashlight, allow more detailed and rapid study of the nucleus. Higher energies would be needed because of Coulomb repulsion. In the gold foil experiments, the alpha



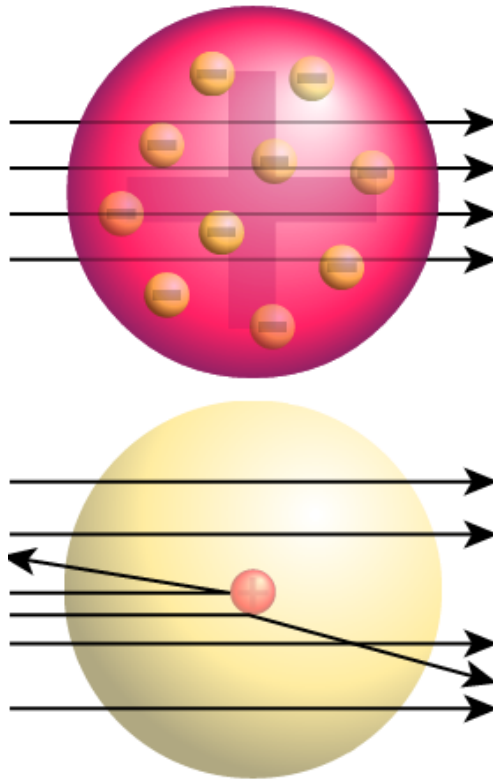


Figure 1.1: Top: Alpha particles passing through the less dense bread pudding model of the atom, Bottom: Alpha particles being deflected by Rutherford's model of a small, dense nucleus. For interpretation of the references to color in this and all other figures, the reader is referred to the electronic version of this dissertation.

radiation never actually collided with the atomic nucleus. Because both of these objects are positively charged, they repel each other very strongly, so the alphas were just deflected. Higher energies could overcome this repulsion, allowing detailed probing of the structure of the newly discovered nucleus, and Rutherford knew it.

### 1.3 Rutherford's Address to the Royal Society

In 1927, Rutherford was the president of the English Royal Society, the most prestigious scientific organization in the world. As was tradition, he gave an annual address to the Society, and in his 1927 address, he called for a new study and development of particle

accelerators. He expressed a long-standing “ambition to have available for study a copious supply of atoms and electrons which have an individual energy far transcending that of the alpha and beta particles” available from natural sources so as to “open up an extraordinarily interesting field of investigation” [1]. The explosion of invention and discovery spurred in part by this speech has revolutionized nuclear physics, astrophysics, and other branches of physics, even creating several new fields of study. His true foresight is evident in his call for “A million volts in a soapbox,” a level of acceleration that is close to the level that can be achieved in today’s modern accelerators.

## 1.4 Electrostatic Accelerators

All particle accelerators use electric fields to accelerate charged particles. In the early particle accelerators, this electric field was established by creating a large, fixed potential difference across a gap, causing the particle to gain energy as it crossed that gap. This method is still used today in almost all particle sources to give the beam its initial energy. The energy that these structures can impart per charge is limited, however, to around 60 MV by break down (an electron, having charge  $e$ , passing through this gap would thus gain 60 MeV of energy). An analogy of this limit can be found in a skateboard park. If a skateboarder wishes to go faster without pushing themselves, they must find a ramp. To gain more energy, the ramp must get taller and taller. Very rapidly, the height achievable becomes limited by the materials available, limiting the energy the skater can have. A similar situation limits electrostatic accelerators; increasing the potential difference across the gap becomes more and more challenging, requiring increasingly specialized and expensive techniques and materials (like placing the whole structure in sulfur hexafluoride to prevent sparking). It is also not

possible to use the same gap more than once (twice, if you play some very special games with the particle charge), and the skate park analogy continues to be useful here as well. Once the skater has reached the bottom of the ramp, there is no way for them to take advantage of the ramp's drop again; all of their energy gained would be lost again getting back to the top.

## 1.5 The Radio-Frequency Revolution

If you wish to achieve a higher energy, you need to use a voltage that oscillates in time. The particle crosses a gap while the electric fields in that gap are in the correct direction for acceleration, and then travels through a region that is shielded from the fields when they are in the opposite orientation. A cartoon of this setup can be seen in Figure 1.2. This can

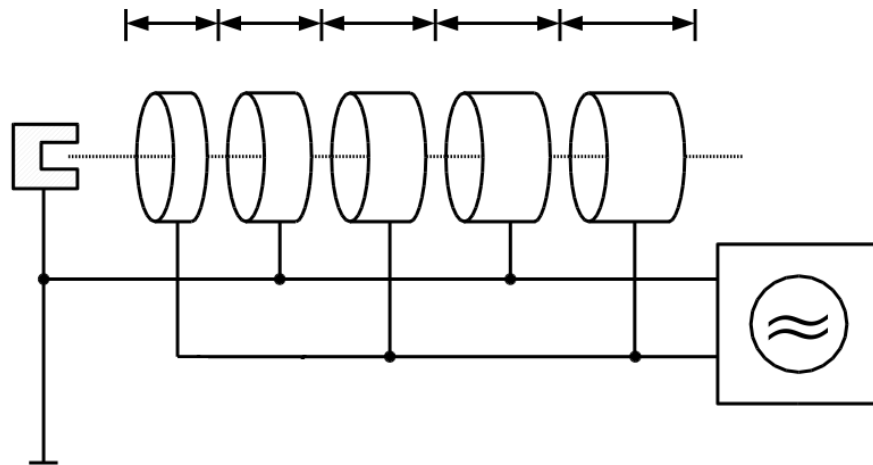


Figure 1.2: Schematic of an RF accelerator with particle source (left), voltage source (bottom right), and repeating drift tubes/gaps for acceleration. Note the increased length of the drift tubes as the particles gain energy.

either be repeated with many synchronized gaps in series, or the same gap can be used many

times by bending the particle back to its starting position. This overcomes the limitations of electrostatic accelerators. While the total energy gain per gap is still limited, the total energy gain is technically unlimited because there is no limit to the amount of gaps you can have. For example, the proposed International Linear Collider (ILC) will consist of 16000 (8000 each for two different particle types) acceleration segments with 9 gaps each, each segment providing about 31.5 MeV of energy. While the energy gain per gap is only  $\sim 3.5$  MeV, each beam will gain a total of  $\sim 250,000$  MeV, or 250 GeV. Rolf Wideroe was the first to successfully demonstrate this acceleration technique, and the concept of RF (radio frequency) particle acceleration has come to dominate particle accelerators. A schematic of Wideroe's demonstration accelerator can be seen in Figure 1.3.

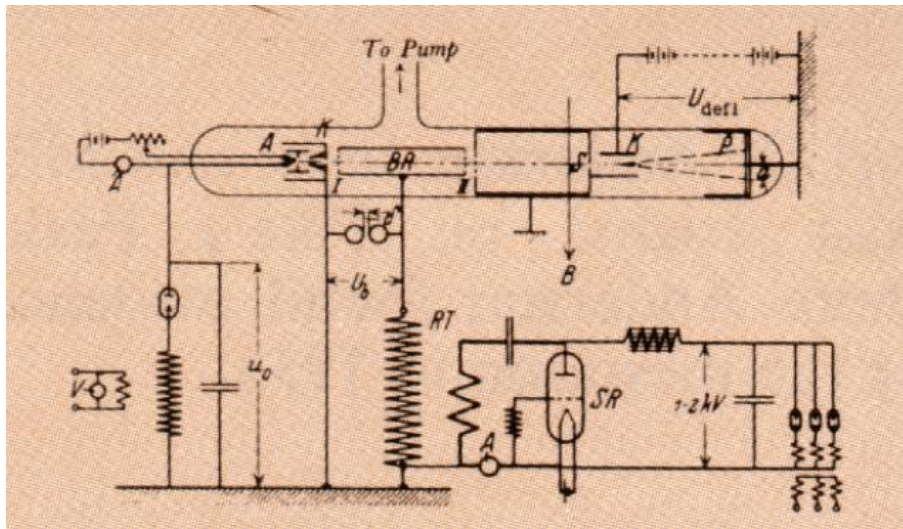


Figure 1.3: Schematic of Wideroe's Demonstration Accelerator

With this device, he achieved 50 kV of acceleration with only 25 kV and two gaps. There are downsides to this type of acceleration, especially the need for careful shaping of the beam into small bunches and the careful timing of the accelerating field. The gains, though, are significant. Most of the research in accelerator physics has been devoted to the advancement of this type of accelerator, and most modern nuclear physics is performed using this kind of

accelerator.

## 1.6 The Chart of the Nucleotides

Experimentation continued with the nucleus, and it was discovered that it consisted of two types of subatomic particles, tightly bound together by the strong (nuclear) force. The first type is the proton, with the opposite charge of the electron but almost 2000 times heavier. The other type of particle is the neutron. This particle carries no charge, and is slightly more massive than the proton. The number of protons in the nucleus determines the nuclear charge, and because of the dominant strength of the electromagnetic force, it determines what chemical properties the atom has. These properties determine the type of element the atom is, such as oxygen, Carbon, or Uranium. One problem is that protons repel each other strongly, especially when packed into a small volume such as the nucleus. The neutrons add mass to the nucleus while increasing the nuclear volume, reducing the repulsion. This allows more protons to be contained in a stable nucleus, allowing the heavier elements up to and beyond Uranium to exist. While the number of protons determines the element of the atom, an element can often exist with different numbers of neutrons. These chemically identical atoms that have different numbers of neutrons are called isotopes, and their properties are a prime focus for nuclear physicists. Figure 1.4 is known as the Chart of the Nucleotides, and is the most common way of displaying the known isotopes and their basic properties.

Often, there are one or two isotopes of an element that can exist for long periods of time (thousands of years or more) without breaking apart, and these are called stable isotopes. These are the isotopes often found in nature, and have been heavily studied in the last century because of their availability. However, there are also isotopes that exist with more

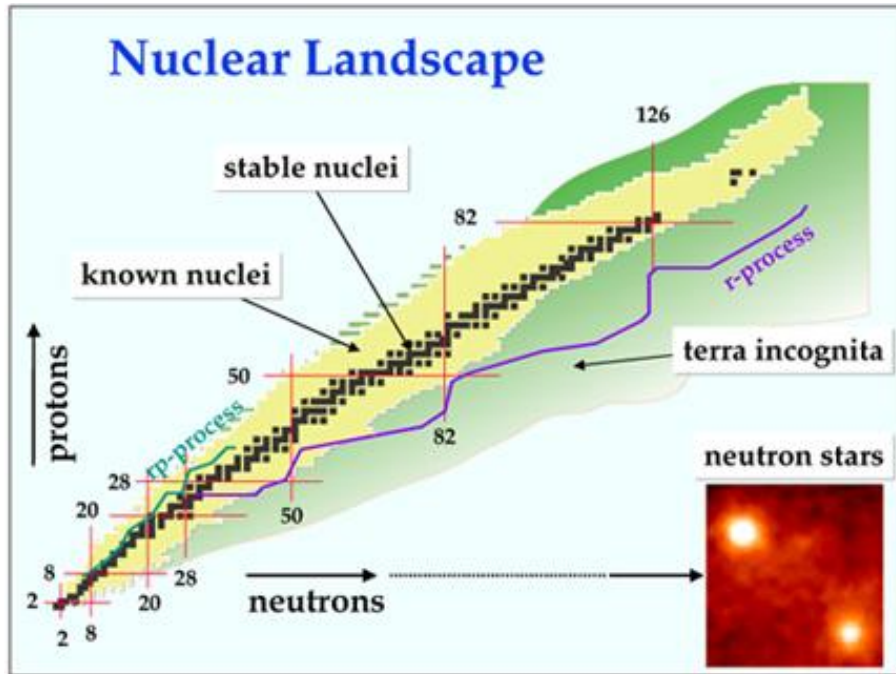


Figure 1.4: Chart of the Nucleotides

or less neutrons than the stable isotopes. Whether you add neutrons or subtract them, the nucleus grows less stable. Either there are too many neutrons, making it easy for them to escape, or there are too few, and the proton repulsion is barely contained. Either way, these elements eventually break apart, producing nuclei with different numbers of protons and neutrons until a more stable state is reached. These elements are called radioactive isotopes and one of them was the source of the alpha radiation that Rutherford used in his experiment. The rate at which these unstable isotopes decay is characterized by the half life, or time it takes half of a set number of them to decay. A example of this behavior is known as Carbon-14 dating. Carbon-12 and Carbon-13 are the most common isotopes of Carbon, and they are stable. Carbon-14 is a slightly unstable isotope that is created in the upper atmosphere by cosmic rays. Some of this forms Carbon Dioxide, which plants absorb during photosynthesis. As animals eat plants, they ingest Carbon-14, up to a certain concentration.

When the animal stops eating plants (or things that ate plants), the amount of Carbon-14 starts to fall while the amount of Carbon-12 and Carbon-13 stays constant. With a half life of  $\sim 5730$  years, Carbon-14 can be used to estimate the age of the remains of creatures that lived up to 45,000 years ago with a good degree of accuracy.

## 1.7 Rare Isotope Production

The further you get from stability, the shorter the half life, making it more challenging to study these isotopes in a laboratory. These are, however, the most interesting isotopes for nuclear physicists because their properties provide data crucial for the modeling of all nuclei. Starting from the isotopes found in nature, it is possible to create these short-lived (rare) isotopes for study. A variety of methods exist for this, but all involve accelerating and colliding one atom with another. This breaks apart the heavier atoms, giving the machines used for this the name “atom smashers”. Breaking apart a heavy nucleus produces a wide variety of smaller isotopes, including the desired short-lived rare isotope. These products are then collected and purified until only the desired isotope remains for study. To increase the effectiveness of these machines, it is desired to increase the energy of the collision as well as the intensity of the accelerated atoms. This increases the production rates of the desired rare isotopes, allowing scientists to collect more data for each isotope. It is predicted that there are  $\sim 8000$  isotopes that can be produced, only  $\sim 3000$  of which have been observed, with only  $\sim 1800$  of these having been studied in great detail.

## 1.8 Seeking the Answers to Fundamental Questions

The study of these isotopes provides valuable insight to the fundamental forces that govern our universe. This knowledge helps us to answer questions like “where did the heavy elements on Earth come from?” Early in the history of the universe, almost all of the matter in existence was one of the two lightest elements, hydrogen or helium. Over billions of years, these gasses formed into stars powered by nuclear fusion, producing heavier and heavier elements. It is impossible to form anything heavier than lead through this process, however. Where did all of the elements found on Earth that are heavier than lead come from, then? It is theorized that it took a supernova to form them. In the extreme environment of a stellar explosion, the conditions existed to form heavier elements and then cast them out into the universe. These explosions seeded the universe with every element on the periodic table, and when the second generation of stars and solar systems formed, there was enough heavy material to form planets like Earth. Understanding the properties of all of the unstable isotopes is required to model what happens during a supernova, and how they are formed in one, decaying into the more stable isotopes found on Earth today. An ultimate goal of this research is to be able to model the formation of these isotopes in a supernova and have the results agree with the amounts of these heavy elements found on the Earth today. In addition to this, there are more theoretical questions that can be answered by this type of research. The structure of the nucleus is very complex, and not well understood or modeled. Studying the structure of rare isotopes allows testing of the more complex nuclear structure theories and can indicate the form of a new one. The goal is to be able to have one theory that accurately agrees with the measured data for all known isotopes and can predict the properties of new isotopes.



## **1.9 The Benefits of Understanding**

In addition to more theoretical pursuits, a practical understanding of nuclear physics and the technology developed for its study have real world benefits. Examples of this can be seen in the medical profession where radioisotopes (radioactive isotopes) are used for many purposes, from cardiac imaging to cancer treatment. The same technology developed for accelerators is used in hospitals, generating these radioisotopes or accelerating beams for use in treating cancer directly. Additionally, this technology has direct applications for nuclear stockpile stewardship and homeland security. Advanced nuclear reactor designs show great promise for more safe, reliable nuclear power in the future, but require detailed studies of material properties that cannot be studied at any other type of facility. In addition to a more safe, clean nuclear reactor, a better understanding of nuclear and accelerator physics will aid in the goal of allowing the transmutation of nuclear waste, eliminating the need for challenging long term storage. An example of the implications for homeland security is port security. Nuclear physics research is instrumental in the development of scanning technology that could allow rapid and accurate detection of nuclear weapons and other dangerous materials trying to enter the country. These are just some of the examples of the benefits reaped from the study of both nuclear and accelerator physics.

## **1.10 Purpose of Research**

Advanced heavy isotope accelerators for nuclear physics research require advances in accelerator technology. The research presented in this document is part of this evolution, the development and optimization of an advanced accelerator resonator. The project that mo-

tivates this work, the Facility for Rare Isotope Beams (FRIB) will be discussed, and the motivation for its usage of this type of resonator, Half Wave Resonator, will be presented. The theory of these resonators and the tools used to design them will be detailed, and a complete electromagnetic and mechanical design optimization will be presented. The construction and testing of a Half Wave Resonator will also be presented with a discussion of future advancement and usage of Half Wave Resonators.

# Chapter 2

## The Physics of Particle Accelerators

Essentially all modern nuclear physics facilities require a particle accelerator of some kind. This chapter will discuss the theory and design of an advanced nuclear physics accelerator with a focus on the special radio frequency resonators used. The theory of these resonators will be presented in the context of the design of the Facility for Rare Isotope Beams (FRIB), a Department of Energy (DoE) supported project expected to start delivering world-leading beams for nuclear physics in the next decade. The relevant secondary technologies required for this accelerator will also be discussed such as cryogenics, superconducting materials, and radio frequency systems.

### 2.1 The Basic Structure of a Particle Accelerator

A particle accelerator is, at its core, a structure designed to produce a beam of charged particles with kinetic energy that is well above the thermal energy range. In order to study the properties of radioisotopes, nuclear physicists need to produce specific isotopes in large quantities. Natural radioactive sources can deliver some types of radioisotopes at a range of

fixed energies, depending on the decay process involved. However, the rate of radioisotope production is limited by the quantity and concentration of radioactive material that is practical to use: the supply of many elements naturally occurring isotopes is limited because of their low abundance. Moreover, radioactive sources are naturally limited by their half life; over time the source intensity decreases as the material decays into more stable isotopes. Sources which produce radioisotopes at higher rates necessarily decay more rapidly. Some radioisotopes cannot be produced by natural radioactive sources at all. A particle accelerator, on the other hand, can be designed to produce a beam of almost any material. The energy at which the isotope is delivered can be controlled, and the isotope can be delivered at a rate that is much higher than can be achieved from natural sources. This section will overview most of the major components necessary for a modern particle accelerator with some practical examples.

### **2.1.1 Charged Particle Source**

The front end of a particle accelerator is the particle source. These systems are responsible for generating the beam of the desired charged particles to be accelerated. This is typically generated as a continuous stream of low-energy particles, and must be very carefully confined as it is transported. Low Energy Beam Transport (LEBT) is a complex discipline in itself, the final quality of the beam depends on the quality at the source. This beam is then accelerated, typically by an electrostatic gap, and bunched. An RF accelerator requires the continuous beam to be confined to small bunches because of the oscillatory nature of the accelerating fields required for proper acceleration. Because the particles desired can vary quite a bit from machine to machine, there are many configurations for these systems. For

FRIB, the particle source will be required to produce beams of many different elements. These will be generated by heating a small, extremely pure sample of the isotope to be accelerated, hot enough to vaporize a small amount of the isotope. This is then confined in powerful magnetic fields while some of its electrons are stripped away by microwaves. This now-charged beam is then bunched and injected into the accelerator.

## 2.1.2 Acceleration Mechanism

After the bunched beam is produced, it must be accelerated up to the desired energy. This section is generally distinct from the source, and the beam must be injected into the accelerating section. From here, the beam will pass through many accelerating gaps, gaining energy along the way. This is either achieved by having a small number of accelerating gaps that the beam passes through many times, or having many accelerating gaps in series. These gaps consist of accelerating cavities, each with a resonant frequency that is an integer multiple of the frequency of the bunched beam. These resonators are designed to store energy and transfer that energy to the beam as efficiently as possible. For machines where the same accelerating section is used over and over again (for the Large Hadron Collider (LHC) at CERN, the same bunch sees the same resonator over 11,000 times a second [2]), the focus of the resonators is not as much to accelerate the beam as quickly as possible, but rather to make sure the quality of the bunch is maintained. Because of the number of times the same bunch sees the resonator, any disturbance tends to grow, and can have drastic consequences for the machine. In a linear machine where each bunch sees each resonator exactly once, the focus is more on efficiency of accelerating, making sure to give the beam as much energy as possible. The remainder of this document will focus on the second use of resonators.

### 2.1.3 Particle Transportation and Confinement

While every accelerator is designed to accelerate a specific particle, called the “reference particle”, real machines must accelerate bunches of particles with a distribution of energies and trajectories around the reference particle. Given time, these particles will drift away from the ideal trajectory and be lost unless confined. Just as electromagnetic fields are used to accelerate the beam, they can be used to confine the beam. The design of these systems, most often constructed of solenoid, dipole, and/or quadrupole magnets, is a complex discipline in its own right. Dipole magnets are used to bend the beam, and for a circular machine, they make up the bulk of the required magnets. Even for linear machines, there is often the requirement of bending the beam several times, say, from the particle source to the beginning of the accelerating section. Additionally, solenoid and quadrupole magnets are used to confine and focus the beam during transport and acceleration. Because no beam can be constructed with all of the particles traveling in the same direction, the beam will spread over time. These focusing magnets can be mathematically treated in much the same way lenses for light can, so the study of these magnets is often called “beam optics”. For an excellent introduction to these systems and their calculation, see “An Introduction to the Physics of High Energy Accelerators” by D.A. Edwards and M.J. Syphers [3].

### 2.1.4 Subsystems

A multitude of subsystems is required for accelerator operation. While I will not attempt to make an exhaustive listing, there are broad categories of subsystems shared by all accelerators that are worth mentioning. The first are power subsystems, providing wall power from the electrical grid to almost every active accelerator component, and this is in addition to

the traditional civil construction demands for power for things like air-conditioning, lights, computers, etc. Of special interest are the high power RF systems, generally consisting of klystrons and other amplifiers that produce the large amounts of power required to keep the accelerating cavities energized. Additionally, any electromagnet (the vast majority of magnets) will require a power supply.

The second set of subsystems is related to cooling. With so much power flowing through so many components, the heat generated becomes non-trivial, requiring subsystems to remove it. If the magnets/cavities are normal conducting (copper, for instance), then the heat is generated at room temperature and will often require water cooling with attached refrigerators. Very often, this water must also be high-purity, low-conductivity water instead of normal city water, requiring complex pumps and filters to maintain. If the magnets/cavities are made from superconducting material, then a cryogenics system is required instead of a conventional refrigerator. While the use of superconductors means that the losses are drastically reduced, these losses are generated at 2 K. The efficiency of a refrigerator at these temperatures is usually quite low – for every one 1 watt of losses at 2 K, it requires several hundred watts of wall power. For instance, the FRIB power plant design calls for a capacity of 15 kW at 4.5 K, but will require 5,250 kW of mechanical power to operate the compressors alone. Cryogenic systems require their own special design and infrastructure, from the generation of cryogenic liquid (most often liquid helium), transporting it, storing it around the components to keep them cold, and then recapturing the boiled off gas for reliquification.

Next, there are vacuum systems to consider. Special containment is required around all

components in the cryogenics system to insulate the liquid helium from the outside heat; even a small unnecessary heat load can overload the cryogenic plant's capability. The entire beam line must also be kept at a high vacuum ( $1 \times 10^{-8}$  torr) by vacuum pumps. The positioning and pumping strengths must be judged carefully to be sure that the proper vacuum is maintained throughout the machine, and often the cryogenics vessels use vacuum as an insulator, requiring even more vacuum pumping, all with instrumentation to measure and track the pressure in all of these locations.

Lastly, there is a large amount of data that is required so that the machine can be controlled safely and efficiently. To this end, there are a vast array of tools and monitoring devices used to allow operators to control the system. Beam Position Monitors (BPMs) are an excellent example of this; they give the operators and control systems data on where the beam is located in the machine. This and other data are then fed back into the machine to optimize performance. For this to be possible, all of these monitoring instruments must be wired to a central data system, requiring vast amounts of cabling and organization.

## 2.2 Resonator Theory

This section will provide insights for use in further sections by producing a generic formalism to describe resonators with the explicit goal of treating resonating cavities with the same mathematical treatment. Starting from the simple harmonic oscillator, damping and driving terms will be added, and their effects derived. The treatment of electromagnetic resonators by this formalism will then be justified, and a special case of interest will be presented.



### 2.2.1 The Ideal Harmonic Oscillator

The ideal, linear oscillator is the most basic starting point for solving many problems in physics. This is especially true in accelerator physics because so many of the phenomena of accelerator physics can be treated as purely classical and having few confounding effects.

The harmonic oscillator, without damping, has the form

$$\frac{d^2x}{dt^2} + \omega_0^2 x = 0 \quad (2.1)$$

where  $x(t)$  is the oscillating position at time  $t$ , and  $\omega_0$  is the oscillation frequency. The general solution for this is characterized by an amplitude  $A$  and a phase  $\phi$

$$x(t) = A \cos(\omega_0 t + \phi). \quad (2.2)$$

### 2.2.2 The Driven, Damped Harmonic Oscillator

For this to be a useful model we must consider damping. The form of damping that is of interest to us (because it is the form of the losses in a resonator), is damping proportional to the change in “position”, which has a form of

$$\frac{d^2x}{dt^2} + \gamma \frac{dx}{dt} + \omega_0^2 x = 0, \quad (2.3)$$

where the damping coefficient  $\gamma$  has the dimension of frequency. This type of equation has different forms of solution depending on the strength of the damping. If we choose the

damping to be weak, the general solution to this equation has the form

$$x(t) = Ae^{-\gamma_1 t} \cos(\omega_1 t + \phi) \quad (2.4)$$

where

$$\omega_1 = \omega_0 \sqrt{1 - \frac{\gamma^2}{4\omega_0^2}} \quad (2.5)$$

and

$$\gamma_1 = \frac{1}{2}\gamma. \quad (2.6)$$

Note that adding damping shifts the resonator frequency based on how strong the damping is. From this we can define a “quality factor”  $Q$  which is related to the rate at which the resonator loses energy.  $Q$  is defined by the equation  $Q = \omega_0/2\gamma$  with weak damping characterized by  $Q \gg 1$ . For a typical superconducting cavity,  $Q$  is generally  $\sim 5 \times 10^9$ , justifying the assumption of weak damping.

The effects of a driving term must also be considered. For an arbitrary driving term of the form  $f(t)$ , the differential equation becomes

$$\frac{d^2x}{dt^2} + \gamma \frac{dx}{dt} + \omega_0^2 x = f(t), \quad (2.7)$$

with the solution (for  $\gamma = 0$ )

$$x(t) = x_0 \cos \omega_0 t + \frac{\dot{x}_0}{\omega_0} \sin \omega_0 t + \frac{1}{\omega_0} \int_0^t \sin(\omega_0(t-t')) f(t') dt' \quad (2.8)$$

where  $x_0$  and  $\dot{x}_0$  are the initial position and velocity. The third term of this solution gives the

contribution from the driving term, and it is worthwhile to notice that a harmonic driving term with frequency equal to the resonant frequency of the oscillator will produce the largest oscillations, as expected.

### 2.2.3 Oscillator Behavior Near Resonance

It is most useful to examine the response of the weakly damped oscillator to driving near its resonant frequency because this is the desired case for resonator operation. Assuming a driving term that is purely harmonic ( $f(t) = f_0 \cos \omega t$ ) and ignoring transient behavior yields a solution with a relatively simple form. These assumptions are very justified in almost every accelerator application; most changes made to the driving term of the cavity have a time scale much larger than the RF period (which is usually on the order of nanoseconds). This type of differential equation is solved quite simply by assuming a complex solution and writing

$$\frac{d^2 \Xi}{dt^2} + \gamma \frac{d\Xi}{dt} + \omega_0^2 \Xi = f_0 e^{-i\omega t} \quad (2.9)$$

with  $x(t) = \Re \Xi(t)$ . We are seeking a solution of the form  $\Xi(t) = \Xi_0 e^{-i\omega t}$  where  $\Xi_0$  is also a complex number of the form  $\Xi_0 = |\Xi_0| e^{i\phi}$ . Solving for the real variable of interest  $x$  gives  $x(t) = \Re \Xi(t) = \Re(|\Xi_0| e^{-i\omega t + i\phi}) = |\Xi_0| \cos(\omega t - \phi)$ . Plugging this form of the solution into the differential equation gives

$$\left(-\omega^2 - i\omega\gamma + \omega_0^2\right) \Xi_0 = f_0 \quad (2.10)$$

simplifying to

$$\Xi_0 = \frac{f_0}{\omega_0^2 - \omega^2 - i\omega\gamma} \quad (2.11)$$

with squared amplitude of

$$|\Xi_0|^2 = \frac{f_0^2}{(\omega_0^2 - \omega^2)^2 + \omega^2 \gamma^2}. \quad (2.12)$$

The resulting behavior can be seen in Figure 2.1 for a variety of damping coefficients  $\gamma$  [4].

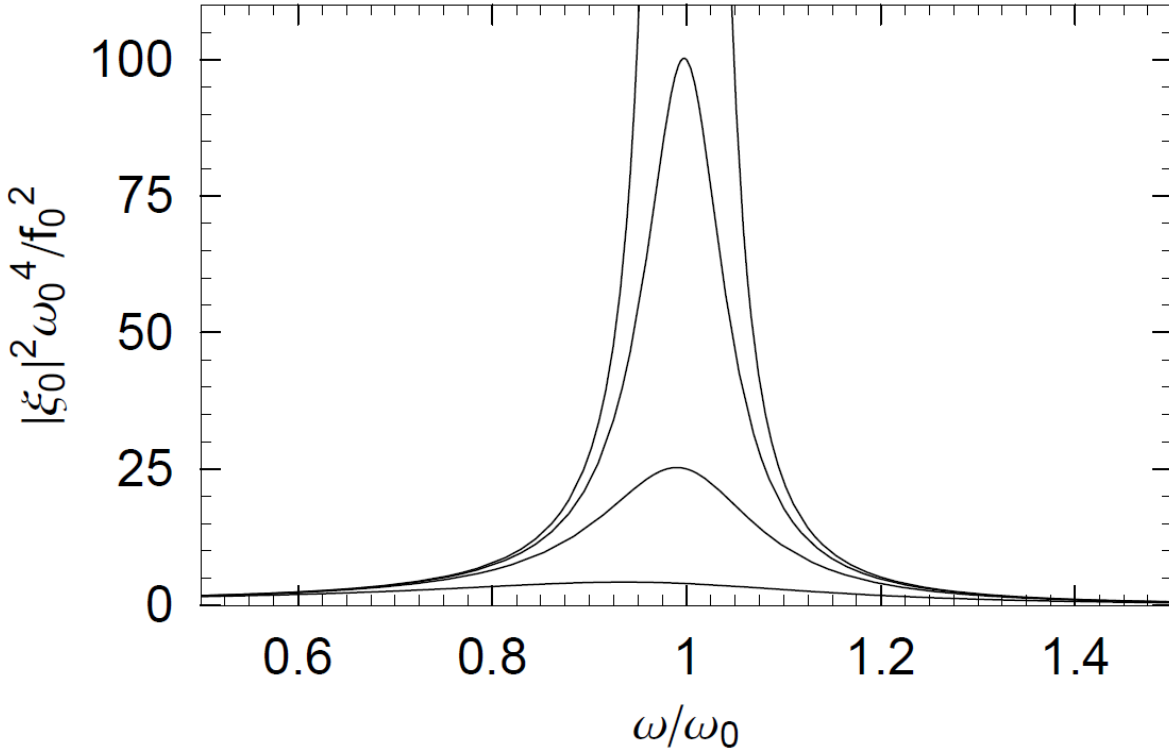


Figure 2.1: Resonant curves for damped, driven harmonic oscillator with  $\gamma = 0.5, 0.2, 0.1, 0$

Again, it is easy to see that the maximum response will be shifted slightly depending on the strength of the damping. This shift can be neglected for  $\gamma \ll \omega_0$ , and as demonstrated earlier, this is a very good approximation for superconducting resonators. Another important feature of these curves is the characteristic width of each curve. This width ( $\Delta\omega$ ), defined as the width at the level that is 3 dB below the maximum response, is equal to  $2\gamma$  where  $\gamma$  is the damping parameter. An alternative and equivalent definition of the Quality Factor is  $Q = \omega / \Delta\omega$ .

The phase response of  $\Xi$  is also of interest. This phase  $\phi$  can be interpreted as the difference in phase between the driving term and the response of the resonator, and is an important quantity for resonator control.

$$\tan(\phi) = \frac{\Im \Xi_0}{\Re \Xi_0} = \frac{\omega \gamma}{\omega_0^2 - \omega^2} = \left(\frac{\omega}{\omega_0}\right) \frac{1}{1 - \left(\frac{\omega}{\omega_0}\right)^2} \left(\frac{\gamma}{\omega_0}\right) \quad (2.13)$$

A plot of  $\phi$  can be seen in Figure 2.2. The most important feature of this behavior is the nearly linear region near resonance. Most cavity control systems treat the cavity response as linear and must operate in this region to remain stable.

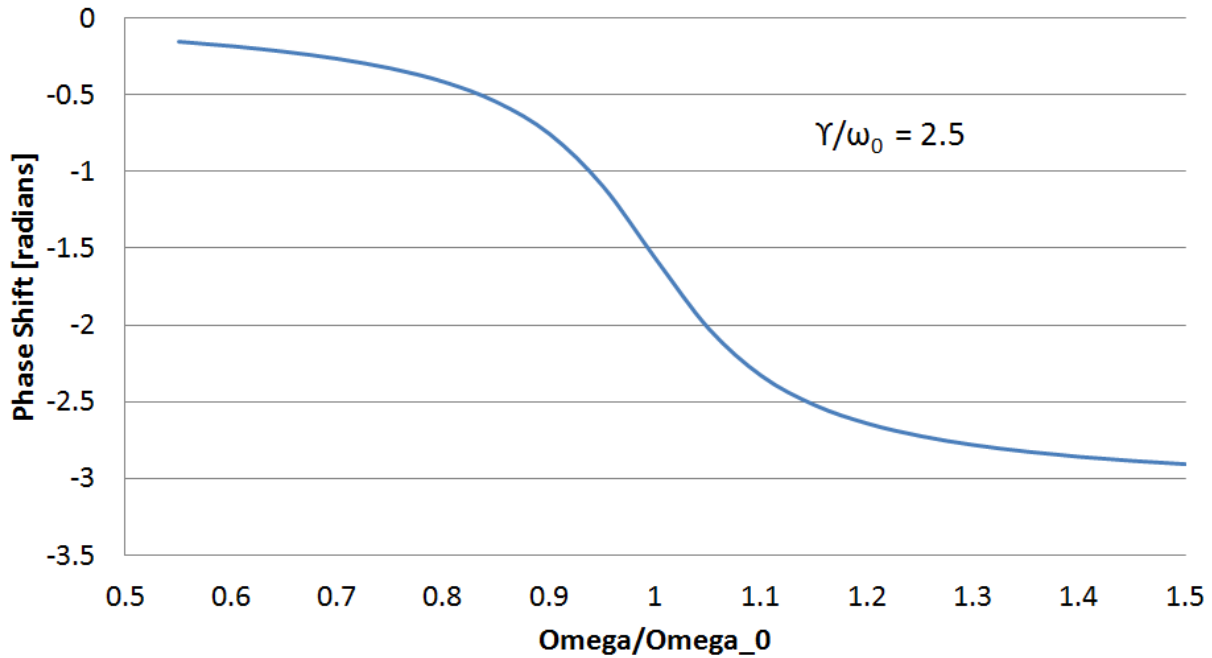


Figure 2.2: Oscillator phase shift compared to driving term versus detuning. Note the nearly linear region near resonance.

### 2.2.4 Special Case: The Duffing Equation

As we shall see, certain non-linear behavior in superconducting resonators in operation can be well modeled by the Duffing Equation. The Duffing Equation adds a weakly non-linear term to the restoring force such that

$$\frac{d^2x}{dt^2} + \gamma \frac{dx}{dt} + \omega_0^2 x + \alpha x^3 = f_0 \cos \omega t. \quad (2.14)$$

For the purposes of this application, it can be assumed both the damping, driving, and non-linear terms are small compared to the frequency  $\omega_0$ . Additionally, we will only look for solutions where  $\omega \simeq \omega_0$ . Using the standard van der Pol transformation [5], seen in Figure 2.3, we transform into a rotating coordinate frame. Using the transformations

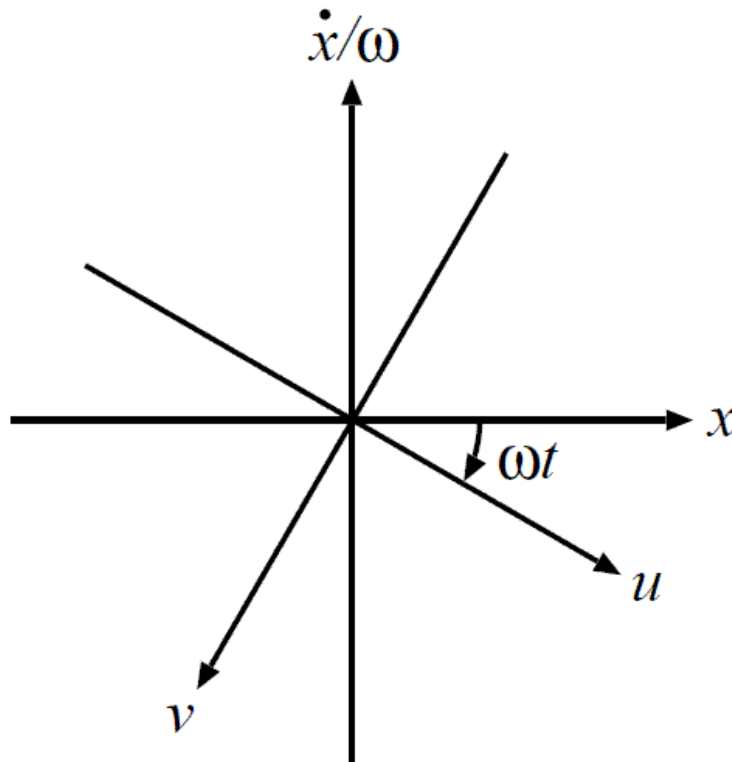


Figure 2.3: Van der Pol coordinate transformation into a frame rotating at  $\omega$ .

$$u = x \cos \omega t - \frac{\dot{x}}{\omega} \sin \omega t \quad (2.15)$$

and

$$v = -x \sin \omega t - \frac{\dot{x}}{\omega} \cos \omega t, \quad (2.16)$$

we arrive at the following differential equations for  $u$  and  $v$ :

$$\begin{aligned} \dot{u} = \frac{1}{\omega} [-(\omega^2 - \omega_0^2)(u \cos \omega t - v \sin \omega t) - \omega\gamma(u \sin \omega t + v \cos \omega t) \\ + \alpha(u \cos \omega t - v \sin \omega t)^3 - f_0 \cos \omega t] \sin \omega t \end{aligned} \quad (2.17)$$

$$\begin{aligned} \dot{v} = \frac{1}{\omega} [-(\omega^2 - \omega_0^2)(u \cos \omega t - v \sin \omega t) - \omega\gamma(u \sin \omega t + v \cos \omega t) \\ + \alpha(u \cos \omega t - v \sin \omega t)^3 - f_0 \cos \omega t] \cos \omega t. \end{aligned} \quad (2.18)$$

Because we are assuming small non-linearities and constant frequency ( $\omega$ ), we are only interested in the average behavior of these functions. Averaging over a period of  $2\pi/\omega$ , we get

$$\dot{u} = \frac{1}{2\omega} \left( -\omega\gamma u + (\omega^2 - \omega_0^2)v - \frac{3}{4}\alpha(u^2 + v^2)v \right) \quad (2.19)$$

and

$$\dot{v} = \frac{1}{2\omega} \left( \omega\gamma v - (\omega^2 - \omega_0^2)u + \frac{3}{4}\alpha(u^2 + v^2)u - f_0 \right). \quad (2.20)$$

In reality, these are not the values of interest for our resonator. For more meaningful results, we again transform these quantities into the magnitude ( $r = \sqrt{u^2 + v^2}$ ) and phase ( $\phi =$

$\arctan(v/u)$  in the rotating frame. This results in the following differential equations:

$$\dot{r} = \frac{1}{2\omega} (-\omega\gamma r - f_0 \sin \phi) \quad (2.21)$$

and

$$\dot{\phi} = \frac{1}{2\omega} \left( -(\omega^2 - \omega_0^2)r + \frac{3}{4}\alpha r^3 - f_0 \cos \phi \right). \quad (2.22)$$

Again, we can simplify by assuming a steady state solution:  $\dot{r} = \dot{\phi} = 0$ . The resulting amplitude and phase plots can be seen in Figures 2.4 and 2.5, and the non-linear response is evident. Because of this detuning, both the amplitude and phase become multi-valued for certain ranges of detuning, and if the effect is severe enough, controlling the resonator behavior can become prohibitively challenging.

## 2.2.5 Electromagnetic Fields as a Harmonic Oscillator

To this point, I have focused on the formalism for a generic harmonic oscillator with damping and driving terms. Occasionally, I have motivated certain approximations and simplifications as relevant to accelerating resonators without proof, but now I wish to demonstrate the applicability of this formalism to electromagnetic resonators in preparation for the rest of the chapter. For a (much) more rigorous treatment of this material, the reader is directed to Chapter 7 of J.D. Jackson's excellent book "Classical Electrodynamics" [6].



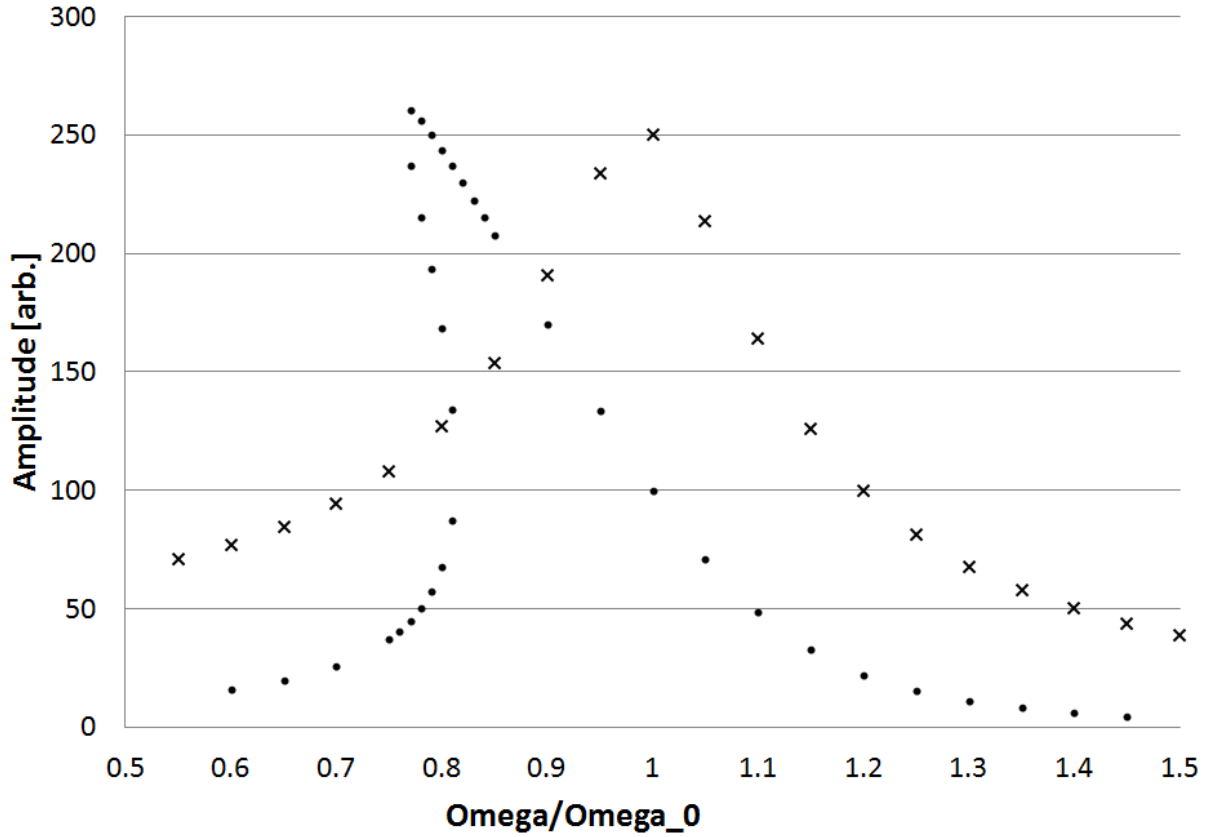


Figure 2.4: Oscillator amplitude versus detuning. Circles represent  $\alpha = -0.002$ , crosses represent  $\alpha = 0$ .

Maxwell's Equations govern all electromagnetic behavior. In free space, these equations are

$$\nabla \cdot B = 0 \tag{2.23}$$

$$\nabla \times E + \frac{\partial B}{\partial t} = 0 \tag{2.24}$$

$$\nabla \cdot D = 0 \tag{2.25}$$

$$\nabla \times H - \frac{\partial D}{\partial t} = 0 \tag{2.26}$$

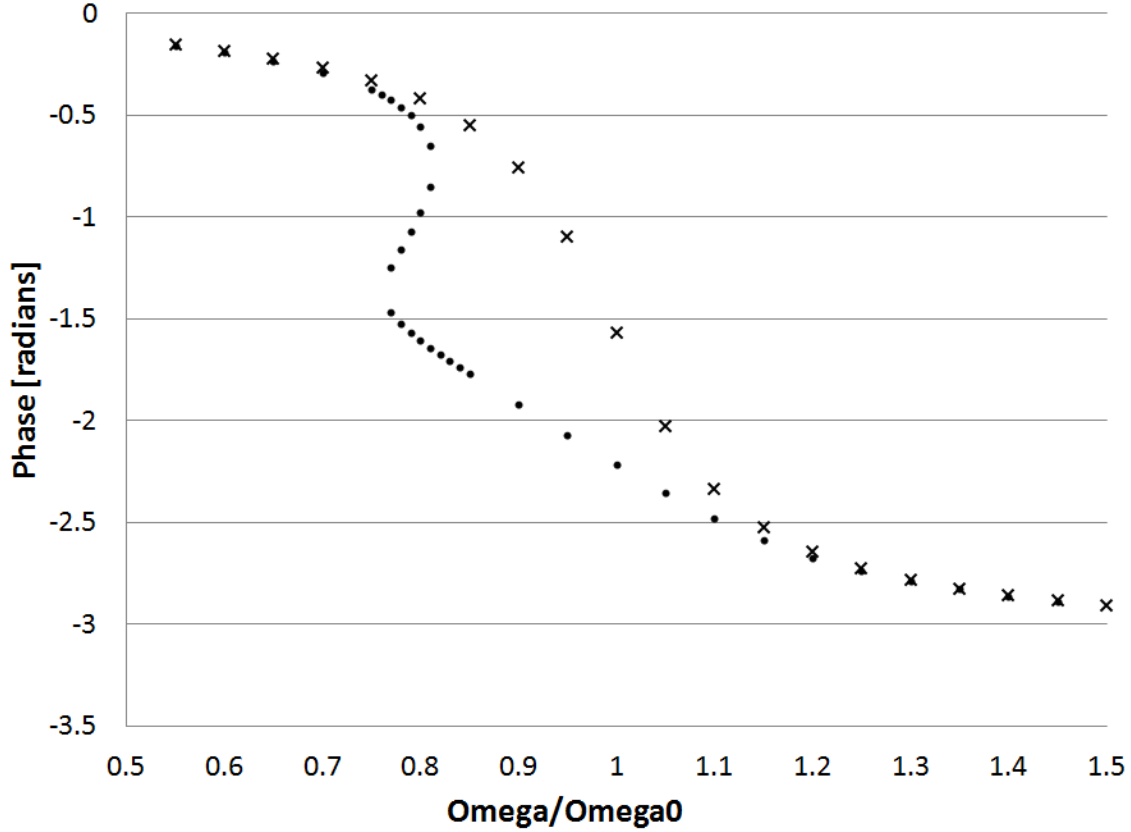


Figure 2.5: Oscillator phase versus detuning. Circles represent  $\alpha = -0.002$ , crosses represent  $\alpha = 0$ .

where  $E$  is the electric field,  $B$  is the magnetic field, and  $D$  (equal to  $\epsilon_0 E$  in this case) is the electric displacement field. Assuming a harmonic time dependence of the form  $e^{-i\omega t}$  gives

$$\nabla \cdot B = 0 \quad (2.27)$$

$$\nabla \times E - i\omega B = 0 \quad (2.28)$$

$$\nabla \cdot D = 0 \quad (2.29)$$

$$\nabla \times H + i\omega D = 0 \quad (2.30)$$

From this form, we can construct an arbitrary solution using Fourier superposition. Assuming that we are in a region where there are no losses ( $\mu$  and  $\epsilon$  are real and positive),

Maxwell's Equations reduce to

$$\nabla \times E - i\omega B = 0 \quad (2.31)$$

$$\nabla \times B + i\omega\mu\epsilon E = 0 \quad (2.32)$$

where the divergence equations can be found from taking the divergences of these two equations. Combining these two equations we get the Helmholtz wave equations:

$$\nabla^2 E + \mu\epsilon\omega^2 E = 0 \quad (2.33)$$

$$\nabla^2 B + \mu\epsilon\omega^2 B = 0 \quad (2.34)$$

A solution to equations of this form is a plane wave of the form  $e^{ikx - i\omega t}$ , where  $k = \sqrt{\mu\epsilon}\omega$  is the wave number. While solutions of this form are discussed many places at great length, the harmonic behavior allows us to use the same differential formulations to treat the resonator. For the remainder of this document, we will only consider harmonic behavior in vacuum where  $\epsilon = \epsilon_0$  and  $\mu = \mu_0$  with  $c^2\epsilon_0\mu_0 = 1$ .

## 2.3 A Simple Electromagnetic Resonator - The Pillbox Cavity

This section will provide a treatment of the most basic resonator shape, the pillbox cavity. The geometry and electromagnetic mode structure will be motivated and the performance of this cavity as an accelerating resonator will be quantified. Derivation and description of generic cavity figures of merit will be provided and derived for this geometry.

### 2.3.1 Cylindrical Waveguide Modes

Electromagnetic fields assume a certain form near a perfect conductor. Because a perfect conductor allows no field penetration into the surface and can sustain any currents required to expel the field lines, the fields at the surface of the perfect conductor must satisfy:

$$\hat{n} \times \vec{E} = 0, \quad \hat{n} \cdot \vec{H} = 0 \quad (2.35)$$

where  $\hat{n}$  is the conductor surface's normal vector. Let us consider a cylindrical waveguide of radius  $R$  that is infinite in length. Defining our cylindrical coordinate system in the usual way, we can use the generalized plane wave solution to the Helmholtz equation derived in the previous section, we can assume the fields take the form

$$\vec{E}(\vec{x}, t) = \vec{E}(\rho, \phi) e^{ikz - i\omega t} \quad (2.36)$$

$$\vec{H}(\vec{x}, t) = \vec{H}(\rho, \phi) e^{ikz - i\omega t}. \quad (2.37)$$

For the purposes of an accelerating cavity, it is desired to have longitudinal electric fields with no longitudinal magnetic fields, i.e.,  $B_z = 0$ . Additionally, we know that the dependence of the fields on  $\phi$  must be periodic, so we assume a dependence of the form  $e^{im\phi}$  where  $m$  is an integer. This gives us a form for the electric field of

$$E_z(\rho, \phi, z, t) = f(\rho) e^{ikz - i\omega t - im\phi} \quad (2.38)$$

which we can plug into the wave equation:

$$\frac{1}{c^2} \frac{\partial^2 F}{\partial t^2} = \nabla^2 F \implies \frac{1}{\rho} \frac{d}{d\rho} \rho \frac{df}{d\rho} - \frac{m^2}{r^2} f + \left( \frac{\omega^2}{c^2} - k^2 \right) f = 0 \quad (2.39)$$

to get the form of  $f(\rho)$ . The solution of this equation is given by standard Bessel functions  $f(\rho) = E_0 J_m(k_\perp \rho)$  where  $m$  is the order of the Bessel function and

$$k_\perp = \frac{1}{c} \sqrt{\omega^2 - c^2 k^2}. \quad (2.40)$$

To satisfy the boundary conditions at  $\rho = R$ ,  $E_z$  must be zero. This requires that  $k_\perp R$  is equal to one of the Bessel zeros,  $j_{m,n}$  (where  $n$  is an integer indicating the zero), giving  $k_\perp = j_{m,n}/R$ . Eliminating  $k_\perp$  from our equations gives our definition of the wave number  $k$  for this geometry:

$$k_{m,n} = \pm \left( \frac{\omega^2}{c^2} - \frac{j_{m,n}^2}{R^2} \right)^{1/2}. \quad (2.41)$$

It is of interest to note that this gives a lower bound on the frequency for a traveling wave solution. For  $\omega j_{m,n} c/R$ , the wave number becomes imaginary, resulting in a solution known as an “evanescent” wave. This frequency is known as the “cut-off” frequency, with larger diameter waveguides able to support lower frequencies. This wave exponentially decays/increases as it propagates, and is of interest in the study of resonators only for study of mode propagation into and out of the resonator through beam pipes or other ports. For the remainder of this section, we will only consider traveling wave solutions. Now that the  $E_z$  has been defined and remembering that  $B_z = 0$ , we can use  $\nabla \times E = i\omega B$  and  $c^2 \nabla \times B = -i\omega E$  to

find the remaining components of both fields:  $E_\phi$ ,  $E_\rho$ ,  $B_\phi$ ,  $B_\rho$ . These component are

$$E_\rho = E_0 \frac{ik_{m,n}R}{j_{m,n}} J'_m \left( j_{m,n} \frac{\rho}{R} \right) e^{ik_{m,n}z - i\omega t - im\phi} \quad (2.42)$$

$$E_\phi = -E_0 \frac{mk_{m,n}R^2}{\rho j_{m,n}^2} J_m \left( j_{m,n} \frac{\rho}{R} \right) e^{ik_{m,n}z - i\omega t - im\phi} \quad (2.43)$$

$$B_\rho = E_0 \frac{m\omega R^2}{c^2 \rho j_{m,n}^2} J_m \left( j_{m,n} \frac{\rho}{R} \right) e^{ik_{m,n}z - i\omega t - im\phi} \quad (2.44)$$

$$B_\phi = E_0 \frac{i\omega R}{c^2 j_{m,n}} J'_m \left( j_{m,n} \frac{\rho}{R} \right) e^{ik_{m,n}z - i\omega t - im\phi} \quad (2.45)$$

where  $J'_m$  is the derivative of the  $m$ th order Bessel function. Standard convention designates these modes as  $TM_{mn}$  for *T*ransverse *M*agnetic modes where the index  $m$  is the azimuthal order and index  $n$  is the radial order. It is worth noting that the boundary condition  $E_\phi(\rho = R) = 0$  is automatically satisfied because this component has the same radial dependence as  $E_z$ .

This derivation for *TM* modes is based on the condition that  $B_z = 0$ . One can follow the same approach starting with the condition of  $E_z = 0$  to obtain another family of modes, *Transverse Electric (TE)* modes. As these are not useful for accelerator applications, they are beyond the scope of this work.

### 2.3.2 From Traveling Waves to Standing Waves

The goal of this section is to describe a cavity, not a waveguide. To this end, we will take a section of waveguide and terminate it with conducting faces at  $z = 0$  and  $z = L$ . In order to satisfy these additional boundary conditions with *TM* modes, we take two modes with

equal  $m$  and  $n$  but with opposite values of  $k$ . This is equivalent to combining identical waves traveling in opposite directions. The equations

$$\frac{1}{2}(e^{ik_{m,n}z} + e^{-ik_{m,n}z}) = \cos(k_{m,n}z) \quad (2.46)$$

$$\frac{1}{2}(k_{m,n}e^{ik_{m,n}z} - k_{m,n}e^{-ik_{m,n}z}) = ik_{m,n} \sin(k_{m,n}z) \quad (2.47)$$

can be plugged into the full field components, and both  $E_\rho$  and  $E_\phi$  gain a factor of  $\sin(k_{m,n}z)$ . This means that the boundary condition requiring these components to be zero at the  $z = 0$  plane is automatically satisfied, and the boundary condition at  $z = L$  can be satisfied by requiring  $k_{m,n}L = l\pi$  where  $l$  is an integer index that gives the longitudinal mode order. It is of interest to note that these new boundary conditions are now also satisfied for the magnetic fields. The resulting field components are

$$E_z = E_0 J_m \left( j_{m,n} \frac{\rho}{R} \right) \cos \left( \frac{l\pi z}{L} \right) e^{-i\omega t - im\phi} \quad (2.48)$$

$$E_\rho = -E_0 \frac{l\pi R}{j_{m,n}L} J'_m \left( j_{m,n} \frac{\rho}{R} \right) \sin \left( \frac{l\pi z}{L} \right) e^{-i\omega t - im\phi} \quad (2.49)$$

$$E_\phi = -E_0 \frac{iml\pi R^2}{\rho j_{m,n}^2 L} J_m \left( j_{m,n} \frac{\rho}{R} \right) \sin \left( \frac{l\pi z}{L} \right) e^{-i\omega t - im\phi} \quad (2.50)$$

$$B_\rho = E_0 \frac{m\omega R^2}{c^2 \rho j_{m,n}^2} J_m \left( j_{m,n} \frac{\rho}{R} \right) \cos \left( \frac{l\pi z}{L} \right) e^{-i\omega t - im\phi} \quad (2.51)$$

$$B_\phi = E_0 \frac{i\omega R}{c^2 j_{m,n}} J'_m \left( j_{m,n} \frac{\rho}{R} \right) \cos \left( \frac{l\pi z}{L} \right) e^{-i\omega t - im\phi}. \quad (2.52)$$

Note that this also changes the form of the wave number, resulting in a discrete dispersion relation instead of a continuous curve:

$$\frac{\omega_{m,n,l}^2}{c^2} = \pm \left[ \left( \frac{l\pi}{L} \right)^2 + \frac{j_{m,n}^2}{R^2} \right]^{1/2}. \quad (2.53)$$

This shift to a discrete set of modes (conventionally referred to as  $TM_{mnl}$  modes) can be repeated for  $TE$  modes as well.

### 2.3.3 The “Fundamental Mode” and its Properties

For use as an accelerating cavity, the  $TM_{010}$  mode (called the “fundamental mode”) gives the best performance. The justification for this is simple when remembering that our desire was to have only the accelerating electric field component be non-zero near the beam axis. The field components for this mode are very simple:

$$E_z = E_0 J_0 \left( \frac{2.405\rho}{R} \right) e^{-i\omega t} \quad (2.54)$$

$$H_\phi = \frac{E_0}{\eta} J_1 \left( \frac{2.405\rho}{R} \right) e^{-i\omega t + i3\pi/2} \quad (2.55)$$

where

$$\eta = \sqrt{\frac{\mu_0}{\epsilon_0}} \cong 376.7 \, \Omega \quad (2.56)$$

is the impedance of free space. The frequency for this mode does not depend on the length of the cavity  $L$ , reducing to

$$\omega_{010} = \frac{2.405c}{R}. \quad (2.57)$$



For this mode to successfully accelerate beam, ports must be added for the beam to enter and exit the cavity. The rest of this section will not include these ports, as they are extremely challenging to model analytically. This is a perturbation best studied by computer simulations, which is a subject covered extensively in Chapter 3.

### 2.3.4 The Interaction of Conductors and Electromagnetic Fields

There is no material that will not dissipate power when an RF field is applied to its surface.

The losses in a cavity are given by

$$\frac{dP}{dA} = \frac{1}{2}R_s|H|^2 \quad (2.58)$$

where  $dP/dA$  is the dissipated power per unit area and  $H$  is the local magnetic field. The remaining quantity is the surface resistivity. For a normal conducting material, this can be on the order of  $m\Omega$ , and for a high quality superconducting surface, this can be on the order of  $n\Omega$ . These losses are generated by the surface currents induced by the changing magnetic fields in the resonator. Remembering that, for an RF cavity,

$$E = E_0e^{-i\omega t} \quad (2.59)$$

and defining the electrical conductivity  $\sigma$  such that

$$\vec{j} = \sigma \vec{E} \quad (2.60)$$

where  $\vec{j}$  is the surface current, we can show that, for a good conductor,

$$\nabla^2 \vec{E} = \tau_n^2 \vec{E} \quad (2.61)$$

where  $\tau_n^2 = \sqrt{i\omega\sigma\mu_0}$ . For a simple geometry, such as an infinite half-plane of conductor at  $x > 0$  with an applied electric field that is only in the  $z$  direction, the solution to this equation is

$$E_z = E_0 e^{-\tau_n x} = E_0 e^{\frac{-x}{\delta}} e^{\frac{-ix}{\delta}} \quad (2.62)$$

where

$$\delta = \frac{1}{\sqrt{\pi f \mu_0 \sigma}}. \quad (2.63)$$

This quantity,  $\delta$ , is called the “skin depth”, and gives a characteristic length for how deeply the electromagnetic fields penetrate the conductor. As an example of this, a copper surface with  $\sigma = 6 \times 10^7$  S/m at a frequency of 1 GHz has a skin depth of approximately  $2 \mu\text{m}$ . Also note that as the frequency increases, this skin depth decreases. Because this skin depth is so small compared to the wavelength of the resonator, it can be ignored in the treatment of the cavity properties. In the geometry above, the current density and losses can also be quantified. The current and field of this configuration are

$$j_z = j_0 e^{-\tau_n x}, H_y = H_0 e^{-\tau_n x}. \quad (2.64)$$

Using these, the surface impedance  $Z_0$  can be calculated where

$$Z_0 = \frac{E_0}{I} \quad (2.65)$$

with  $I$  being the current. The losses come from the real part of the surface impedance, where the imaginary part of this is the reactance. Calculation yields

$$R_s = \sqrt{\frac{\pi f \mu_0}{\sigma}} = \frac{1}{\sigma \delta}. \quad (2.66)$$

Note that these calculations are done for normal conducting materials, superconducting materials and their properties will be discussed later in this chapter.

### 2.3.5 Cavity Figures of Merit - Accelerating Voltage

All cavities are judged by a small set of electromagnetic figures of merit. These figures of merit fall into two different categories: efficiency and scaling. Efficiency figures of merit are measures of how efficiently the cavity performs and do not scale with stored energy. The scaling figures of merit are all figures of merit that do scale with the stored energy of the cavity. There are three major scaling figures of merit. First, and perhaps most important, is the Accelerating Voltage ( $V_{acc}$ ). This is the measure of how much energy a charged particle passing through a cavity will gain, and it is defined as

$$V_{acc} = \int_{-\infty}^{+\infty} E_{acc}(z) \cos(\omega t + \phi) dz = \int_{-\infty}^{+\infty} E_{acc}(z) \cos\left(\frac{\omega z}{\beta c} + \phi\right) dz \quad (2.67)$$

where  $z$  axis is the beam axis,  $\beta = v/c$ ,  $\phi$  is a phase offset that maximizes  $V_{acc}$  and assuming that  $\beta$  doesn't change. This last approximation is equivalent to saying that the energy gained in the cavity is small compared to its total energy. This approximation is not valid if a high degree of accuracy is required, say, for particle tracking. Practically, this can be calculated as

$$V_{acc} = \sqrt{\left(\int_{-\infty}^{+\infty} E_{acc} \sin(\omega t) dz\right)^2 + \left(\int_{-\infty}^{+\infty} E_{acc} \cos(\omega t) dz\right)^2}. \quad (2.68)$$

For the pillbox cavity, this integral has an analytic solution because the accelerating electric field is constant in  $z$ .

$$V_{acc} = \left| \int_{-\infty}^{+\infty} E_{acc}(z) e^{i\omega t + i\phi} dt \right| = E_0 \left| \int_0^L e^{i\omega_0 z / \beta c} dz \right| = LE_0 \frac{\sin\left(\frac{\omega_0 L}{2\beta c}\right)}{\left(\frac{\omega_0 L}{2\beta c}\right)} \quad (2.69)$$

The length of the cavity, at this stage, remains unspecified. An important consideration of the length is that this type of cavity is often operated in series as can be seen in Figure 2.6, with each cavity being  $\pi$  ahead of the previous one in phase. It is obvious to see that it is desirable to have the time it takes the particle to transit the cavity be equal to the time it takes the fields to reverse:

$$\frac{L}{\beta c} = \frac{\pi}{\omega_0}; L = \frac{\beta \lambda}{2}. \quad (2.70)$$

### 2.3.6 Cavity Figures of Merit - Transit Time Factor

Given a cavity length that is appropriate for the velocity of particle being accelerated, it is clear that there is still some loss in accelerating efficiency because the fields are varying in

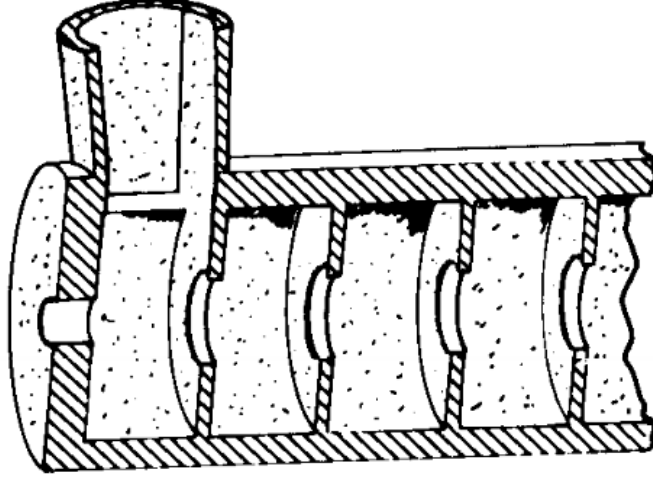


Figure 2.6: An example of pillbox type cavities coupled together.

time. The maximum acceleration that could be expected from a cavity of this type would be

$$V_0 = \int_{-\infty}^{+\infty} |E_{acc}(z)| dz = LE_0. \quad (2.71)$$

The ratio of  $V_{acc}$  to  $V_0$  gives the efficiency figure of merit called the Transit Time Factor ( $TTF$ ). For the pillbox cavity with a length of  $\beta\lambda/2$ , the  $TTF$  is

$$TTF = \frac{V_{acc}}{V_0} = \frac{\sin\left(\frac{\omega_0 L}{2\beta c}\right)}{\left(\frac{\omega_0 L}{2\beta c}\right)} = \frac{\sin\left(\frac{\pi}{2}\right)}{\left(\frac{\pi}{2}\right)} = \frac{2}{\pi}. \quad (2.72)$$

It is important to note that, in reality, a given length of cavity  $L$  gives an *optimum* particle velocity  $\beta_{opt}$ . This means that the  $TTF$  varies with  $\beta$  for a given cavity geometry:

$$TTF(\beta) = \frac{\sin\left(\frac{\omega_0 L}{2\beta c}\right)}{\left(\frac{\omega_0 L}{2\beta c}\right)} = \frac{\sin\left(\frac{\pi\beta_{opt}}{2\beta}\right)}{\left(\frac{\pi\beta_{opt}}{2\beta}\right)}. \quad (2.73)$$

Figure 2.7 shows this curve for a cavity designed for  $\beta_{opt} = 0.50$  for 2, 4, and 8 cavities in series. Notice that as the number of synchronized cavities (“gaps”) increases, the range

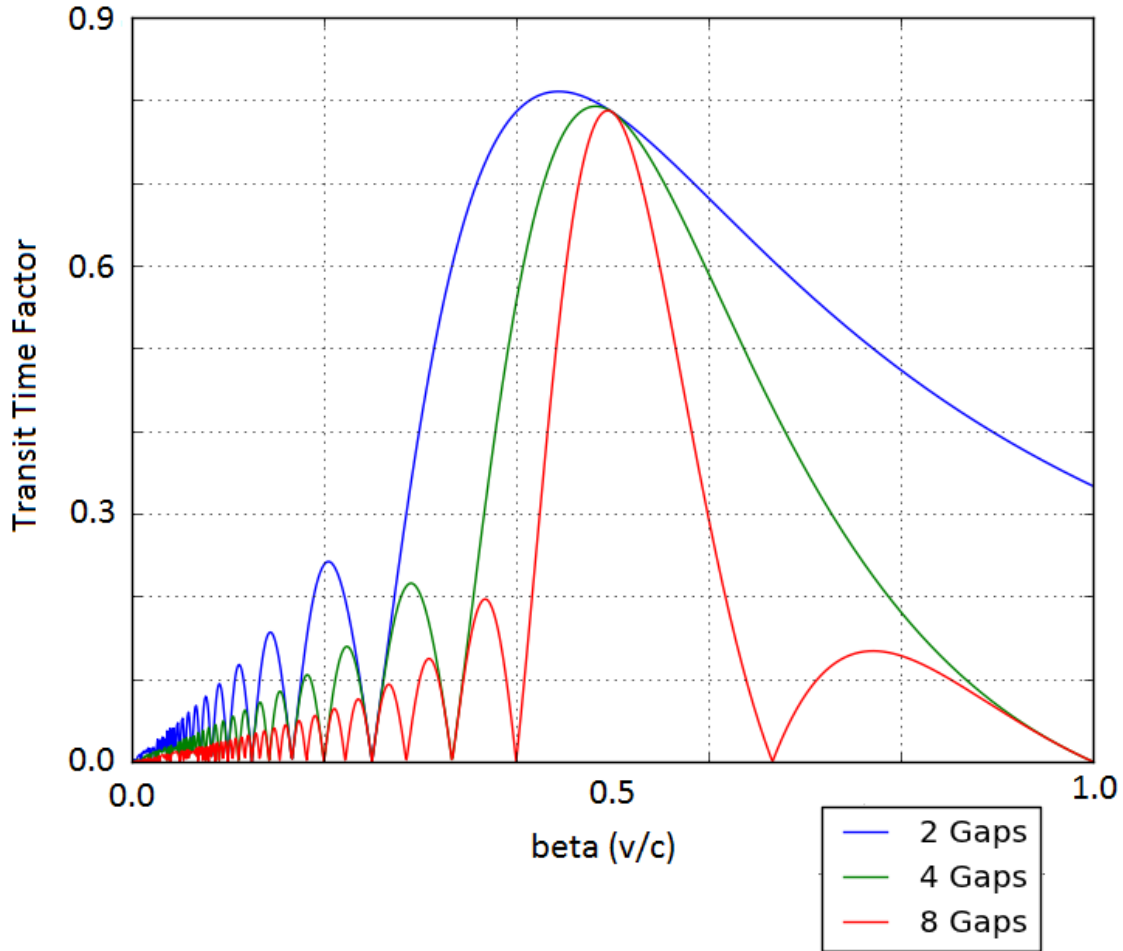


Figure 2.7: The Transit Time Factor (TTF) for 2, 4, and 8 cavities in series with  $\beta_{opt} = 0.50$ .

of velocities that can be efficiently accelerated shrinks. This is of considerable importance for an accelerator that has to accelerate a beam with a velocity that changes significantly. While larger numbers of synchronized gaps mean a higher amount of acceleration per meter of constructed accelerator, this may require more cavities designed for a variety of different  $\beta_{opt}$ . Two extreme examples of this are heavy ion and electron accelerators. An electron is such a light particle that it very rapidly approaches the speed of light, thus only requiring

one resonator geometry. To give an example of how fast this happens, remember that the International Linear Collider has a resonator designed to give roughly 30 MeV of acceleration with each resonator having 9 cells. This means that, from *rest*, an electron would be going 99%(!!!) the speed of light at the exit of the first resonator (even after including the reduction in acceleration efficiency when the electron's speed is mismatched relative to the optimum beta). For a heavy ion accelerator, the situation is much different. For a beam of uranium (common in nuclear physics), over 500,000 times as much energy (almost 2 TeV!!!) is required to reach the same velocity, even in its highest charge state. Even using the most flexible accelerating resonators (2-gap structures), this would take at least 5 different cavity designs to achieve (and it would be  $\sim 4$  km long!).

### 2.3.7 Cavity Figures of Merit - Peak Surface Electric and Magnetic Field

The remaining scaling figures of merit are the peak surface electric and magnetic fields. For the pillbox cavities, these values

$$E_{pk} = E_0 \tag{2.74}$$

$$H_{pk} = \frac{E_0}{\eta} J_1(1.84) = \frac{E_0}{647 \Omega} \tag{2.75}$$

are located on the end walls of the cavity. These values have important design implications that will be discussed at length in another section of this chapter.

### 2.3.8 Cavity Figures of Merit - Geometry and Quality Factor

The efficiency with which the resonator stores energy is of principal importance. For superconducting cavities, this is especially true because all dissipated power is exhausted into liquid helium. The figure of merit for this efficiency is the Quality Factor:

$$Q = \frac{\omega_0 U}{P_d}. \quad (2.76)$$

From our study of the harmonic oscillator, remember that we defined the quality factor as the ratio of the energy stored in the resonator to the energy lost per radian of oscillation. Inspection shows that this definition is consistent with the resonator definition. In addition to the Quality Factor, there is a figure of merit that does not depend on the surface resistance ( $R_s$ ) called the Geometry Factor. This is defined as

$$G = R_s Q = \frac{\omega U}{\left(\frac{P_d}{R_s}\right)} \quad (2.77)$$

and is solely dependent on the geometry. This is a more useful figure of merit for cavity design because the  $R_s$  depends on many factors outside of the electromagnetic design such as material purity, surface quality, heat treatment of the cavity, and many more. This is also a useful figure to compare different geometries and cavities of different frequencies because it is independent of frequency [7, pp. 43-44]. To calculate the Geometry Factor for a given geometry, we must first calculate the stored energy ( $U$ ) and dissipated power ( $P_d$ ). Remembering that

$$\frac{dP_d}{dA} = \frac{1}{2} R_s \left| \vec{H} \right|^2 \quad (2.78)$$



where  $|\vec{H}|$  is the magnetic field at  $dA$ , and that the Geometry Factor requires  $P_d/R_s$  the equation for the total dissipated power becomes

$$\frac{P_d}{R_s} = \frac{1}{2} \int_S |\vec{H}|^2 dA \quad (2.79)$$

where  $S$  includes all RF surfaces in the cavity. Note that we are assuming that  $R_s$  is constant over the surface, which is unlikely to be strictly true. While it is expected that its value will not vary much over the surface, accurate measurements of  $R_s$  and its variation over the surface of the cavity are extremely difficult. In any case, the variation will not likely be predictable, and should not affect cavity design. In addition to  $P_d$ , we need the stored energy in the cavity. In general, the time averaged stored energy density in the cavity is [8]

$$u = \frac{1}{2} \left( \epsilon |\vec{E}|^2 + \frac{1}{\mu} |\vec{B}|^2 \right). \quad (2.80)$$

At any given time, the energy is stored in the electric and magnetic fields of the cavity. However, the total energy is fixed, and in this time-averaged form, both electric and magnetic contributions are equal. This means we can simplify this density to

$$u = \frac{\epsilon}{2} |E|^2 = \frac{1}{2\mu} |B|^2 \quad (2.81)$$

which yields

$$U = \frac{\epsilon_0}{2} \int_V |E_0|^2 dV = \frac{1}{2\mu_0} \int_V |B_0|^2 dV. \quad (2.82)$$

This gives us

$$G = R_s Q = \frac{\omega_0 \mu_0 \int_V |\vec{H}|^2 dV}{\int_S |H|^2 dA}. \quad (2.83)$$

With some calculation, these integrals can be done for the pillbox cavity as described [7, p. 46]:

$$U = \frac{\pi\epsilon_0 E_0^2}{2} J_1^2(2.405) LR^2 \quad (2.84)$$

$$P_d = \frac{\pi R_s E_0^2}{\eta^2} J_1^2(2.405) R(R+L) \quad (2.85)$$

$$G = \frac{\omega_0 \mu_0 LR^2}{2(R^2 + RL)} = \eta \frac{2.405L}{2(R+L)} = \frac{453 \frac{L}{R}}{1 + \frac{L}{R}} \Omega. \quad (2.86)$$

By remembering that we desire

$$L = \frac{\beta\lambda}{2} \quad (2.87)$$

we find that, for a pillbox cavity,

$$\frac{L}{R} = \frac{\beta\pi}{2.405} \quad (2.88)$$

which gives a Geometry Factor for ALL optimized pillbox cavities of

$$G = 257\beta \Omega. \quad (2.89)$$

As a comparison, the Facility for Rare Isotope Beams (FRIB) calls for a cavity (of a totally different geometry) designed for  $\beta = 0.29$ . An equivalent pillbox cavity would have  $G \approx 74 \Omega$  with the current FRIB cavity design having  $G = 76 \Omega$ . While a pillbox cavity is impractical at these velocities (it would require a cavity that has a diameter over 5 times its length), this demonstrates the usefulness of this figure of merit for comparison between cavities.

### 2.3.9 Cavity Figures of Merit - $R/Q$

The third major efficiency figure of merit is the  $R/Q$ . This is a measure of how efficiently the cavity transfers its stored energy to the beam passing through it. This is the ratio of the *effective* shunt impedance to the cavity's quality factor, and this is a point that needs to be stressed. There are many definitions of the shunt impedance depending on context or even convention, and I will be using the common accelerator conventional definition [7, p. 47]:

$$R_a = \frac{V_{acc}^2}{P_d} \quad (2.90)$$

in units of  $\Omega$  per cell. This is further complicated by the fact the the majority of this document will be spent discussing cavities that, while one “cell”, have two accelerating gaps. From all this, the definition of the  $R/Q$  is

$$R/Q = \frac{V_{acc}^2}{\omega_0 U}. \quad (2.91)$$

One final note is that this is the effective shunt impedance. While I will omit the *eff* subscript from  $R$ , I will be using  $V_{acc}$  instead of  $V_0$ , which is implied by “shunt impedance” in some circles. For a pillbox cavity, this can be readily calculated

$$R/Q = 150 \Omega \frac{L}{R} = 196\beta \Omega. \quad (2.92)$$

### 2.3.10 Pillbox Cavities for Low Velocity Particles

The relationship between  $R/Q$  and  $\beta$  indicates that pillbox type cavities would perform best for high velocity beams, and would perform quite poorly for very low velocity beams. This

can be seen by comparing the performance of a FRIB cavity design for  $\beta = 0.29$ , a pillbox  $R/Q \approx 57 \Omega$  compares poorly to the  $R/Q = 110 \Omega/\text{gap}$  of the current design. In addition to efficiency, there are mechanical drawbacks to using a pillbox cavity at low velocity. As has been shown, the optimum length of the accelerating gap for a pillbox cavity is  $\beta\lambda/2$ , and I will now posit that what this actually means is that the distance between *adjacent, synchronized gaps* should be

$$L_{\text{gap-to-gap}} = \left(n + \frac{1}{2}\right) \frac{\beta\lambda}{2} \quad (2.93)$$

where  $n$  is an integer. Pillbox cavities require very little space between synchronized gaps, thus for them (and a vast majority of resonators)  $n$  will be 1. This gap-to-gap distance is a more general principle of accelerating resonators, and thus can be used to compare different geometries. This scaling gives interesting results for pillbox cavities designed for very low velocity beams. FRIB calls for the first resonator to be optimized for  $\beta = 0.041$ . With a conservative gap-to-gap distance of 0.1 m, this gives a cavity with  $f = 61.5$  MHz, and a cavity radius of  $R = 0.534$  m. This cavity has very poor mechanical qualities from such a large ratio of radius to gap size, in addition to the loss in accelerating efficiency due to the small gap size.

## 2.4 Coaxial Resonators

In the previous section, we derived the mode structures and properties of resonators constructed from a terminated section of cylindrical waveguide. The scaling of these structures means they become undesirable for acceleration of very low velocity particles. Coaxial res-

onators originate from the mode structure of coaxial transmission lines. These resonators offer a practical option for lower velocity particle acceleration because they can achieve the lower fundamental frequency required for a lower optimum velocity of beam while maintaining efficiency of acceleration. In payment for this, these cavities have more complex geometries that require more material, construction, and processing cost and time. Their mode structures, scaling parameters, and figures of merit will be derived and compared with the pillbox cavity type, and their use in heavy ion accelerators will be justified.

### 2.4.1 Coaxial Transmission Line Geometry

The addition of a cylindrical inner conductor to a cylindrical waveguide significantly alters the mode structure. First, modes with longitudinal electric fields are no longer supported, and the modes of interest have no longitudinal magnetic fields, giving these modes their designation as *TEM*, or *T*ransverse *E*lectric and *M*agnetic. There are two types of termination that are of interest for this type of geometry, short and open. A short termination is the same type that was used in the previous section for pillbox cavities, a conducting plane in the  $\rho - \phi$  plane. This gives a magnetic field maximum and a zero in the electric fields at the boundary. The other type, an open, is the addition of a perfect *magnetic* conducting plane in  $\rho - \phi$ . This provides a zero in the magnetic field and a maximum in the electric field at the boundary. While this is, technically, non-physical, it is an excellent starting place for analytical calculations. An easy justification for the contained nature of modes using an effective open boundary condition can be seen from considering a length of coaxial line, shorted at one end, and connected to a cylindrical waveguide with the same radius as the outer conductor at the other end. As long as the frequency of the coaxial mode was below

the cutoff frequency of the cylindrical waveguide, it would be reflected off the transition and bound in the coaxial section. Clearly, there would be some non-ideal field profile on the length scale of the evanescent decay length, but this is only a perturbation of the mode shape. It should be noted that while you can solve for pillbox modes with open terminations, these structures will give, in reality, unbound modes that are completely impractical.

## 2.4.2 The Ideal Quarter Wave Resonator

First, we will discuss a coaxial resonator with one short termination (at  $z = L$ ) and one ideal open termination (at  $z = 0$ ), seen in Figure 2.8. Coaxial lines are typified by a radial electric field and an azimuthal magnetic field, with a  $1/\rho$  dependence in amplitude. The traveling wave formulation of this gives

$$E_\rho = -\frac{I_0\mu_0c}{2\pi\rho}e^{i\omega t+ikz} \quad (2.94)$$

$$B_\phi = \frac{I_0\mu_0}{2\pi r}e^{i\omega t+ikz}. \quad (2.95)$$

Again, summing two identical traveling waves with opposite directions of propagation

$$e^{ikz} + e^{-ikz} = 2\cos(kz) \quad (2.96)$$

$$e^{ikz} - e^{-ikz} = 2i\sin(kz) \quad (2.97)$$

we can satisfy the boundary conditions to get

$$E_\rho = \frac{E_0a}{\rho}\cos\left(\frac{p\pi z}{2L}\right)\sin(\omega t) \quad (2.98)$$

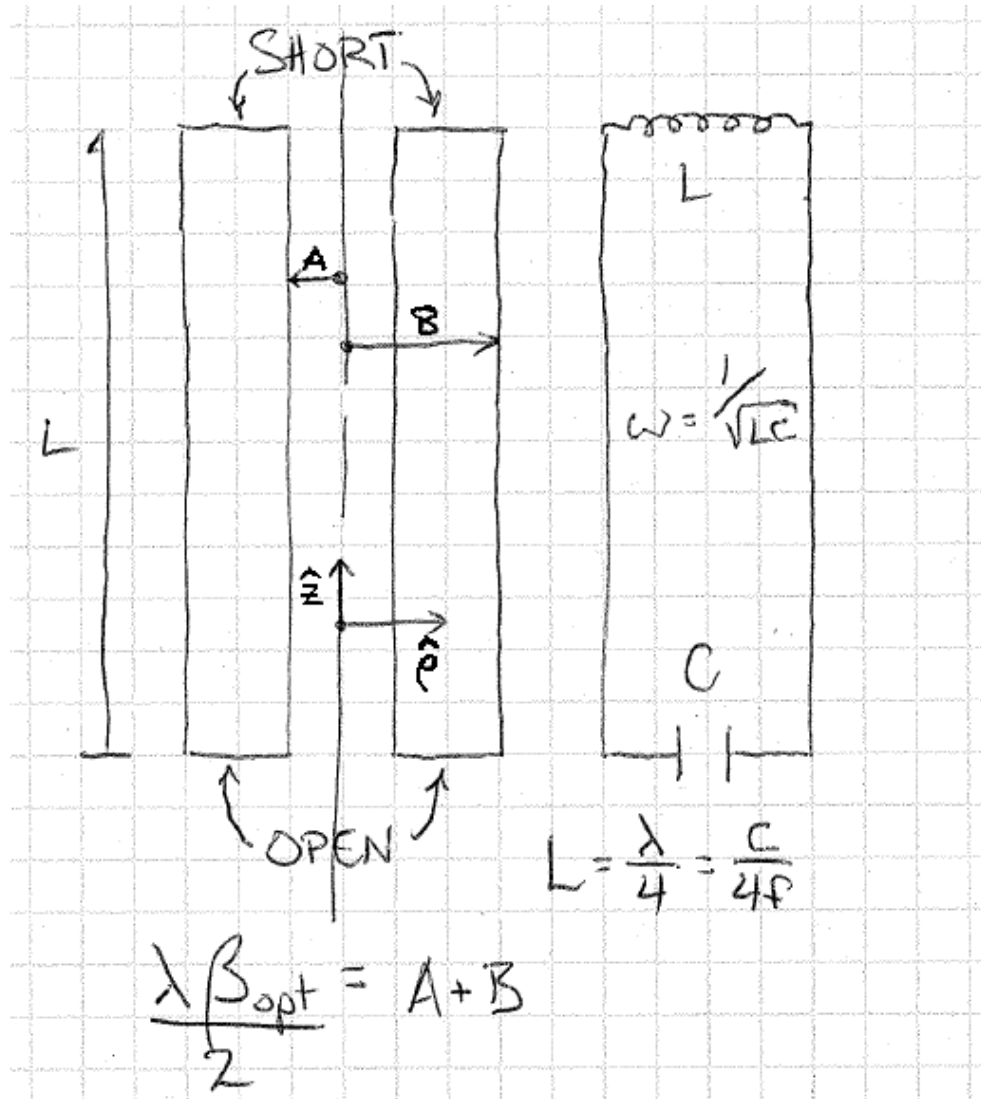


Figure 2.8: Schematic of the ideal QWR.

$$B_\phi = -\frac{E_0 a}{\rho c} \sin\left(\frac{p\pi z}{2L}\right) \cos(\omega t) \quad (2.99)$$

where  $p$  is an integer giving the order of the mode in  $z$ ,  $E_0$  is the peak surface electric field (located at  $z = 0$  and  $\rho = a$ ),  $a$  and  $b$  are the inner and outer conductor radii, and  $\omega = p\pi/2L$ . From this, it is trivial to see that the peak surface magnetic fields is  $E_0/c$  and is located at  $z = L$  and  $\rho = a$ . Rearranging this last equation gives us  $L = \lambda/4$  for the lowest mode,  $p = 1$ , giving the cavity its name: Quarter Wave Resonator (QWR). The

accelerating axis for this cavity is at  $z = \phi = 0$ , giving an ideal QWR accelerating field seen in Figure 2.9. Using these field distributions, it is straight-forward to find an ideal QWRs

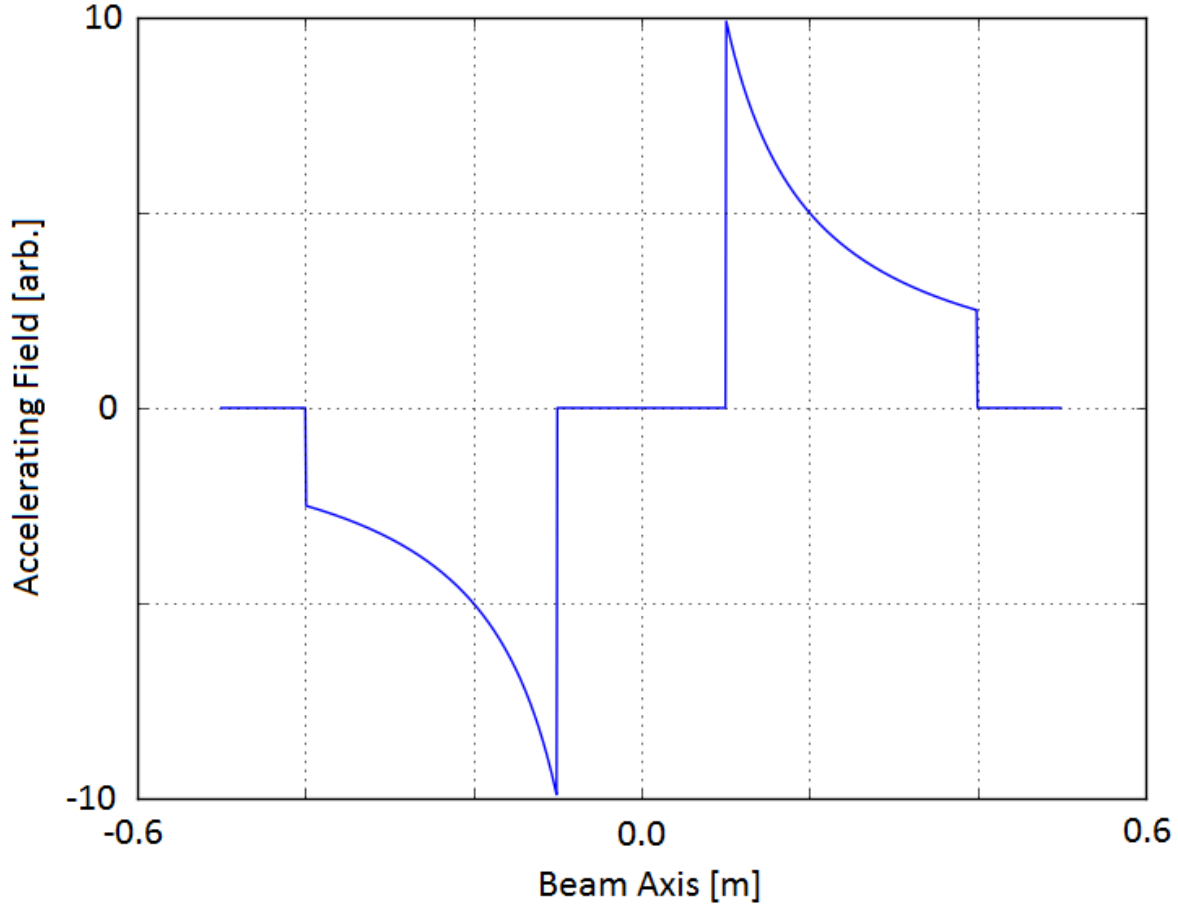


Figure 2.9: An example of the accelerating electric field for an ideal coaxial resonator. The beam axis passes radially through the cavity at  $z = 0$ .

figures of merit. The stored energy,  $U$ , is

$$U = \frac{\epsilon_0}{2} \int_V |E|^2 dV \quad (2.100)$$

$$= \frac{\epsilon_0 E_0^2 a^2}{2} \int_a^b \frac{1}{\rho} d\rho \int_0^{2\pi} d\phi \int_0^L \cos^2\left(\frac{\pi z}{2L}\right) dz \quad (2.101)$$

$$= \frac{\epsilon\pi E_0^2 \lambda}{8} \ln\left(\frac{b}{a}\right) \quad (2.102)$$



remembering that  $L = \lambda/4$ . The dissipated power,  $P_d$ , is also straight-forward to calculate:

$$\frac{P_d}{R_s} = \frac{1}{2\mu_0^2} \int_S |B|^2 dA = \frac{\pi E_0^2 a^2 \epsilon_0}{2\mu_0} \left[ \frac{\lambda}{4} \left( \frac{1}{a} + \frac{1}{b} \right) + 2 \ln \left( \frac{b}{a} \right) \right] \quad (2.103)$$

remembering to sum the contributions from the inner conductor, outer conductor, and the short plate. The dissipated power on the open termination is zero because the magnetic field there is zero. These numbers allow us to calculate the geometry factor  $G$ :

$$G = \frac{c\pi\mu_0 \ln \left( \frac{b}{a} \right)}{\left[ \frac{\lambda}{2} \left( \frac{1}{a} + \frac{1}{b} \right) + 4 \ln \left( \frac{b}{a} \right) \right]}. \quad (2.104)$$

The calculation of the optimum beta is less straight-forward for this geometry compared to the pillbox cavity. The integral is made complicated by the form of the accelerating field which gives an equation for the accelerating voltage

$$V_{acc} = 2 \int_a^b \frac{E_0 a}{x} \sin \left( \frac{\omega x}{\beta c} \right) dx \quad (2.105)$$

that does not have an analytic solution. We can sidestep this problem by remembering that we can find the optimum velocity by solving for when the derivative of  $V_{acc}$  is zero.

$$\frac{\partial V_{acc}}{\partial \beta} = 2E_0 a \int_a^b -\frac{\cos \left( \frac{\omega x}{\beta c} \right) \frac{\omega x}{\beta^2 c}}{x} dx = \frac{2E_0 a \omega}{\beta^2 c} \left[ \int_b^a \cos \left( \frac{\omega x}{\beta c} \right) dx \right] \quad (2.106)$$

which gives

$$\frac{\partial V_{acc}}{\partial \beta} = \frac{2E_0 a}{\beta} \left[ \sin \left( \frac{\omega a}{\beta c} \right) - \sin \left( \frac{\omega b}{\beta c} \right) \right] = 0. \quad (2.107)$$

Using the trigonometric identity

$$\sin u - \sin v = 2 \cos \left( \frac{u+v}{2} \right) \sin \left( \frac{u-v}{2} \right) \quad (2.108)$$

we obtain

$$\cos \left( \frac{\omega(a+b)}{2\beta c} \right) \sin \left( \frac{\omega(b-a)}{2\beta c} \right) = 0. \quad (2.109)$$

This gives conditions of

$$n\beta\lambda = b - a; \quad \frac{n\beta\lambda}{2} = b + a \quad (2.110)$$

where  $n$  is an integer. The first equation give solutions where the gap size  $(b-a)$  is extremely large, large enough for the particle to see at least one full RF period. Thus, these solutions are likely to be minima, and will be disregarded. The second equation gives the relationship that we expected for  $n = 1$ , that

$$\frac{\beta\lambda}{2} = b + a \quad (2.111)$$

which is identical to the relationship assumed for the pillbox cavity (remembering that  $b+a$  is the gap-to-gap distance). For an ideal QWR, knowing the frequency and optimum particle velocity desired specifies two of the three variables for the cavity, with the gap size  $b-a$  being the only unspecified value. A plot of  $R/Q$  and  $G$  versus gap size  $(b-a)$  can be seen in Figure 2.10. In this plot, it is easy to see that a large gap size results in a more efficient cavity. This is tempered, however, with the knowledge that the larger the gap for a given  $\beta_{opt}$ , the smaller the inner conductor diameter. The remaining figures of merit for the ideal QWR are the peak surface electric and magnetic fields. These are both on the inner conductor, and their magnitudes scale like  $1/a$ . The limit to how much we can reduce  $a$  as we increase  $R/Q$

and  $G$  is driven by the requirement of minimizing these peak surface fields.

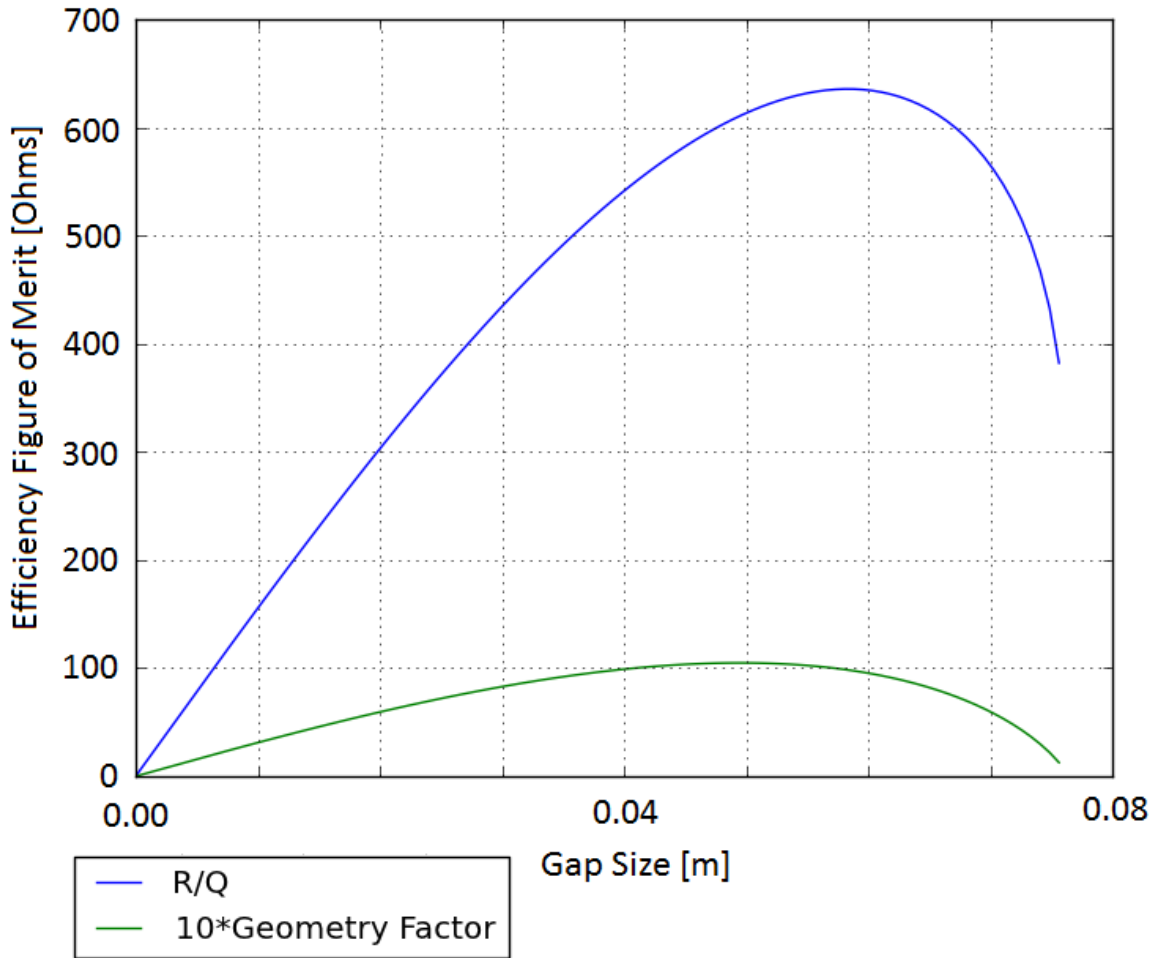


Figure 2.10:  $R/Q$  and  $G$  versus gap size for an ideal 80.5 MHz,  $\beta = 0.041$  QWR.

From Figure 2.11, we can see that the ideal open termination is not truly representative of the electric field region of a practical QWR. While a detailed treatment of QWR design is outside the scope of this document, an issue of some importance is the asymmetry of this geometry not present in the ideal QWR fields. This asymmetry causes steering electric and magnetic fields on the beam axis, especially when the frequency of the cavity is increased above  $\sim 200$  MHz. This steering can be corrected to a degree [9], but QWR usage is generally limited to applications at lower frequencies, and therefore lower velocities.

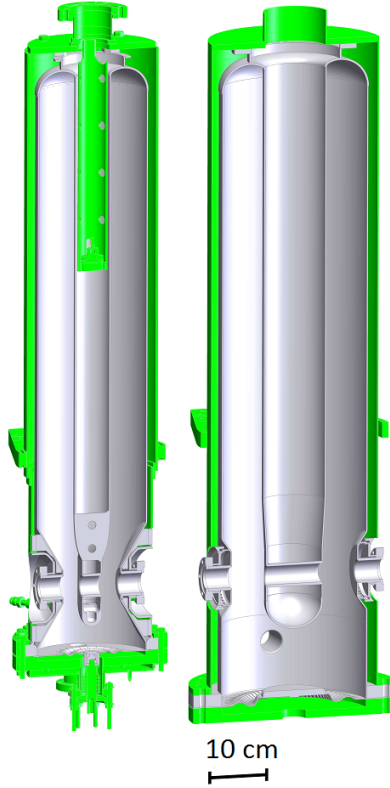


Figure 2.11: FRIB Quarter Wave Resonator designs.

### 2.4.3 The Ideal Half Wave Resonator

If, instead of a short termination at ( $z = L$ ) and an ideal open termination at ( $z = 0$ ), you have a short termination at ( $z = L/2$ ) and another short termination at ( $z = -L/2$ ) (seen in Figure 2.12), the mode structure changes, giving you a higher frequency cavity for a given length. The field profiles change to

$$E_{\rho} = \frac{E_0 a}{\rho} \cos\left(\frac{p\pi z}{L}\right) \sin(\omega t) \quad (2.112)$$

$$B_{\phi} = -\frac{E_0 a}{\rho c} \sin\left(\frac{p\pi z}{L}\right) \cos(\omega t) \quad (2.113)$$

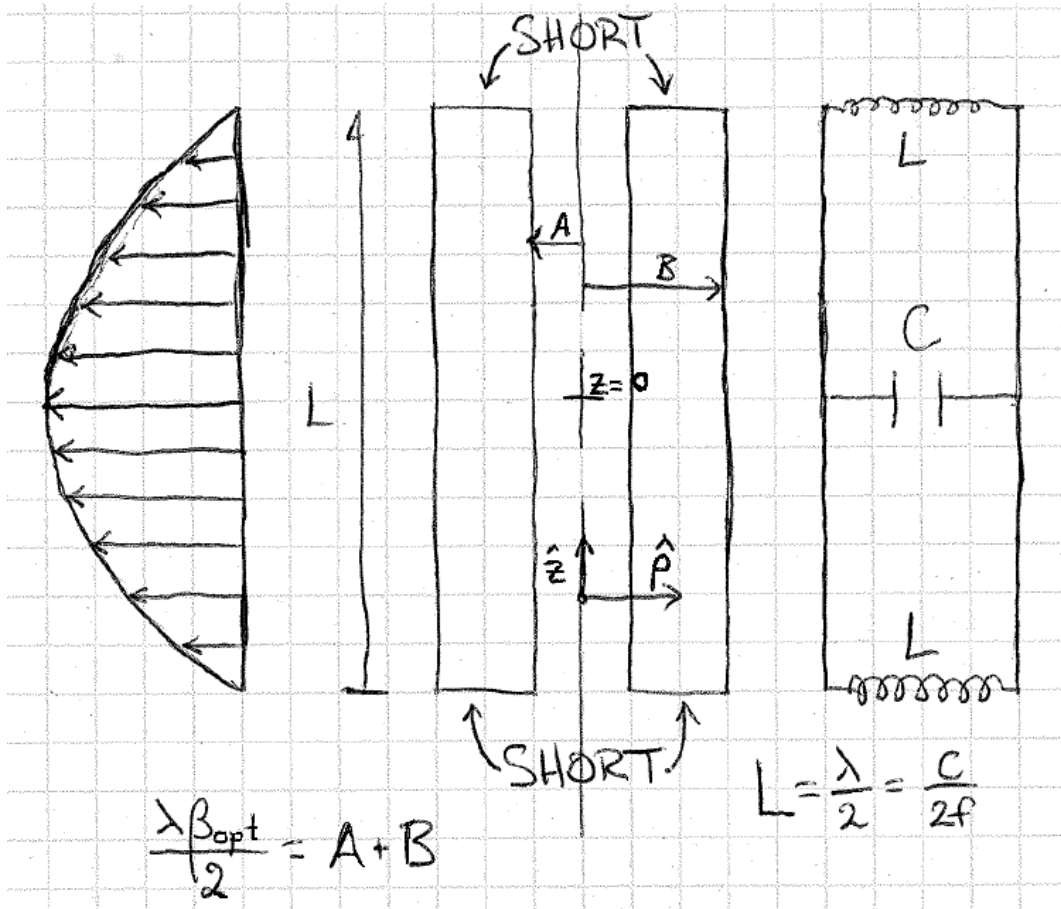


Figure 2.12: Schematic of an ideal HWR.

where  $p$  is an integer giving the order of the mode in  $z$ ,  $E_0$  is the peak surface electric field,  $a$  is the inner conductor radius, and  $\omega = pc\pi/L$ . Rearranging this last equation gives us  $L = \lambda/2$  for the lowest mode,  $p = 1$ , giving the cavity its name: Half Wave Resonator (HWR). These equations are all very similar to a QWR, and in fact are only different because of the change in definition of the length,  $L$ . An ideal HWR is effectively an ideal QWR, but reflected about the QWR's ideal open boundary condition. This means that almost all of the derived quantities for the QWR can be used here with minor modification. These

modifications give

$$U = \frac{\epsilon_0}{2} \int_V |E|^2 dV \quad (2.114)$$

$$= \frac{\epsilon_0 E_0^2 a^2}{2} \int_a^b \frac{1}{\rho} d\rho \int_0^{2\pi} d\phi \int_{-L/2}^{L/2} \cos^2\left(\frac{\pi z}{L}\right) dz \quad (2.115)$$

$$= \frac{\epsilon\pi E_0^2 a^2 \lambda}{4} \ln\left(\frac{b}{a}\right). \quad (2.116)$$

$$\frac{P_d}{R_s} = \frac{1}{2\mu_0^2} \int_S |B|^2 dA = \frac{\pi E_0^2 a^2 \epsilon_0}{\mu_0} \left[ \frac{\lambda}{4} \left( \frac{1}{a} + \frac{1}{b} \right) + 2 \ln\left(\frac{b}{a}\right) \right] \quad (2.117)$$

$$G = \frac{c\pi\mu_0 \ln\left(\frac{b}{a}\right)}{\left[ \frac{\lambda}{2} \left( \frac{1}{a} + \frac{1}{b} \right) + 4 \ln\left(\frac{b}{a}\right) \right]} \quad (2.118)$$

remembering that  $2L = \lambda$ . Additionally,

$$V_{acc} = 2 \int_a^b \frac{E_0 a}{x} \sin\left(\frac{\omega x}{\beta c}\right) dx \quad (2.119)$$

$$\frac{\beta\lambda}{2} = b + a. \quad (2.120)$$

remain identically valid for the HWR. It should be noted that, for a given length, the frequency of the structure has doubled. In addition, because the losses are driven by the magnetic fields, the losses for a given acceleration will double going from a QWR to a HWR. This will double the HWR's  $R/Q$ , but because the stored energy also doubles,  $G$  remains the same. In addition, the location of the peak surface electric and magnetic fields remain the same, with the caveat that there are not *two* peak surface magnetic fields, at  $z = L/2$  and  $z = -L/2$ . The benefit of the HWR geometry is the symmetry along the long axis, meaning

that steering fields are only generated from manufacturing errors as opposed to the inherent geometry itself. This means that the frequency limitations of the QWR do not apply to HWR, allowing acceleration of higher velocity particles.

#### 2.4.4 Coaxial Cavity Efficiency at Low Velocity

While  $V_{acc}$  for coaxial cavities is not analytic, the possible acceleration ( $V_0$ ) is. For a QWR, this leads to

$$V_{acc} = V_0 \times TTF = 2E_0 a \ln\left(\frac{b}{a}\right) \times TTF \quad (2.121)$$

which leads to

$$\frac{R}{Q} = TTF^2 \times \frac{8 \ln\left(\frac{b}{a}\right)}{\pi^2 \epsilon_0 c} \approx TTF^2 \times \ln\left(\frac{b}{a}\right) \times 300 \Omega \quad (2.122)$$

which does not scale with  $\beta$ . The  $TTF$  at optimum velocity for most designs will be  $0.85 < TTF < 0.90$ , and does not scale strongly with  $\beta$ . For most coaxial designs,  $b/a$  is between 2.5 and 3.5, although the exact definitions of  $a$  and  $b$  break down for realistic cavity designs. This means that coaxial cavities maintain their acceleration efficiency for very low velocity particles while pillbox type cavities become increasingly less efficient. To directly compare an ideal HWR to an ideal pillbox cavity, the HWR's  $R/Q$  must be halved to account for the HWR having two gaps compared to a single pillbox. This is an interesting comparison because it can be used to indicate the  $\beta$  where the  $R/Q$  of the pillbox cavity is equal to the  $R/Q$  of a coaxial cavity, giving some idea of the velocity where one geometry should replace the other:

$$\beta_{transition} = \frac{0.5 \times R/Q_{HWR}}{R/Q_{pillbox}} \approx \frac{150 \Omega \times \mathcal{F}}{150 \frac{\pi}{2.405} \Omega} \approx 0.75 \times \mathcal{F} \quad (2.123)$$

where

$$\mathcal{F} = TTF^2 \times \ln\left(\frac{b}{a}\right). \quad (2.124)$$

$\mathcal{F}$  is dependent on the design of the cavity, but for most HWR designs will be between 0.8 and 1, giving a transition  $\beta$  of  $\sim 0.7$ . This scaling is born out in the parameters of realistic cavity designs for applications around these velocities. While the  $R/Q$  scales like  $\beta$  for a pillbox and is roughly constant for coaxial cavities, the Geometry Factor is more complex. For an ideal pillbox,  $G = 257\beta \Omega$ . For a HWR, assuming a reasonable  $b/a$  of 3, the dependence is more complex:

$$G_{HWR} \approx \frac{1300\beta}{5.3 + 4.4\beta} \Omega \quad (2.125)$$

which goes to zero for small  $\beta$ , and is only  $\sim 120 \Omega$  for  $\beta = 1$ . A plot of this behavior can be seen in Figure 2.13. For comparison, an ideal HWR with  $\beta = 0.5$  would have a Geometry Factor of  $\sim 80 \Omega$ , where the realistic FRIB design for a similar cavity has a Geometry Factor of  $\sim 100 \Omega$ . This is because the ideal HWR geometry is not very efficient; a more complex inner and outer conductor geometry provides this increase in efficiency. The steps taken to achieve this improvement will be detailed in Chapter 3.

### 2.4.5 An Aside: The Three-Quarter Wave Resonator

An extension of the logic used to get the parameters for the HWR can be used for a more novel type of cavity geometry. It has been proposed [10] to operate a QWR-like geometry (open and short boundary conditions) in the  $p = 2$  mode, giving  $L = 3\lambda/4$ . The particles would be accelerated through the electric field maximum that is closer to the short plate,



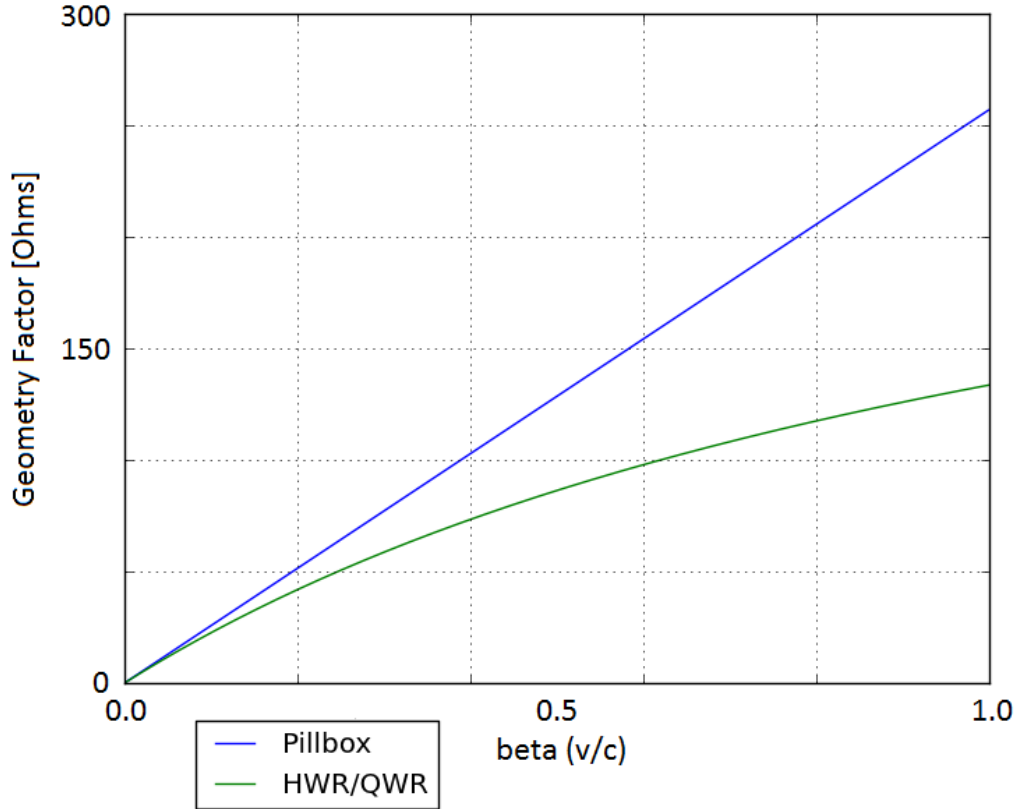


Figure 2.13: Geometry Factor plotted versus  $\beta$  for the ideal cavity geometries.

away from the open boundary. This would combine the benefits of the QWR geometry (open end for processing and inspection after fabrication) while avoiding the steering fields present in a traditional QWR. This cavity type is called a Three-Quarter Wave Resonator, or 3QWR. Comparing a HWR and 3QWR at the same frequency and beta, it is clear that the 3QWR will have the same  $G$  while the  $R/Q$  will be  $1/3$  lower.

#### 2.4.6 Another Aside: Power Transmission Choices Based on Frequency

The frequency scalings we've derived for the cylindrical and coaxial waveguides give some idea for the type of transmission line that would be required to transmit energy to these

cavities. For the cylindrical waveguide, we derived a cut-off frequency of

$$\omega_{\text{cutoff}} = \frac{2.405c}{R} \quad (2.126)$$

where  $R$  is the radius of the pipe. For the FRIB cavities, operating at 80.5 and 322 MHz, this would require a pipe radius of 1.43 and 0.36 m, far too large to be practical. For the coaxial waveguide, there is no cutoff frequency, making this geometry the desired transmission line for this application.

## 2.5 Superconducting Material Properties

Oxygen-Free, High Conductivity (OFHC) copper and niobium have been the materials of choice for the vast majority of accelerators because of the efficiency offered. Copper is an excellent conductor of both electricity and heat, allowing for low losses and easy evacuation of the joule heat generated. Niobium is a poor conductor at room temperature, but becomes superconducting below 9.2 K. The operational implications of using these materials as well as the theory behind their losses will be discussed below.

### 2.5.1 Superconducting Material Theory

As has been shown, the skin depth  $\delta$  and the surface resistance  $R_s$  for a normal conducting material are

$$\delta = \frac{1}{\sqrt{\pi f \mu_0 \sigma}} \quad (2.127)$$

$$R_s = \frac{1}{\sigma \delta}. \quad (2.128)$$

Superconducting materials behave very differently from normal conducting materials, and require a very different treatment to derive equivalent quantities. A superconducting material is typified by a sudden transition between standard normal conducting physics to a DC resistivity of zero at a certain temperature (below 9.2  $K$  for bulk niobium). Below this critical temperature ( $T_c$ ), it becomes energetically favorable for electrons to be combined into “Cooper pairs” which act as a superfluid, allowing current to flow through the material with no losses [11]. The current theory of this behavior is BCS theory [12, 13], and its predictions agree well with measured results [14, 15]:

$$R_{BCS} = 2 \times 10^{-4} \frac{C_{RRR}}{T} \left( \frac{f}{1.5} \right)^2 e^{\left( -\frac{17.67}{T} \right)} \quad (2.129)$$

as a good fit for the BCS component of the surface resistance of niobium where  $R_{BCS}$  is in ohms,  $T$  is the temperature in Kelvin, and  $f$  is the frequency in GHz.  $C_{RRR}$  is a factor based on the material purity, 1 for reactor grade niobium, and approximately 1.5 for  $RRR = 300$  niobium. From this, it is easy to see that it is desirable to operate superconducting cavities at the lowest temperature possible. In practice,  $R_{BCS}$  isn't the only contribution to the surface resistance. The remaining resistance is a material/cavity processing dependent resistance called the “residual resistance”  $R_{res}$  that does not depend on temperature or frequency. While residual resistances of below 1  $n\Omega$  have been achieved, 10  $n\Omega$  is more reliably reproducible for large scale cavity fabrication [16]. If the cavity is operated at or below 2 K, the residual losses tend to dominate performance. An approach for estimating the skin depth of a superconducting material can be derived [7, pp. 85-88] by using a two-fluid model for the electrons in the material, one fluid composed of the Cooper pairs, and the other the unbound electrons. This gives a penetration depth (called the London Length [17])

of

$$\lambda_L^2 = \frac{m}{n_s e^2 \mu_0} \quad (2.130)$$

where  $m$  and  $e$  are the mass and charge of the electron, and  $n_s$  is the density of the superconducting electron pairs. For niobium, this penetration depth is on the order of tens of nanometers, meaning that the RF performance is dominated by the quality of a very thin layer on the surface of the material. The temperature dependence for  $\lambda_L$  has been empirically found as [18]

$$\lambda_L(T) \approx \lambda_L(0) \left[ 1 - \left( \frac{T}{T_c} \right)^4 \right]^{-1/2}. \quad (2.131)$$

While it becomes energetically favorable for electrons to form Cooper pairs below  $T_c$ , this is offset by the application of a magnetic field. Magnetic flux is expelled in the transition from normal to superconducting (called the Meissner Effect [19]), but the fields still penetrate the material on the order of the London Length. BCS theory approximates the temperature dependence of this critical magnetic field as

$$H_c(T) = H_c(0) \left[ 1 - \left( \frac{T}{T_c} \right)^2 \right]. \quad (2.132)$$

Finally, niobium is a Type-2 superconductor. This means that the transition from superconducting to normal conducting in the presence of a magnetic field actually has two critical magnetic field levels,  $H_{c1}$  and  $H_{c2}$ , in contrast to a Type-1 superconductor in which the superconductivity breaks completely at one field level. This behavior can be seen in Figure 2.14. One of the reasons niobium is used for superconducting accelerators is the relatively high  $T_{c1}$ , one of the highest for any Type-2 superconductor.

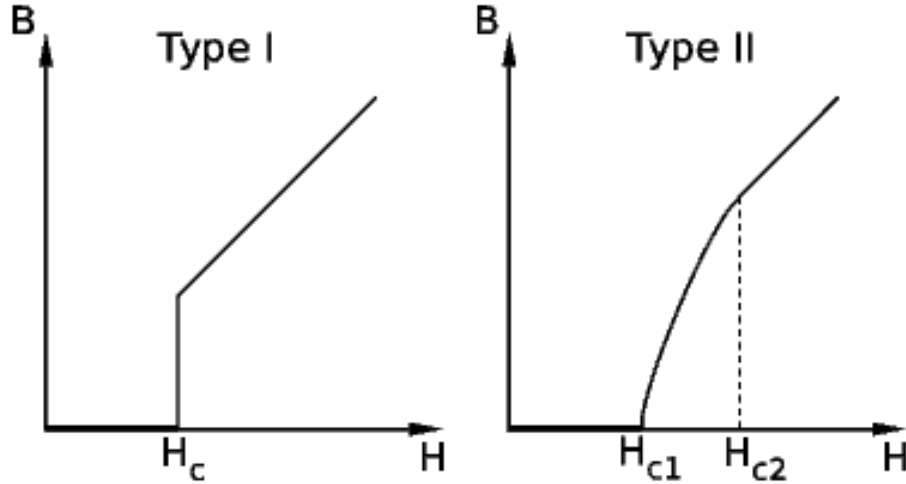


Figure 2.14: Magnetic field just inside superconducting material around transition for Type 1 and 2 materials. Note the sudden penetration for Type 1 and the gradual break down for Type 2.

## 2.5.2 The Advantages of Superconductivity

Assuming that it is operated at a temperature well below 9.2 K (not challenging with liquid helium's boiling point of 4.2 K at 1 bar), superconducting cavities can be operated with very low losses. The surface resistance for a well prepared bulk niobium can be as low as single nano-ohms, as compared to micro-ohms for a well prepared copper cavity. This means that for the same cavity and field level, the losses are lowered by 6 (!) orders of magnitude. Some of this is lost because of the requirement to operate at very low temperature. The maximum achievable efficiency for heat transfer depends on the input and output temperature and is given by the Carnot Efficiency:

$$\eta_c = \frac{T_C}{T_H - T_C} \quad (2.133)$$

where  $T_H$  and  $T_C$  are the temperature at which the heat is exhausted and extracted in Kelvin. For 4 K operation, this gives an *optimum* operation efficiency of .013. This should be combined with the technical efficiency of cryogenics systems ( $\nu \approx 0.2$  [7, p. 48]), resulting

in an increase in required wall power by two to three orders of magnitude. This means that the six orders of magnitude decrease in material losses is, in practical terms, three orders of magnitude gain in wall power efficiency. For applications which call for the cavities to be operated in continuous wave (CW) mode, the cost savings of superconducting operation can be substantial, despite the complex technology involved.

### **2.5.3 The Challenges of Superconducting Materials**

While the decrease in required power is substantial, there are drawbacks to using superconducting cavities. The cryogenic engineering talent and facilities required is a dramatic investment, and can be a significant portion of the overall cost of an accelerator. Additionally, the ultimate performance and achievable accelerating gradient is limited by the peak surface magnetic field. Even for an extremely well prepared cavity, the peak surface magnetic field is  $\sim 220$  mT, and for low velocity cavities, even with state of the art processing, this number is closer to 120 mT. Because the losses in a superconductor also increase strongly with frequency, this means that superconducting cavities are limited to operation under 2 GHz for practical reasons. Even the International Linear Collider which is designed to operate at 1.3 GHz and 2 K has moved to a pulsed design to limit the load on the cryogenic systems. Additionally, there are many processing and fabrication considerations for these cavities to achieve a low surface resistance with little to no radiation. These considerations will be discussed later in this document.

### 2.5.4 Practical Concerns: RRR and Impurities

Procurement of the appropriate material for an accelerating cavity is an important step in obtaining good performance. While the RF losses in a cavity are small, the specific heat of niobium at those temperatures is also quite low. If the thermal conductivity is small, local heating can occur at high fields, breaking the superconductivity in what is known as a thermal quench. The thermal conductivity of the niobium is dominated by impurities and crystal structure, which is measured by the RRR:

$$RRR = \frac{\sigma(4.2K)}{\sigma(300K)} \propto \kappa \quad (2.134)$$

where  $\sigma$  is the electrical conductivity and  $\kappa$  is the thermal conductivity. Material can be readily obtained from suppliers with RRR of over 250, considered good enough to give good cavity performance. This material is produced by repeated electron beam melting in vacuum to drive off impurities, and can also be improved by baking over 1200°C in vacuum with either titanium or Yttrium as a getter to remove impurities.

## 2.6 Coupler Theory and Design

Cavities are ultimately powered by a power plant, like all other devices that require electricity. This wall power is used to power both the low power RF signal generators and the amplifiers (klystrons, solid state, or other types) that generate the large amounts of power needed to fill the cavity. This power must be effectively transformed from traveling wave power in the transmission lines to the standing wave mode of the cavity. In this section, the basic design and some considerations of these couplers will be discussed in the context of different

applications. These topics will be expanded upon with more specific design and theory for couplers used for low beta superconducting resonators like those being designed for the FRIB driver linac.

### 2.6.1 Coupler Figures of Merit

Types of transmission lines have already been discussed, and coaxial waveguide has been demonstrated to be the only practical solution at low frequency. From this, we can design two types of couplers, probe (capacitive) and loop (inductive). Probe couplers use the transmission line's inner conductor to excite the cavity electric fields in the local region. There are different ways to quantify the coupling strength, but the overlap between the excited fields from the inner conductor of the coupler and the fields in the cavity drive the coupling strength. Thus, the probe type coupler is more effectively used in the high electric field region of the cavity. The desired coupling strength is then achieved by changing the length of the coupler inner conductor. Magnetic field coupling is achieved by attaching the coupler inner conductor to its outer conductor, making a loop. Magnetic fields are excited normal to the loop, and the strength of the coupler is determined by the confluence of these excited fields and the cavity mode's magnetic field distribution. The desired coupling strength is achieved by varying the area of the loop exposed to the cavity (moving the coupler in or out of the cavity) or changing the angle between the cavity field and the normal of the loop (rotating the coupler). The coupler strength can be quantified by the rate at which energy enters or leaves the cavity through the coupler. This emitted power,  $P_e$ , can be normalized to the stored energy in the cavity and used to form an effective quality factor for



the coupler called the “external Q”:

$$Q_{ext} = \frac{\omega U}{P_e}. \quad (2.135)$$

The ratio of the external Q to the cavity Q is called the coupling factor,  $\beta$  (not to be confused with the relativistic  $\beta = v/c$ )

$$\beta = \frac{Q_0}{Q_{ext}} = \frac{P_e}{P_d}. \quad (2.136)$$

In reality, what will be measured if a cavity is connected to a Vector Network Analyzer (VNA) will be a quality factor given by the *total* losses in the cavity. The total losses in the cavity are given by

$$P_T = P_d + P_e + P_t \quad (2.137)$$

where  $P_e$  is the power emitted from the input coupler (port 1),  $P_t$  is the power emitted from the transmitted power coupler (port 2), and  $P_d$  is the power dissipated in the cavity itself. This gives us a “loaded” quality factor of

$$\frac{1}{Q_L} = \frac{1}{Q_0} + \frac{1}{Q_{ext,1}} + \frac{1}{Q_{ext,2}} \quad (2.138)$$

which gives

$$Q_0 = Q_L(1 + \beta_1 + \beta_2). \quad (2.139)$$

It is desired to measure  $Q_0$  directly, but in steady state, only the scattering parameters ( $S_{11}$  and  $S_{21}$ ) can be measured. The scattering parameters are defined as

$$|S_{11}|^2 = \frac{P_r}{P_f} \quad (2.140)$$

$$|S_{21}|^2 = \frac{P_t}{P_f} \quad (2.141)$$

with  $P_f$  being the forward power and  $P_r$  being the *total* reverse power from the cavity, the vector sum of the reflected and emitted traveling waves.  $\beta_1$  and  $\beta_2$  can be expressed in terms of these scattering parameters [7, p. 48]

$$\beta_2 = \frac{|S_{21}|^2}{1 - |S_{11}|^2 - |S_{21}|^2} \quad (2.142)$$

$$\beta_1 = \frac{1 - |S_{11}|}{1 + |S_{11}|} \quad (2.143)$$

or

$$\beta_1 = \frac{1 + |S_{11}|}{1 - |S_{11}|} \quad (2.144)$$

depending on coupling strength. For  $\beta_1 < 1$  (Equation 2.143), the coupling is considered “undercoupled,” for  $\beta_1 > 1$  (Equation 2.144), the coupling is considered “overcoupled.” The remaining case,  $\beta = 1$ , is the “matched” condition. In this configuration, there is no reverse power because the emitted and reflected power from port 1 are equal in magnitude and opposite in phase. These equations are derived assuming the measurement is being done in a steady-state and that  $\beta_1 \gg \beta_2$  so that  $P_t$  can be dropped while considering the behavior of Port 1. It can be seen from these equations that some additional knowledge is required for accurate interpretation of the measured values, any measurement of  $|S_{11}|$  can result in two different  $\beta_1$  results. This information can be found by changing the parameters of the measurement. Observing the change in  $|S_{11}|$  because of adjusting the coupling is a known way to determine if the cavity is over or under coupled. For example, increasing the length of a probe coupler should increase the coupling strength  $\beta$ . If  $|S_{11}|$  increases

because of this change, the coupler is now overcoupled. If  $|S_{11}|$  drops, the coupler started as undercoupled. This type of change must be done with care to avoid confusion from crossing  $\beta = 1$ . Additionally, the  $P_f$  can be modulated, and the behavior of  $P_r$  and  $P_t$  can be used to determine the coupling. This method is only realistic when the time constant of the cavity

$$\tau = \frac{Q_L}{\omega} \quad (2.145)$$

is large enough to be measured easily. Because  $Q_L$  is so small when the cavity is normal conducting ( $\sim 1000$ ), it is only possible to measure the coupling by modulation of the forward power when the cavity is superconducting, with  $Q_L \approx 1 \times 10^7$  or higher. A more detailed description of this process can be found in Chapter 4. For a realistic cavity, two couplers are used. The “input” coupler is a high power coupler designed to be either close to matched or overcoupled depending on the situation. The second coupler, called the “pickup” coupler, is used as a field probe, allowing simple measurement of the cavity stored energy. This coupler is significantly undercoupled so that the power radiating out of this coupler ( $P_t$ ) is very low, so it can be treated as a perturbation, greatly simplifying the mathematical analysis of the measured results. A useful rule of thumb when choosing the pickup coupling is to ensure that  $P_t$  is always below 1 mW, even at the extreme limit of cavity performance.

## 2.6.2 Bandwidth Considerations

The bandwidth of the cavity is determined by the total energy loss in operation, giving the equation

$$\Delta f_{BW} = \frac{f_0}{Q_L}. \quad (2.146)$$

Because  $Q_0$  is so large for superconducting cavities, this means that the cavity bandwidth is often dominated by the choice of  $Q_{ext,1}$ . When testing a cavity in controlled environment, the cavity frequency can be allowed to drift as needed. This means that the bandwidth of the cavity can be kept quite small, often as close to matched as possible, because the RF circuitry is flexible enough in the configuration to not require a large bandwidth. This keeps the power requirements as small (and inexpensive) as possible, simplifying the testing hardware required. For operation in a real machine, the cavity frequency must be tightly controlled for stable operation. This means that the RF control systems must react to the changing cavity conditions while keeping the amplitude, phase, and frequency of the cavity within tight, preset parameters. This is a much more difficult task, and the cavity bandwidth must be large enough to allow this stable operation of the cavity. This means heavily overcoupling the cavity, meaning that  $P_e$  dominates cavity losses and  $P_r \approx P_f$ . How overcoupled the cavity must be is determined by size and time scale of the frequency perturbations the cavity is likely to experience as well as the control systems used.

### 2.6.3 High Power Concerns

When the cavity is heavily overcoupled,  $P_f$  is much larger than  $P_d$ . This means that the input couplers must be able to handle full power in the forward and reverse direction simultaneously, and this leads to stringent cleaning standards for couplers, much like the cavities. Couplers are often cleaned and conditioned much like normal conducting cavities are, and their cooling can be a serious issue. Couplers designed for such high power and so heavily overcoupled will often be a significant perturbation to the cavity fields, and their effect on cavity frequency and performance must be taken into account during standard

cavity design. Additionally, the coupling is chosen based on an assumption of  $Q_0$ , but in reality, this can vary from cavity to cavity. The ability to vary the input coupling in situ adds mechanical complexity to coupler design, but allows fine tuning of each cavity to either minimize power requirements on an overperforming cavity or allow operation of a poorly performing cavity. This benefit extends to Dewar testing, where  $Q_0$  is varying more widely than in real operation. A variable coupler allows for testing or conditioning at a higher field by keeping the cavity close to matched for a much wider range of cavity performance.

## **2.7 Parameter Scaling and Resonator Selection Based on Application**

Choice of resonators is an important and complex decision for a given accelerator complex. For heavy ion accelerators, this optimization problem becomes quite a bit more complex, with a variety of structures required to span the velocity ranges required. In this section, I will use FRIB as a case study to describe the decision and optimization process undertaken to arrive at a design for the FRIB driver linac, highlighting certain resonator-driven decisions.

### **2.7.1 What Type of Charged Particle?**

The FRIB driver linear accelerator (linac) will be required to accelerate many different elements from oxygen to uranium. These isotopes have a wide variety of neutron to proton ratios, complicated by the fact that the ion sources for FRIB are not able to produce beams of fully ionized atoms. The final energy for these beams will be at least 200 MeV/u, depending on the isotope and charge state. This clearly calls for an extremely flexible acceleration

system, with many tunable parameters to optimize for different beams.

### **2.7.2 What Energy?**

FRIB was chosen to be built on the campus of Michigan State University near the current site of the National Superconducting Cyclotron Laboratory. Being built in an underground enclosure on campus means civil construction cost is a driving issue, leading to an accelerator design that is as compact as possible. This, combined with the desire that the accelerator operate with a duty cycle of 1, leads naturally to the choice of a superconducting accelerator because of the high efficiency and accelerating gradients that can be achieved.

### **2.7.3 How Much Beam Power?**

To achieve the desired power on target of  $> 400$  kW for Uranium, up to five charge states are to be accelerated simultaneously to get the beam current required. Additionally, a pulsed system would not be able to achieve the high power/current required. This means that neither normal conducting accelerator technology nor a rapidly cycling synchrotron would be practical for FRIB.

### **2.7.4 The Transit Time Factor**

As has been discussed, the more synchronized gaps an accelerating cavity has, the smaller the range of velocities it can accelerate efficiently. For an accelerator like FRIB, where the velocity of the beam is changing drastically over the entire accelerator, this means that two-gap structures are demanded. Coaxial resonators are also indicated for FRIB because they offer the most efficient acceleration at these low velocities. Even using QWRs and HWRs,

at least four different cavity designs are required. While using resonators with more gaps was considered, the complexity of the geometries designed for the velocities required and the larger number of different geometries demanded led to the current design using two QWRs designed for  $\beta = 0.041, 0.085$  and two HWRs designed for  $\beta = 0.29, 0.53$ .

## 2.8 Operational Experience with Low-Beta Cavities

Nuclear physics has used superconducting low velocity accelerating cavities for decades, starting with ATLAS at Argonne National Laboratory [20] in 1978. Since then, many laboratories around the world have built on this experience and commissioned superconducting accelerators for nuclear physics. The FRIB accelerator design draws on this experience to both avoid common problems and provide superior performance. This section will provide a brief summary of this knowledge base and the new technologies that are being driven by the demands of FRIB.

### 2.8.1 Quarter Wave Resonators

There are many facilities around the world that use superconducting QWRs for nuclear physics. Major examples of this are ATLAS at Argonne National Laboratory [21], PIAVE-ALPI at Istituto Nazionale di Fisica Nucleare (INFN) Legnaro in Italy [22], and ISAC-II at TRIUMF in Vancouver, Canada [23]. In addition to these, there are several accelerators currently being designed and built such as SPIRAL-2 at GANIL in France [24] and R $\epsilon$ A3 at Michigan State University [25]. The latter provides a natural test-bed for FRIB technology. The experience gained while designing, fabricating, commissioning, and operating all of these accelerators will be invaluable for FRIB, which will use two different QWR designs for the

first section of acceleration. However, while these facilities use their QWRs to accelerate their beams to only a few percent of the speed of light, FRIB requires final velocities over 60% the speed of light. As has been discussed, QWRs become unusable at high velocity because of beam steering, and a different geometry is required.

### **2.8.2 Half Wave Resonators**

For FRIB, it was decided to use two different HWR geometries for the high-energy section of the accelerator. The accelerator is designed to provide flexible, efficient accelerating to  $> 60\%$  the speed of light (remember previously discussed cavity scaling) for the wide variety of isotopes required. While the ideal HWR geometry is similar to the ideal QWR, the process of optimization and design for operation in a realistic accelerator is quite different. Much of the experience gained on QWRs can be extrapolated to HWRs, but there is little practical experience fabricating and operating HWRs in an accelerator. There is only one facility in the world that has accelerated beams with HWRs, the Soreq Applied Research Accelerator Facility (SARAF) in Israel [26]. These HWRs were designed to accelerate hydrogen and deuterium at 9% the speed of light, and have presented a multitude of challenges during commissioning [27]. Given this experience, FRIB will require the most advanced HWRs ever designed and built, and the remainder of this document will be devoted to the design, fabrication, and testing of these types of cavities.



# Chapter 3

## Electromagnetic and Mechanical Design of a Half Wave Resonator

In this chapter, we start with an explanation of the software tools used to evaluate electromagnetic and mechanical performance, followed by a more detailed discussion of the optimization techniques used to arrive at state-of-the-art HWRs such as might be used for the FRIB cavities. This will include both electromagnetic and mechanical concerns as well as more practical issues arising from industrial fabrication demands.

### 3.1 Electromagnetic Cavity Simulation

The ideal HWR geometry is an instructive tool for estimating cavity performance because it is analytically solvable. This geometry is, however, not practical for use in a real accelerator. There are many features that must be added and optimized that cannot be treated analytically, and must be simulated. Modern electromagnetic simulation software can simulate the parameters of almost any geometry and evaluate its figures of merit, often only limited

by the amount of computing power available. In this section, the basic methods that these solvers use to simulate these complex geometries will be discussed. In addition, more practical considerations and methods used to perform the design simulations will be presented for use in the rest of this document.

### 3.1.1 Finite Element Solvers

In order to solve a complex geometry like that of a realistic cavity, the volume of the cavity is broken into a discrete set of interlocking simple geometries, called elements. Tetrahedral elements are the most commonly used for cavity design because they often give the most accurate representation of the complex surfaces involved in cavity design. An example of this can be seen in Figure 3.1, generated in ANSYS-APDL. The fields in the cavity are then

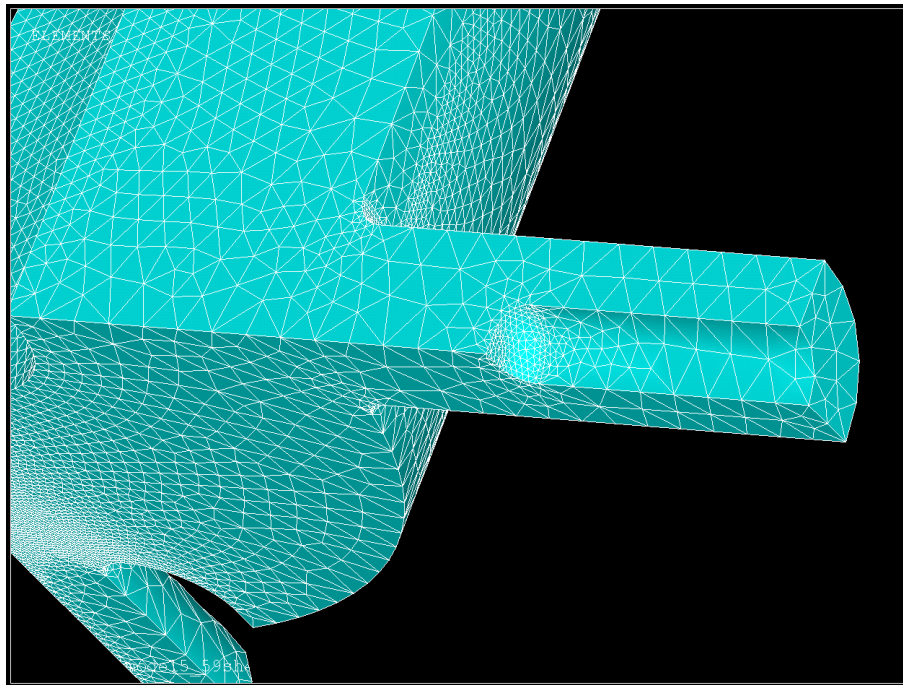


Figure 3.1: A cavity vacuum space meshed with tetrahedral elements, a coupler probe is in the foreground with a beam port cup visible in the background.

assumed to have a simple representation in the volume of the element, expressed as a low-

order (often 1st or 2nd) function of space. An example of the structure of these elements can be seen in Figure 3.2. Because the fields in the cavity are assumed to be monochromatic,

## Representation of field with linear elements in 3d

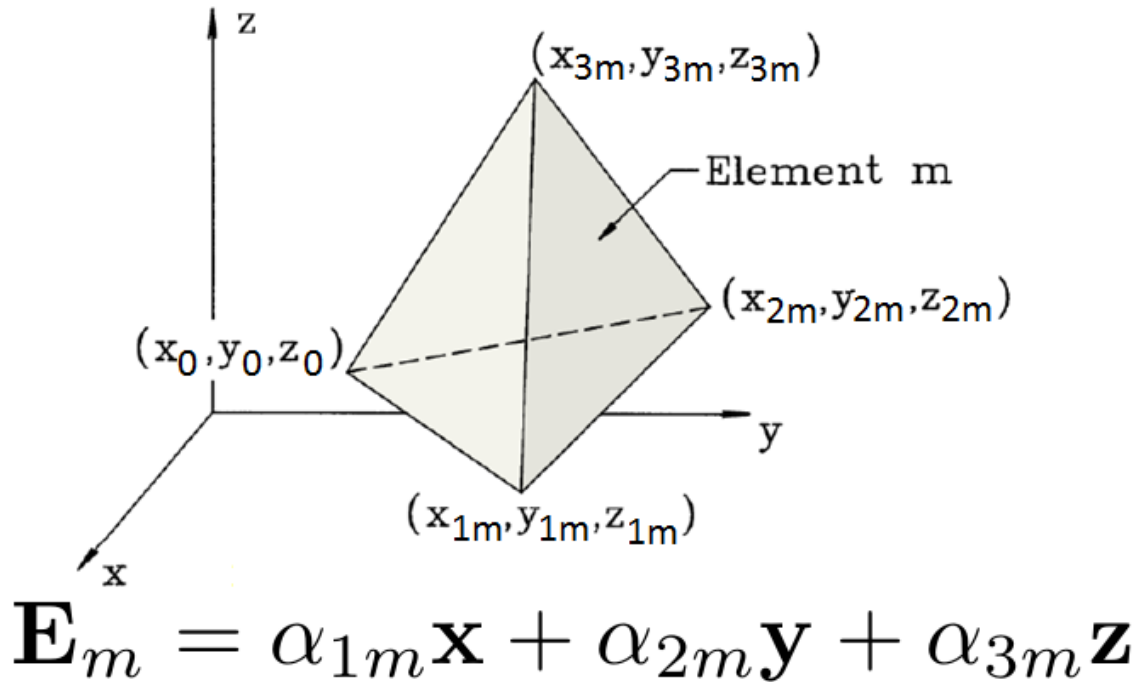


Figure 3.2: Structure of a first order (linear) tetrahedral element. Image credit to F. Krawczyk.

the electric fields in the cavity can be described by the Helmholtz Equation:

$$(\nabla^2 + k^2)\vec{E} = 0. \quad (3.1)$$

This equation is then discretized and applied to each element. Elements “interact” at fixed places, generally along the outside edges, called nodes. The parameters of each element are iterated with the goal of minimizing the global stored energy. The study and development

of these solvers is an active and growing field, but for the basic methods and mathematical foundations of these solvers, “Electro-magnetics and Calculations of Fields” by Ida and Bastos [29] or “Finite-element Methods for Electromagnetics” by Humphries [30] are recommended as starting places. What this procedure allows is the accurate representation of the fields in a complex geometry with evaluation of the electromagnetic figures of merit.

### **3.1.2 Geometry Creation**

The first step of any simulation is defining the problem. Because the geometries involved are very complex, it was chosen to use a Computer-Aided Design (CAD) program, SolidWorks [31], to create the needed geometry. This is because the native geometry creation in the electromagnetic solver used for this project (and most other solvers) works by the creation and Boolean combination of primitive objects (cone, spheres, rectangular boxes) or swept two dimensional shapes. The details of the specific geometric features created and their effects on the cavity will be discussed in more detail later in this chapter. After the geometry is completed, it must be exported in a form that can be read by the simulation software. The format of choice for this was SAT, for ease of both export and import. Depending on the complexity of the geometry, it may be necessary to use different SAT [32] file settings or versions (as of publication, there were 18 versions) for the simulation software to properly interpret the geometry.

### **3.1.3 Simulation Procedure**

Assuming that the geometry has been successfully created and imported into simulation software, the basic electromagnetic simulation occurs in four major stages: Setup, Meshing,

Solving, and Post Processing. Each of these stages carries its own importance and subtleties, but in the following subsections, the work flow for each stage in the context of the simulation software used for the work presented later will be outlined. The simulation software used for the vast majority of the work presented is ANSYS-APDL [33]. Complete scripts detailing the execution of the described procedures can be found in the Appendices. It should be noted that, while the general process can be applied, the details of repeating this work in different simulation software (CST-Microwave Studio [34], ANALYST [35], HFSS [36], ACE3P [37]) will very likely be quite different, i.e., *Caveat Lector*.

### **3.1.4 An Aside - Computer Resource Management**

Computer resource management is an important setup for large scale simulations. This includes storing solutions files on the fastest available disk drive available. Using solid state drives in place of traditional palette drives can decrease simulation time by 30 - 40%, depending on the type of solution being done, assuming a large enough solid state drive can be acquired. Eigenmode simulations tend to be memory limited, as opposed to processor speed limited, meaning that investments in upgrading available memory speed and size can speed simulations considerably. Additionally, the temporary files generated during simulation and results files can be extremely large. If the disk drive you are using is 32-bit formatted, it will be unable to store these files. Some simulation software have a feature that ensures no files are larger than the 4 Gigabyte limit for FAT32 formatted drives. A 32-bit architecture also limits the amount of memory that can be allocated to a single program to 2 Gigabytes as well, so moving to 64-bit architecture removes both of these limitations. Depending on the software in use, multiple processor cores can be used in parallel to increase solving speed.

When starting a simulation, ensure that the maximum number of processors, largest amount of memory, and fastest hard drive space available are allocated for the job.

### 3.1.5 Simulation - Setup

Given that the skin depth for high conductivity materials (and especially superconducting materials) is so small, the fields *in* the conductor and the losses generated can be treated as a perturbation. That leads to two standard types of boundary conditions, Perfect Electric Conductors (PEC), and Perfect Magnetic Conductors (PMC). The PEC boundary condition indicates that  $E_{\parallel} = 0$ , and  $H_{\perp} = 0$ , and is appropriate for conductor surfaces and some boundary conditions depending on the mode structure you are trying to simulate. The PMC boundary condition indicates that  $E_{\perp} = 0$  and  $H_{\parallel} = 0$ , and is used for a majority of symmetry planes. All exterior surfaces of the model must be defined as one of these. Starting from a basic imported vacuum space, it is very useful to define groups of important surfaces for later reference. These groups can include symmetry planes, conducting planes of the same conductivity, or areas to be used for special types of analysis. For the HWR model seen in Figure 3.3, generated in SolidWorks, there are two groups of critical surfaces, the symmetry planes seen in blue and the cavity RF surface in gray. The symmetry planes are defined as PMC, and the RF surfaces are defined as PEC. Additionally, any surface can be assigned a conductivity. This will be used to perturbatively calculate losses based on the magnetic fields on that surface. While the cavity RF surfaces are generally assigned the same conductivity, surfaces of interest can be assigned different conductivities based on their material type. This can be very useful for specialized investigations, which will be discussed later in this chapter. Numerical constants can also be set for convenient use later. Grouping

their declarations early in a script eases later modifications. The type of element must be defined as a high-frequency eigenmode type element, and the order of this element must be set. Material properties are also set here, but for a simple high-frequency eigenmode solution,  $\epsilon = \epsilon_0$  and  $\mu = \mu_0$  are the only required definitions.

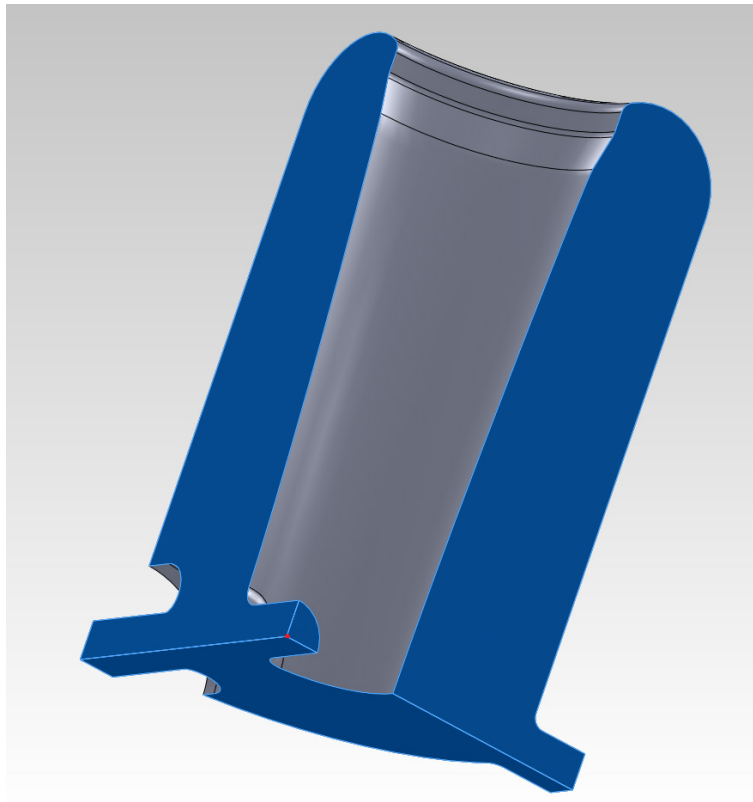


Figure 3.3: HWR vacuum model. Symmetry planes can be seen in blue, Perfect Electric Boundaries can be seen in gray, the cavity origin is marked in red.

### 3.1.6 Simulation - Meshing

Finite element simulations require the cavity volume to be represented by a collection of smaller volumes called elements. The process of defining the size and shape of these elements is called meshing. These elements should be, at largest, one tenth the wavelength you expect to simulate to improve accuracy [29]. The accuracy of the remaining figures of merit are

strongly influenced by the quality of the mesh. Curved surfaces are especially sensitive to meshing as the elements on the surface must be small enough to accurately represent the curvature. A rule of thumb for small curved features is the element size should be smaller than one third the radius of curvature. An example of inadequate meshing can be seen in Figure 3.4.

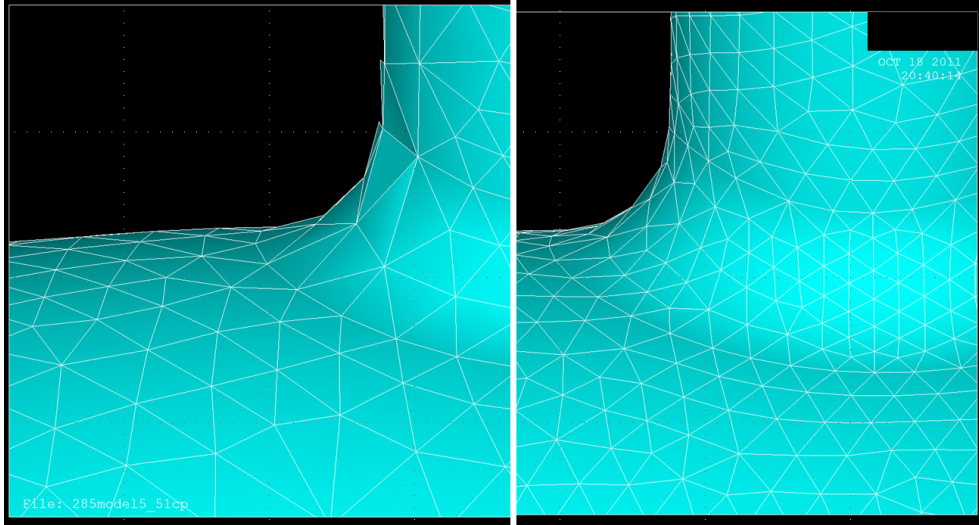


Figure 3.4: Comparison of different meshing on a curved surface. Left: Poor meshing on a curved surface. Right: Same surface with improved mesh density. Images generated using ANSYS.

While most software has advanced automatic meshing algorithms, additional manual refinement may be required based on the geometry being simulated. The first, most common, mesh optimization step is the setting of a maximum element edge length. This can be done for both whole volumes and on areas of known high surface fields. For the volume sizing, it is important to set a global maximum value for an element edge length to prevent drastic gradients in element size. The standard rule of thumb for electromagnetic simulation calls for a maximum element edge length of  $\lambda/10 \approx 9$  cm for 322 MHz. For complex geometries like the ones used for HWRs, additional surface refinement may be required to accurately calculate surface losses and peak surface fields. For accurate surface fields on the small



curved surfaces, elements as small as 1 mm were found to be needed in some locations of the cavity. If the transition between these element sizes is not carefully controlled, poor mesh quality can result. Setting a global maximum on the element size is a powerful tool for regulating this transition. A major factor in mesh quality tolerance is the order of element chosen (i.e., what *order* function is used to represent the fields in an element). As can be seen in Figure 3.5, increasing the mesh density reduces frequency error down to a baseline inaccuracy that is solver dependent. For ANSYS-APDL, this error was found to be roughly 1 part in  $10^5$ , or  $\sim \pm 50$  kHz out of 322 MHz. This level of accuracy was achieved with second order elements at a much lower density than for first order elements. While the solve times for the same accuracy is roughly equivalent, the use of second order elements greatly reduces the meshing tolerances while giving similar or improved surface field accuracy. There are sometimes limitations from the meshing that can help drive the decision to strive for first or second order meshing. Some geometries are so complex that their mesh densities must be high for geometric fidelity. Depending on the available computing hardware, this type of geometry can often require far more mesh elements than could be solved with second order elements, but can be solved with first order elements at a loss of accuracy. In this situation, all results, especially surface fields, must be interpreted with this in mind. When the computing hardware allows, this type of complex geometry should be solved using second order elements if possible, especially if surface fields are of particular interest. Meshing must also be approached carefully with geometries that are very simple. Meshing software will often generate very large elements in these geometries if allowed, and care must be taken to ensure they do not grow large enough to sacrifice accuracy. This is an ideal situation to use a global element edge length limit.

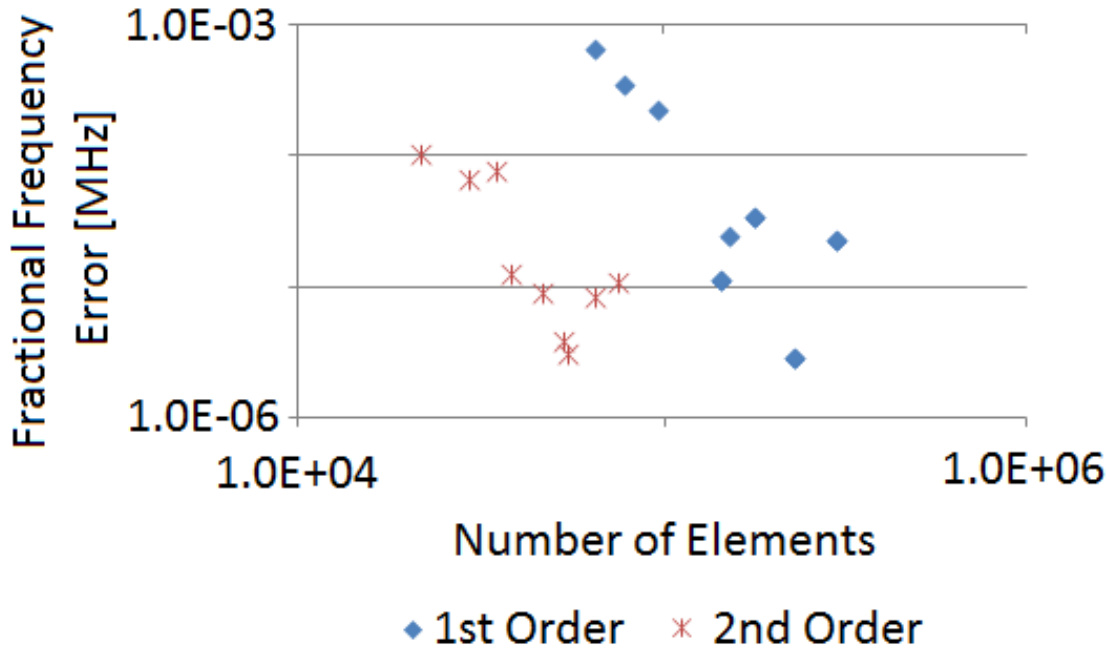


Figure 3.5: Fractional frequency error for different mesh densities in identical geometries for first and second order elements.

Additional care must be taken when generating geometry to avoid causing meshing problems. While this is a more serious issue for mechanical simulations, and will be discussed in greater detail in the relevant section, there are certain features that should be avoided if possible, and these are places of optimization to generally reduce the size of simulations without great sacrifice for accuracy. CAD geometries are represented in simulation software as a continuous and closed collection of surface, each bounded by lines. Mesh structure must respect the shape and boundary of these surfaces, and care should be taken to not create very small areas unnecessarily, or otherwise collect many boundaries together without purpose. An example of a mesh that is overly dense at surface intersections can be seen in Figure 3.6. This type of feature can be tolerated if the solution time isn't excessive, but when working on a very large simulation, it may be beneficial to find instances like this and correct the geometry to allow for more optimal meshing.

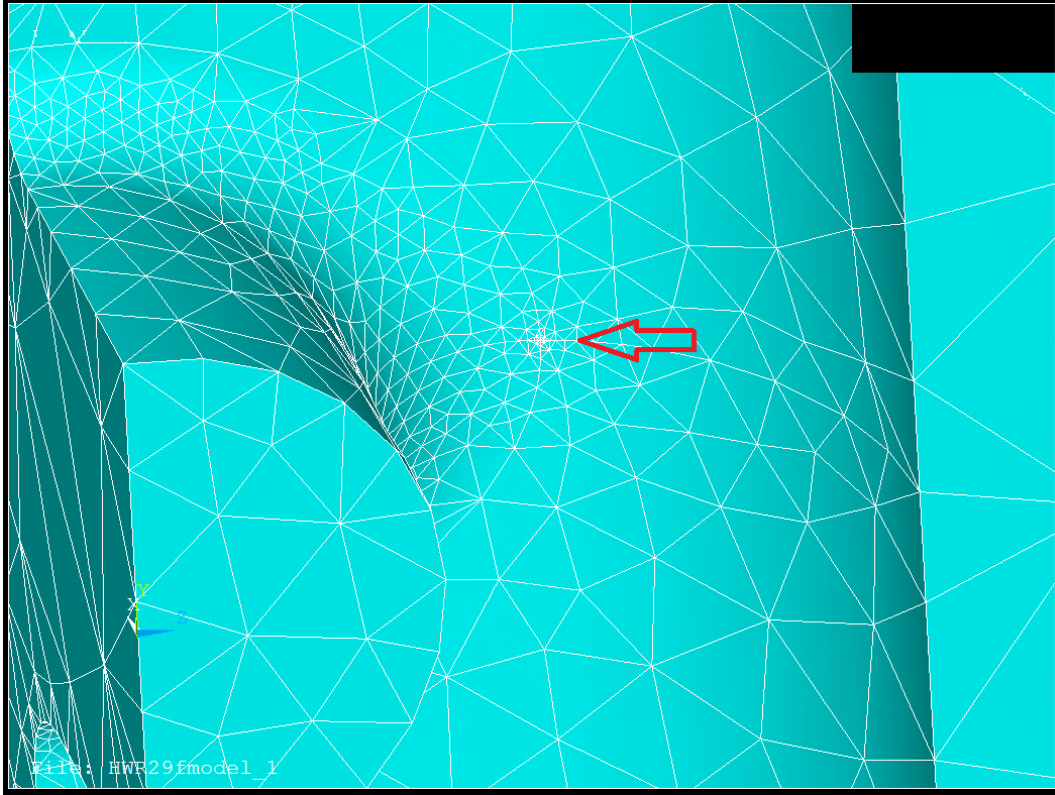


Figure 3.6: The intersection of four surfaces can force excess mesh density, indicated by the red arrow. Images generated using ANSYS.

Automatic meshing algorithms often make meshing decisions based strictly on the geometry, not on the structure of the mode being simulated. This is understandable because the information is not available to the program before the simulation is complete. Some programs like ANALYST have automatic iteration algorithms that use solution data to adjust and optimize the meshing until the solution has converged to the accuracy desired. For most simulations software, foresight can dramatically improve the quality of the simulation results. We've touched on this for surface fields and especially external surfaces with a large curvature, but this is also quite important for the accelerating field profile. Large elements on the beam axis result in a non-physical accelerating field because the fields cannot be properly interpolated between elements to give a smooth shape. Improving the density of

the meshing around the beam axis gives a more accurate accelerating field profile. Both of these behaviors can be seen in Figure 3.7.

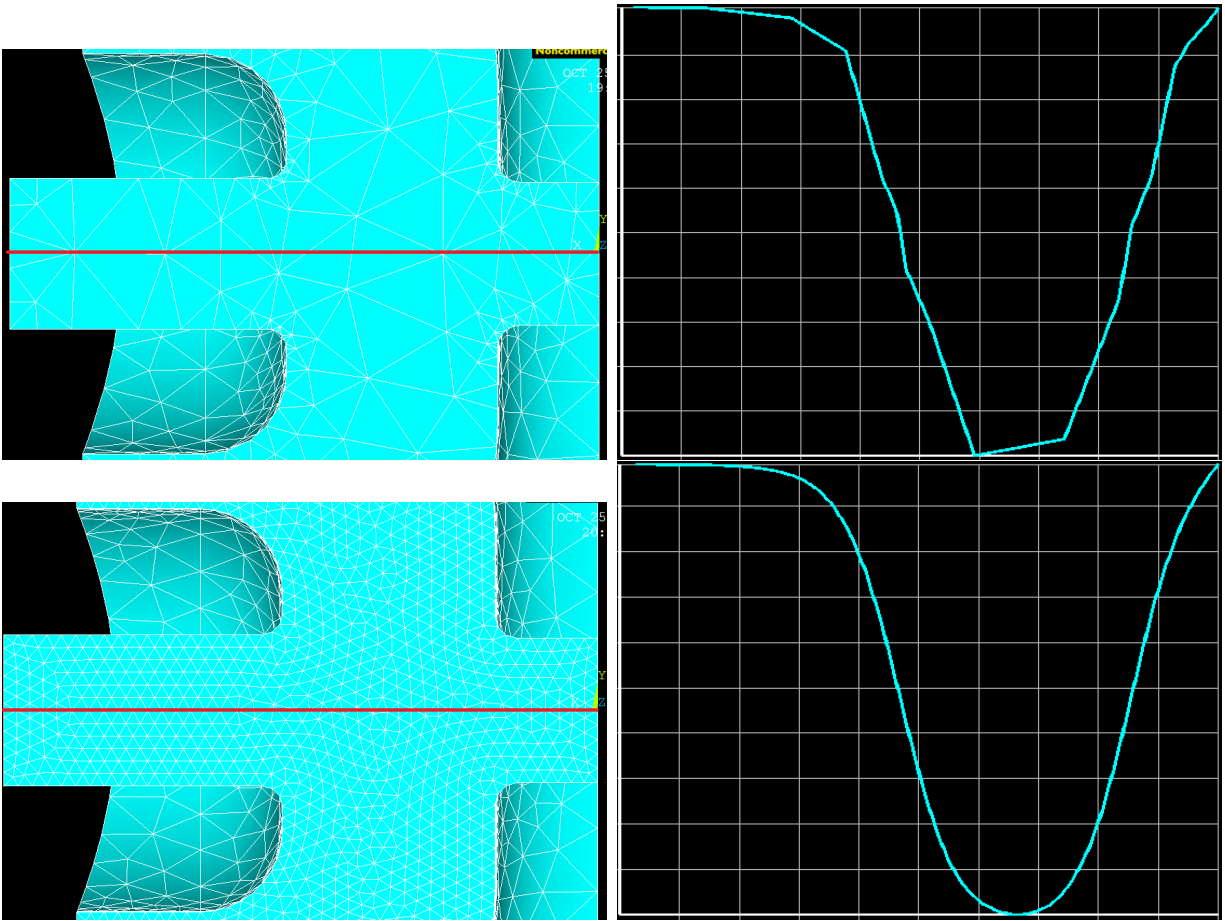


Figure 3.7: Top Left: Poorly meshed cavity, beam axis marked in red. Top Right: Resulting accelerating electric field. Note the non-physical roughness that results from the large element size. Bottom Left: Cavity with improved meshing on beam axis which is marked in red. Bottom Right: Resulting accelerating electric field. Note the improved field profile that results. Images generated in ANSYS.

### 3.1.7 Simulation - Solving

Once the cavity has been meshed and appropriate boundary conditions (PEC, PMC, conductivities, etc.) have been specified, most solvers require some options set to calculate an eigenmode. For ANSYS-APDL, the solver needs to be set to modal, and a frequency range

given for the mode(s) desired. The solver will search for eigenvalues (resonant frequencies) for the cavity element matrix from the low end to the high end of the range until the requested number of modes are found. For most purposes, this range should only be as large as needed to encompass all the variation in the single frequency anticipated. Searching for a range that is  $\sim \pm 10\%$  of the desired resonant frequency is often large enough to still find the resonance even after relatively large geometry changes. For complex structures, this range may also include unintended trapped modes in small features like couplers or tuners, so it is often advisable to scan a larger frequency range for modes before focusing exclusively on the mode of interest. After launching the solution process, the solver will often list the amount of memory needed for the solution. “In core” solutions are done with the entire simulation resident in memory. This greatly speeds simulation time and is the desired mode of operation. “Out of core” solutions require the solver to transfer data between memory and the hard disk, a much slower process. This is one of the prime reasons simulation programs should be allowed access to as much memory as possible.

### **3.1.8 Simulation - Post Processing**

The first step after a new simulation finishes is verifying that the solve has completed properly. While there are various intuitive methods for this, the most effective is often plotting the fields in the cavity. For most geometries, the mode structure is known, at least in concept. Qualitative comparison of the solved fields with this general form (comparing a HWR simulations to the general structure of the ideal HWR mode, for instance) can give a good indication of the quality of the solve. This will also identify surfaces requiring additional mesh refinement, an example of which can be seen in Figure 3.8. In this example, the coarse

meshing resulted in a non-physical roughness to the surface fields, with one element having artificially high fields. Improved meshing removes a great deal of this roughness, and gives a more accurate peak surface field. Once the solution has been evaluated and found to be suf-

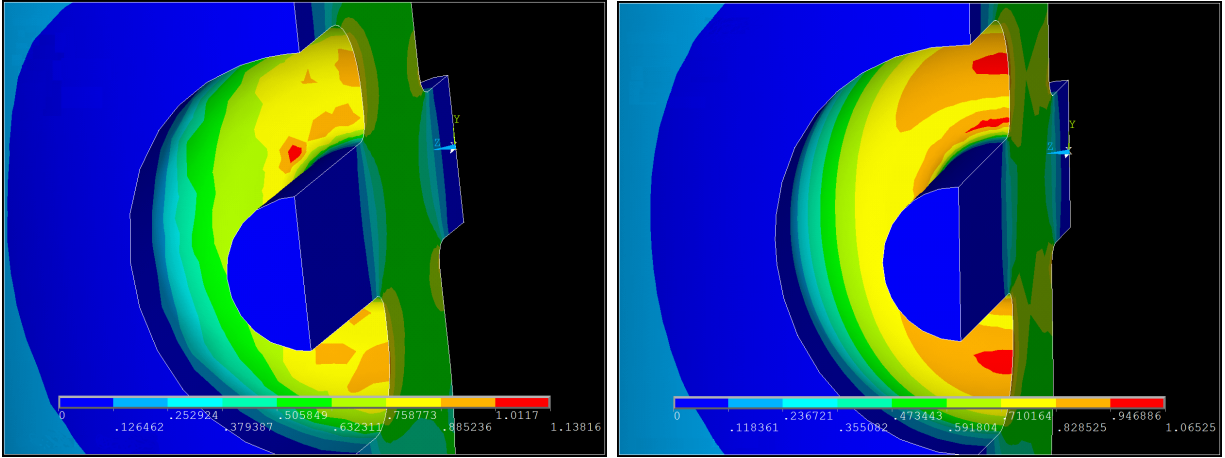


Figure 3.8: Left: Magnitude of the surface electric field on a beam port cup with inadequate meshing for surface field accuracy. Right: Identical geometry with improved meshing and more realistic surface fields.

ficient, extraction of the basic cavity figures of merit can begin. This starts with extraction of bulk properties of the mode and cavity, such as total dissipated power, total stored energy, and cavity volume. These values must be scaled depending on the amount of symmetry used in the cavity. Some solvers automatically do this, but in ANSYS-APDL, it must be done by hand. It should be noted that all stored energy dependent quantities like dissipated power and peak surface fields must be normalized to the stored energy. ANSYS-APDL solves the cavity mode at some nominally small amount of stored energy, and this value must be used to scale the cavity figures of merit. Once the dissipated power, frequency, and stored energy are known, the cavity quality factor can be calculated:

$$Q = \frac{2\pi fU}{P_d}. \quad (3.2)$$

This can then be multiplied by the surface resistance given in the setup phase of the simulation to calculate the geometry factor:

$$G = R_s \times Q. \quad (3.3)$$

The peak surface fields can be found in ANSYS-APDL by making an element table of the field in question. This table can be sorted by field magnitude and the maximum value can be extracted. Again, this is the field value for the nominally low stored energy of the simulation, so  $E_{pk}/\sqrt{U}$  and  $B_{pk}/\sqrt{U}$  should be calculated for later scaling when the proper stored energy is known. The remaining figures of merit require  $V_{acc}$ , and the bulk of the remaining post processing will revolve around its calculation. The first step is to extract the accelerating electric field component along the beam axis. In ANSYS-APDL, this is done via the PATH command, specifying the beginning, end, and field component desired. This gives the value of the accelerating field at a number of discrete points along the line specified, and this number must be large enough for this to be a good approximation of the actual (continuous) accelerating field profile. The first calculation is

$$V_0 = \int_{-\infty}^{+\infty} |E_{acc}(z)| dz = \sum_i^N |E_{acc,i}| \Delta z \quad (3.4)$$

which gives the maximal acceleration possible,  $V_0$ . The next step is calculating the accelerating voltage, which includes the field's variation in time. This calculation uses the general form

$$V_{acc} = \sqrt{\left(\int_{-\infty}^{+\infty} E_{acc} \sin(\omega t) dz\right)^2 + \left(\int_{-\infty}^{+\infty} E_{acc} \cos(\omega t) dz\right)^2} \quad (3.5)$$

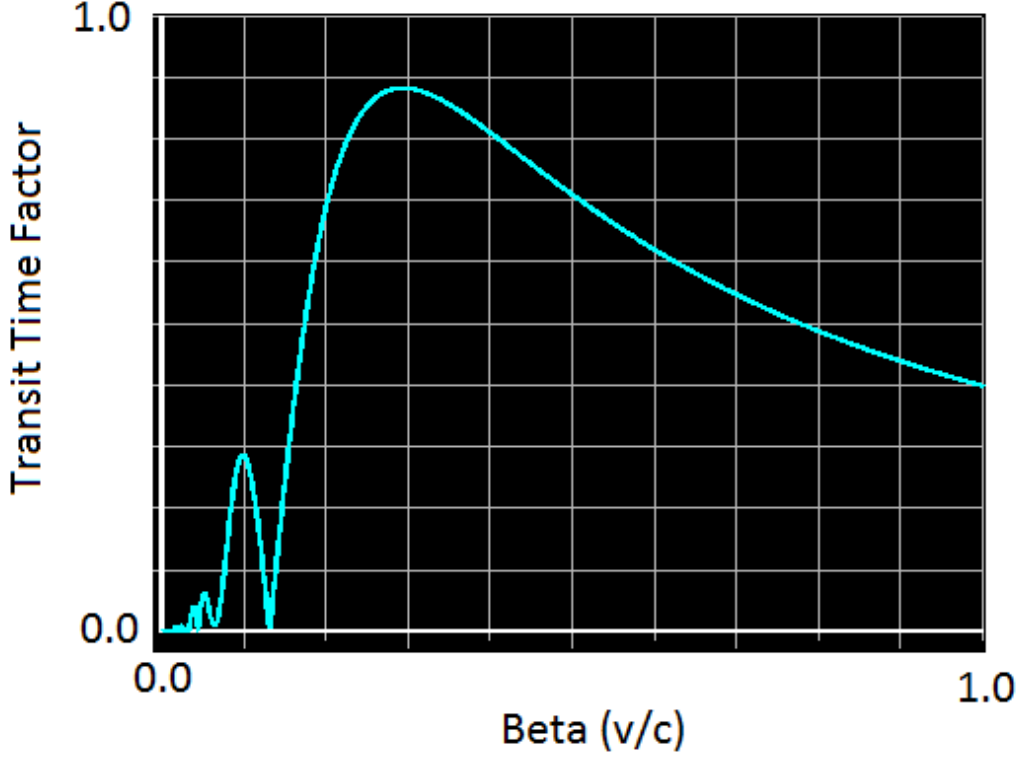


Figure 3.9: Plot of transit time factor versus particle beta.

which does not depend on the choice of ( $z = 0$ ). This becomes

$$V_{acc}(\beta) = \sqrt{\left(\sum_i^N E_{acc,i} \sin\left(\frac{\omega z_i}{\beta c}\right) \Delta z\right)^2 + \left(\sum_i^N E_{acc,i} \cos\left(\frac{\omega z_i}{\beta c}\right) \Delta z\right)^2} \quad (3.6)$$

in practical terms, although this can be simplified sometimes by the choice of ( $z = 0$ ) and cavity symmetry. For instance, a HWR with the origin placed in the geometric center of the cavity can neglect the cos term because of symmetry. This formula depends on  $\beta$ , although does not directly give the optimum  $\beta$ . To find this,  $V_{acc}(\beta)$  is calculated for  $\beta$  ranging from 0.001 to 1 by steps of 0.001. Taking the maximum of this set gives the optimum  $\beta$  with enough accuracy for essentially all applications. This data can be normalized to  $V_0$  to give the transit time factor curve, an example of which can be seen in Figure 3.9. Once



the optimum  $\beta$  has been found,  $V_{acc}/\sqrt{U}$  is calculated, giving the last of the desired field quantities. This is used to calculate  $R/Q$ :

$$R/Q = \frac{1}{\omega} \times \left( \frac{V_{acc}}{\sqrt{U}} \right)^2. \quad (3.7)$$

To find the figures of merit for the cavity at full field, some normalization must be chosen. For the design of the FRIB cavities, it was convention to choose a  $V_{acc}$  desired for a cavity and normalize to that. This determined the stored energy ( $U$ ) from  $V_{acc}/\sqrt{U}$ , and therefore the peak surface fields from the equivalent ratios already calculated. A detailed ANSYS-APDL script used for all of this work can be seen in Appendix A. To this point, the basic electromagnetic figures of merit have been calculated. Sometimes, more details or complex problems needed to be solved, and these often can be solved in post processing. This type of problem often involves field levels or losses on certain parts of the cavity (RF joint, plunger, flange). These problems are solved by selecting the areas, elements, and nodes related to the area in question, and repeating the same process used to extract the fields or losses for the full cavity. If necessary, the losses can be scaled to a different resistivity to simulate a small normal conducting part of the cavity and the quality factor recalculated for the new losses. Examples of this performed in ANSYS-APDL can be seen at the end of Appendix A.

## 3.2 Design of a Beta = 0.29, 322 MHz HWR

The FRIB accelerator has been specified to use two different designs of Half Wave Resonator for the high energy accelerating section. Optimization of the accelerator lattice resulted in the optimum beta of these resonators to be  $\beta = 0.29$  and  $0.53$ , using the fourth harmonic

of the accelerator,  $4 \times 80.5 \text{ MHz} = 322 \text{ MHz}$ . The first half of this section will be spent describing the detailed steps taken during the design of a HWR geometry suitable for FRIB including geometry creation and parameterization, cavity performance optimization, and refinement and simulation of more practical features. The second half of this section will be spent describing the simulation of this cavity's mechanical properties and their interaction with the electromagnetic properties. Finally, the mechanical design of a basic cavity with helium vessel will be discussed and optimized using coupled electromagnetic and mechanical simulations.

### **3.2.1 The Ideal Half Wave Resonator - Revisited**

The scaling of the ideal HWR has been discussed in a previous chapter, but it is obvious that this simple geometry is not practical, let alone optimal for accelerator applications. The ideal HWR has straight, cylindrical outer and inner conductors, and flat short plates at each end. Besides the necessity to get the beam into and out of the cavity, as well as RF power, there are many adjustments that can be made to optimize performance.

### **3.2.2 Beam Tubes and Drift Tubes**

While the ideal cavity geometry generates regions of high electric fields that may be used for acceleration, openings must be created to allow the beam to transit through these regions. The placement of these openings is usually quite obvious: whatever axis passes the beam through the maximum accelerating electric fields. For HWRs, beam ports are cut into the outer conductor, and a drift tube allows passage through the inner conductor, all on the midplane of the cavity. A section view of this positioning can be seen in Figure 3.10.

This positioning takes advantage of the symmetry of the cavity, minimizing steering from tangential electric or magnetic fields. The size of these ports is often driven by the demands of the beam dynamics in the local region of the accelerator. FRIB requires an aperture (minimum opening diameter) for the  $\beta = 0.29$  HWR of 40 mm. These ports have the downside of reducing the R/Q of the cavity by reducing the confinement of the accelerating fields on the beam axis. This is the cause of the significant reduction in the R/Q compared to the ideal cavity, often reducing it by up to a factor of two [28] for most cavity types. For

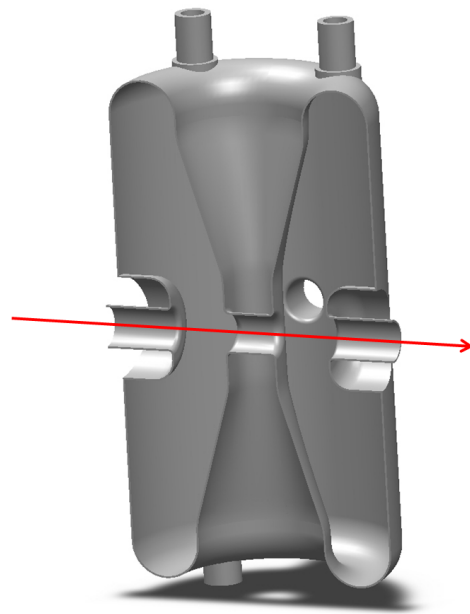


Figure 3.10: Beam port and drift tube position in a HWR with a red arrow indicating the beam axis. One of the RF ports can be seen on the cavity midplane in the background.

example, an ideal HWR designed for  $\beta = 0.29$  has an R/Q of  $\sim 300 \Omega$ , compared to the realistic design for FRIB at this  $\beta$  of  $\sim 200 \Omega$ . This represents a loss in efficiency of roughly 1/3, but something that is necessary for cavity operation. In normal conducting cavities, dissipated power is a driving concern. This drives the design of these cavities to have an aperture as small as possible to increase the R/Q. Because superconducting cavities are peak surface field limited instead of dissipated power limited, this trend is reversed, smoothing the

edges of the beam ports and drift tubes to decrease the field enhancement at that location. Because the aperture of the cavity is driven by external design considerations, little to no optimization is possible on the size and positioning of the drift tube and beam ports.

### 3.2.3 Cavity Geometrical Features and Parameterization

The first, and perhaps most important, step in cavity design is the choice of geometrical features. The initial geometry must include all of the relevant features desired and allow easy optimization of important parameters. The design seen in Figure 3.11 includes all

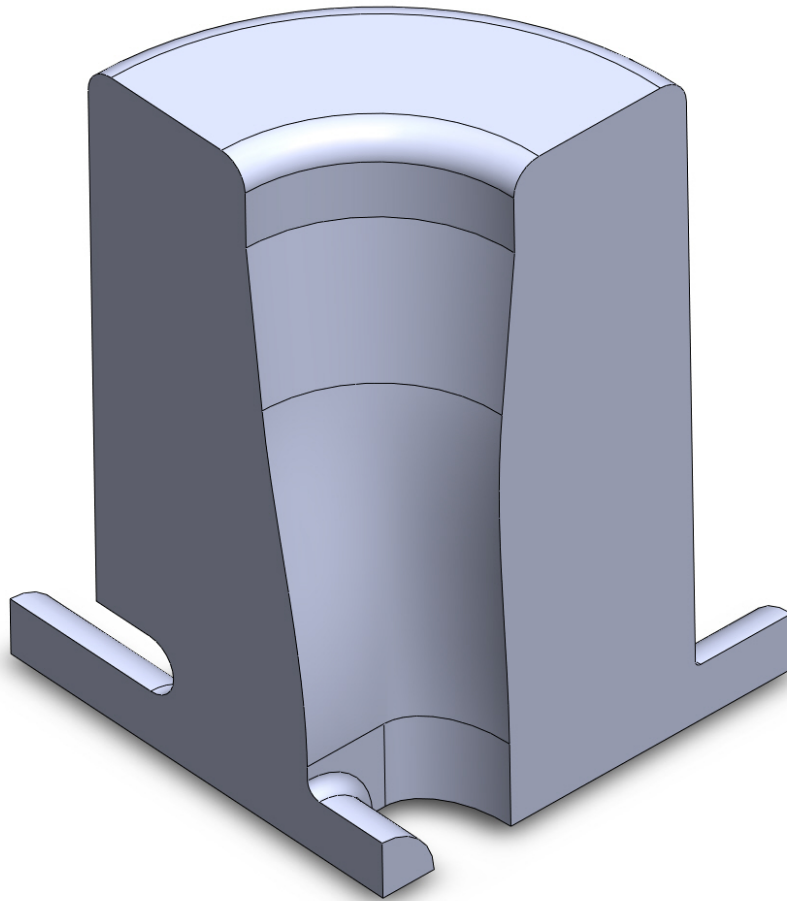


Figure 3.11: HWR vacuum space cut on three symmetry planes.

these features, and provides a good starting place for cavity optimization. The first step in

creating this vacuum space is a rotation of a two dimensional sketch, resulting in the bulk of the symmetric cavity vacuum space, both of which can be seen in Figure 3.12. This sketch

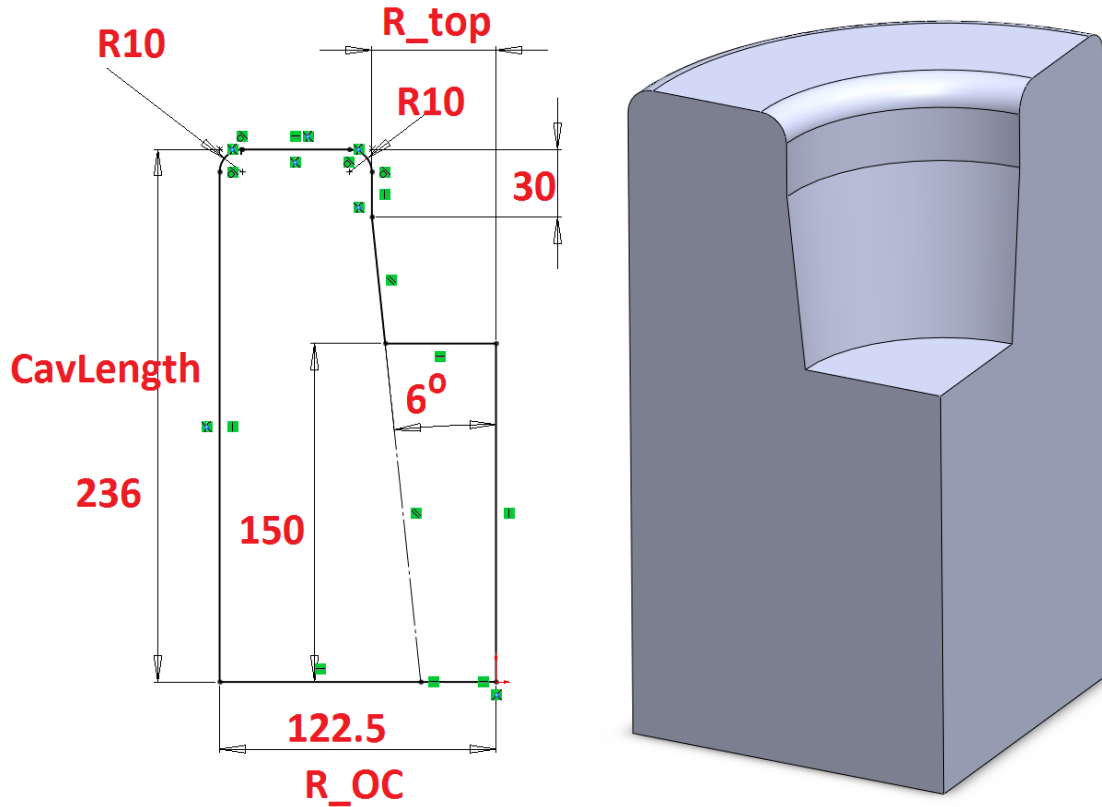


Figure 3.12: Left: Sketch determining the bulk of the cavity vacuum space with dimensions in mm. Right: Resulting volume after the sketch is rotated about the symmetric axis of the cavity. Three symmetric planes assumed.

describes all of the rotationally symmetric parts of the HWR. The length of the cavity, labeled as *CavLength*, will be adjusted to correct the cavity frequency. The magnetic field region can be seen at the top of the sketch, and is drawn such that roughly a third of the inner conductor will be rotationally symmetric. A small straight section on the inner conductor can be seen near the short plate on the inner conductor, with a given radius of  $R_{top}$ . This radius will be adjusted to optimize the peak surface magnetic field. The inner conductor just below that is tapered inward at six degrees toward the electric region, which will be specified

shortly. This allows a smooth transition between the larger magnetic field region of the inner conductor and the smaller electric field region. The outer conductor radius,  $R_{OC}$ , is only limited by the FRIB lattice optimization (145 mm for this cavity). Large  $R_{OC}$  increases the available space for parameter optimization like inner conductor tapering and improves overall cavity efficiency, but makes for a physically larger and mechanically weaker cavity. The major reason for the improvement at larger  $R_{OC}$  is that the gap voltage is determined

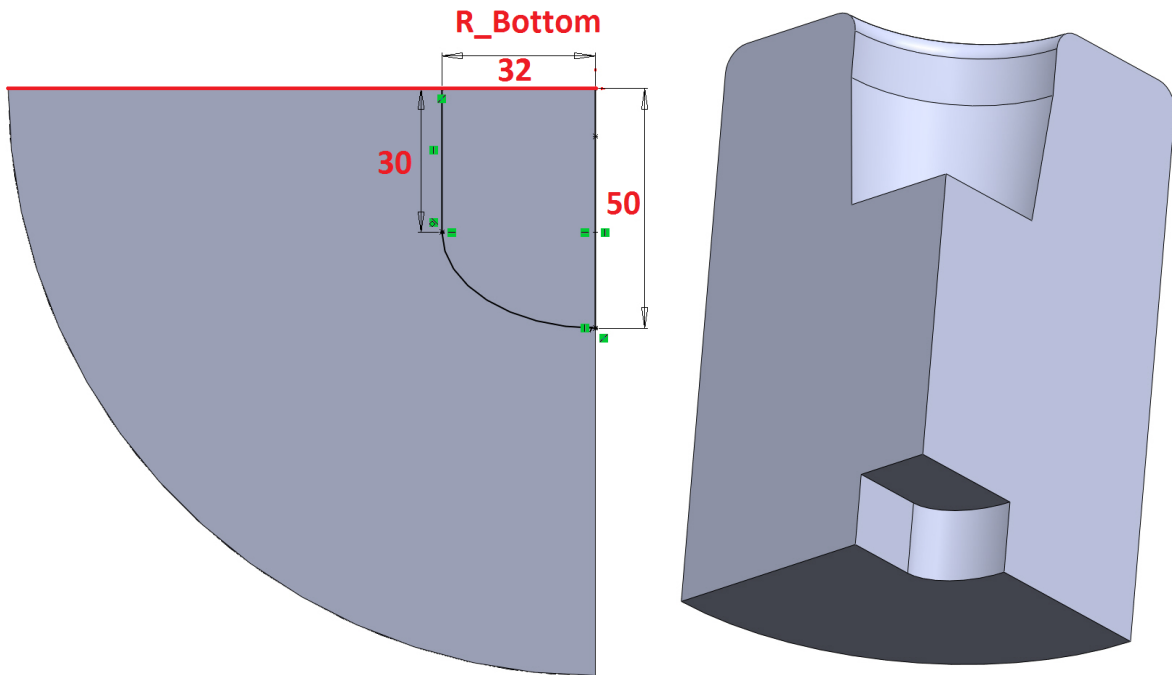


Figure 3.13: Left: Sketch determining the high electric field region with dimensions in mm. Right: Resulting volume after the sketch is cut from the bulk of the cavity. Three symmetric planes assumed.

mostly by the distance from the inner conductor to the outer conductor, the beam port cup simply holds this voltage over a shorter gap. This larger  $V_{acc}/\sqrt{U}$  improves the  $R/Q$  and reduces the peak magnetic field by reducing the required stored energy. The next step in geometry creation is to define the electric field region of the inner conductor. It is desired to have a flat region on the inner conductor for the drift tube to pass through, allowing it to

be smoothly blended into the inner conductor to reduce field enhancement. This is achieved by using a two dimensional sketch called a “racetrack” with a flat region for the drift tube and rounded edges. This sketch and the resulting cut can be seen in Figure 3.13. The length  $R_{bottom}$  will be quite important for both optimization of the peak surface electric field and determining the optimum  $\beta$  of the cavity. The flat region is made large enough in both dimensions such that the drift tube can be blended smoothly into the inner conductor, and an ellipse is used to achieve a smooth rounding of the sides of the inner conductor while allowing adjustment of the inner conductor width. The next step for the creation of the basic inner conductor is the removal of the remaining extra volume to achieve a smooth transition from the radially symmetric magnetic field region to the flattened electric field region. This requires a “lofted” cut, tangential to both the top and bottom surfaces of this extra area. This cutting function in Solidworks smoothly interpolates between the two surfaces using splines for guide functions. The preparatory guide curves and geometry after cutting can be seen in Figure 3.14. An example of what the inner conductor would be, given this vacuum space geometry, has also been included for reference. The final step to complete the inner conductor geometry is the addition of the drift tube. This tube is required by the FRIB lattice to have a radius of 20 mm, and is centered on the beam axis. To smoothly blend the drift tube into the inner conductor, a constant radius fillet is added to the connection, as can be seen in Figure 3.15. The radius of this fillet ( $R_{fillet}$ ) will be used as a final tuning step to optimize the peak surface electric field as the fillet’s location is one of the highest electric field regions of the cavity. An identical process is used to construct the RF port, although the fillet radius is much smaller because the fields in that region are much lower. Although this feature has little impact on cavity performance, and is therefore not required for cavity

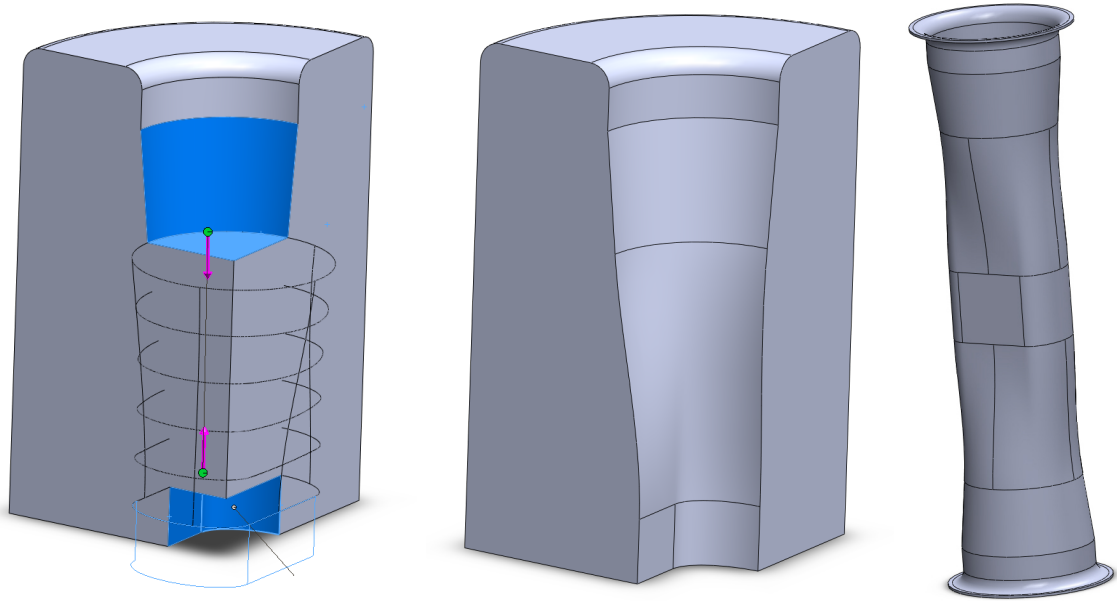


Figure 3.14: Left: Setup for the loft cut to complete the inner conductor shape. Automatic spline guide curves for the cut can be seen in black with the tangential boundary condition shown by purple arrows. Center: Resulting inner conductor shape with smooth transition between magnetic and electric field regions. Three symmetric planes assumed. Right: Resulting inner conductor geometry.

optimization, it is added for completeness. The final geometry that must be included is the beam port and the beam port cup. The beam port cup allows the decoupling of  $\beta$  and  $R_{OC}$ , and gives more variables to control when optimizing the accelerating electric field region. The beam port cup is defined by a sketch that is revolve cut around the beam axis. The sketch and the resulting geometry can be seen in Figure 3.16. While there are many ways to vary the gap for a given  $R_{OC}$  such as tapering the outer conductor back inwards, this geometry combines the customization of the beam port region from the beam port cup with the mechanical stability from a straight, cylindrical outer conductor. The beam port cup is defined by four variables, but the most important is  $L_{cup,2}$  which defines the length of the cup. This variable will be used extensively to correct the cavity optimum  $\beta$  as other parameters are adjusted, while  $L_{cup,3}$  and  $L_{cup,4}$  will be used to optimize the electric



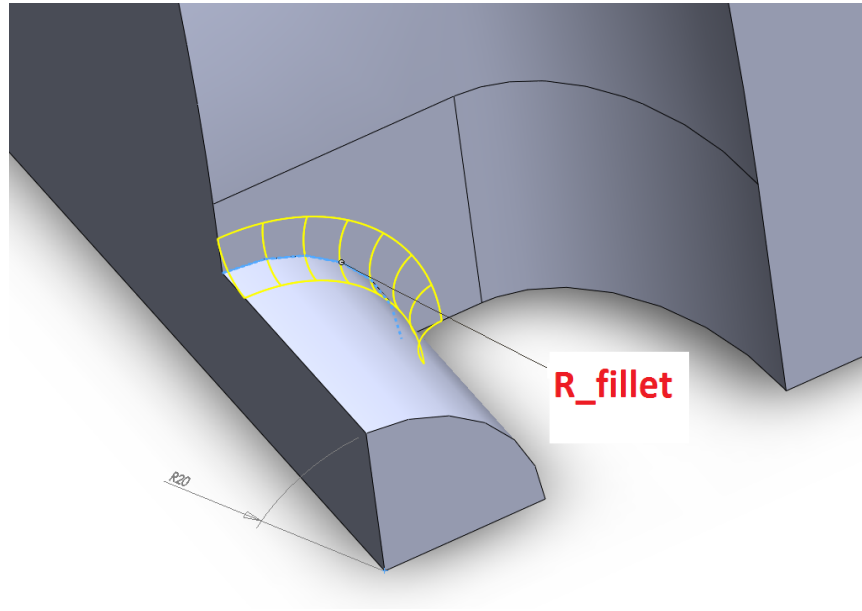


Figure 3.15: After the addition of the drift tube, a fillet is introduced to reduce the field enhancement on the inner conductor. Three symmetric planes assumed.

field distribution on the end of the beam port cup as a refinement at the end of optimization.  $L_{cup,1}$  will be adjusted if needed to reduce the peak surface electric field on the beam port cup, but care must be taken. Increasing the “area” of the beam port cup by increasing  $L_{cup,1}$  increases the capacitance of the cavity. While not an exact model, the cavity can be treated like a simple LC circuit, and increasing the capacitance in this model increases the required current to achieve the same voltage. In the case of a cavity, this increased current means additional losses, and a lower geometry factor. However,  $L_{cup,1}$  must be kept large enough to not dramatically increase the field enhancement on the tip of the cup by allowing more gentle curvature, i.e. larger  $L_{cup,3}$  and  $L_{cup,4}$ .

### 3.2.4 Cavity Performance Optimization Procedure

The geometry developed thus far gives enough parameters to optimize the cavity performance to a high degree. The optimization process for a geometric variable can be seen in Figure 3.17.

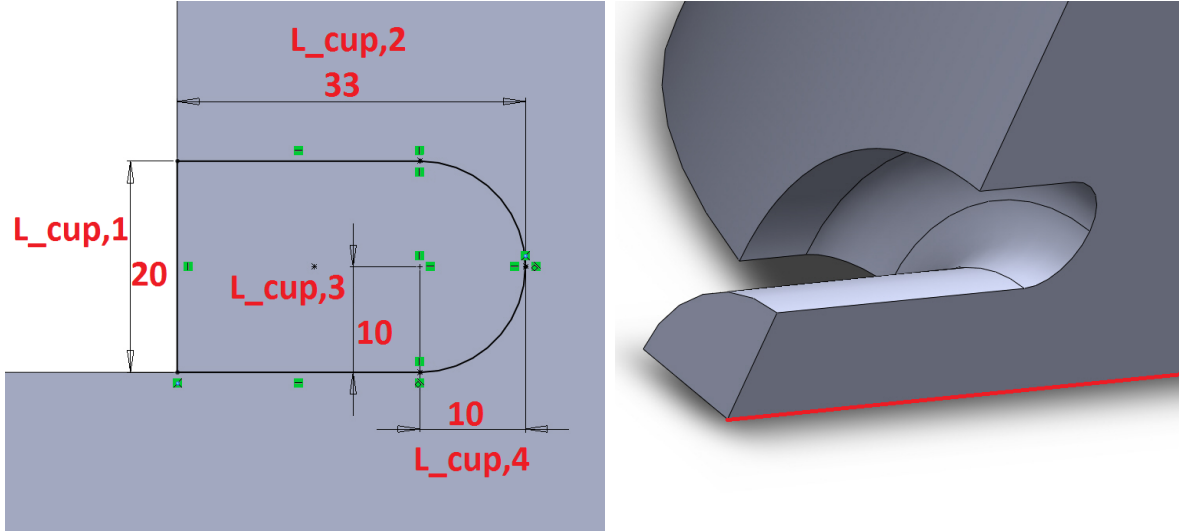


Figure 3.16: Left: Sketch determining the beam port cup with dimensions in mm. Right: Resulting beam port geometry with the beam axis in red. Three symmetric planes assumed.

The first step is to correct the cavity frequency. This will be done by adjusting the length of  $CavLength$  to correct the cavity frequency to  $322 \text{ MHz} \pm 1\%$ . It should be noted that this process is effectively adjusting the inductance of the equivalent LC circuit for the cavity. The size and position of the beam port cup and inner conductor electric field region determines the effective capacitance, and the cross-section of the cavity in the magnetic field region is roughly the equivalent inductance. For this circuit,  $\omega = (LC)^{-1/2}$ , and the desired  $\omega$  is fixed. This model gives a useful intuitive sense of the required adjustments when correcting cavity frequency. The second step, correcting the cavity optimum  $\beta$  to  $0.29 \pm 1\%$ , will be done by changing the position of the beam port cup with  $L_{cup,2}$ . Remembering the scaling of the optimum  $\beta$  of the ideal HWR

$$\frac{\beta_{opt}\lambda}{2} = b + a \quad (3.8)$$

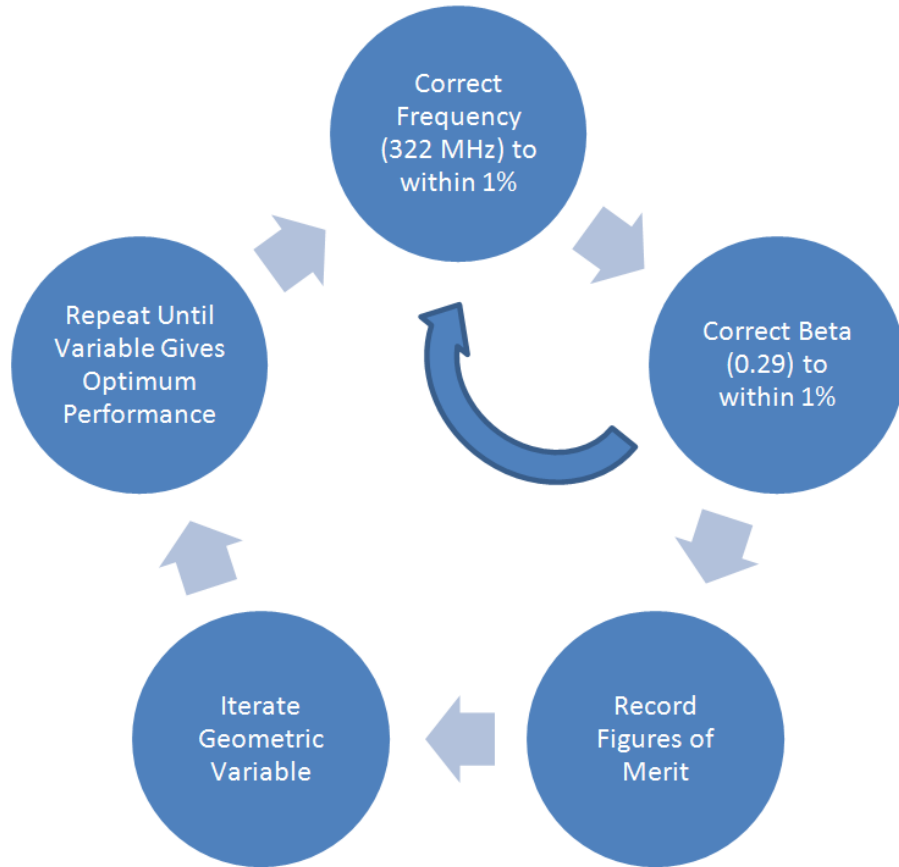


Figure 3.17: The work flow for optimization of a geometric variable.

where  $b$  and  $a$  were the inner and outer conductor radii, the scaling for the cavity optimum  $\beta$  with  $L_{cup,2}$  becomes obvious. This formula cannot, of course, be used directly because in a realistic cavity, the definitions of  $a$  and  $b$  break down. Because changing  $L_{cup,2}$  will change the capacitance of the cavity, it may be necessary to recorrect the cavity frequency, repeating both corrections until the frequency and optimum  $\beta$  are achieved simultaneously. It is interesting to note that the relationship between the beam port cup, optimum  $\beta$ , and geometry factor can be combined to indicate that higher optimum  $\beta$  results in a more efficient cavity, at the same frequency.

There are two tiers of optimization variables for this type of cavity. First are the variables

that will require large scale variation for optimization, and will have significant coupled effects on many, if not all, cavity figures of merit. These variables are  $R_{top}$ ,  $R_{OC}$ , and  $R_{bottom}$ . The first step in cavity optimization is to scan through these variables and find a satisfying balance of figures of merit like peak surface fields and cavity efficiency. These variables can require several rounds of optimization to converge to the best figures of merit. The second tier of variables that are optimized next generally have smaller shifts and a more local effect. These generally only result in fine optimization of one or two figures of merit, like  $R_{fillet}$ , which will primarily change  $E_{pk}$ . These variables generally only required one parameter scan for optimization. The major figures of merit for a cavity are frequency, optimum  $\beta$ , geometry factor ( $G$ ),  $R/Q$ ,  $B_{pk}$ ,  $E_{pk}$ , and stored energy ( $U$ ). For the purposes of this optimization, frequency (322 MHz) and optimum  $\beta$  (0.29) are fixed and all numbers given for other figures of merit will be for a geometry with these figures corrected to within 1%. Because stored energy ( $U$ ) doesn't have a direct impact on cavity performance, it will be quoted, but not optimized for.  $G$  and  $R/Q$  will be maximized for efficiency reasons, and  $E_{pk}$  and  $B_{pk}$  will be minimized for maximum performance reasons, all as discussed elsewhere in this document. The peak surface fields will be quoted as normalized to  $V_{acc} = 1.9$  MV, as required for the FRIB design.

### 3.2.5 Initial Geometry

To begin, the geometry is based on semi-arbitrary dimensions which can be seen in Table 3.1. Using these values, the simulated cavity figures of merit are given in Table 3.2.

Table 3.1: Initial cavity geometrical variables.

Variable	Value (mm)
<i>CavLength</i>	241
<i>R_top</i>	55
<i>R_bottom</i>	32
<i>R_fillet</i>	5
<i>L_cup,1</i>	20
<i>L_cup,2</i>	37
<i>L_cup,3</i>	10
<i>L_cup,4</i>	10

Table 3.2: Initial Cavity Figures of Merit.

Figure of Merit	Value
Frequency	322.5 MHz
$\beta_{opt}$	0.293
$G$	66.5 $\Omega$
$R/Q$	219 $\Omega$
$V_{acc}$	1.90 MV
$E_{pk}$	34.7 MV/m
$B_{pk}$	69.7 mT
$U$	8.15 J

### 3.2.6 Large Scale Optimization

The first parameter scan was done on  $R_{OC}$ , because it is the most likely to generally improve the cavity figures of merit. The results of this scan can be seen in Table 3.3. From this data, it is obvious that making  $R_{OC}$  as large as allowed is extremely beneficial to cavity efficiency. Therefore,  $R_{OC}$  will be set to 145 mm for the remainder of the optimization. It is worth noting that the improvement in  $R/Q$  can be estimated quite easily and accurately

Table 3.3: Outer Conductor Radius Parameter Scan Results.

CavLength	R_OC	L_cup,2	G	R/Q	$E_{pk}$	$B_{pk}$	U
mm	mm	mm	$\Omega$	$\Omega$	MV/m	mT	J
241	122.5	37	66.5	219	34.7	69.7	8.15
239	131.0	48	71.7	236	38.2	64.4	7.56
236	138.0	55	75.2	247	39.7	61.2	7.19
233	145.0	62	78.4	264	39.7	57.9	6.75

from knowledge of the ideal HWR.

$$\frac{R/Q_2}{R/Q_1} = \frac{V_{acc,2}^2}{V_{acc,1}^2} \approx \left( \frac{\ln\left(\frac{b_2}{a_2}\right)}{\ln\left(\frac{b_1}{a_1}\right)} \right)^2 \approx 1.27 \quad (3.9)$$

using  $R_{OC}$  for  $b$  and  $R_{bottom}$  for  $a$ . This agrees well with the simulated results of

$$\frac{R/Q_2}{R/Q_1} \approx 1.21. \quad (3.10)$$

This again shows the power of good understanding of the ideal HWR model. At this point in the simulations, it is clear from the magnetic field distribution seen in Figure 3.18 that the fillets added to the short plate were not enough to reduce the magnetic field there. This prompts the change from a flat short plate with rounding to a fully curved short plate, with geometry that can be seen in Figure 3.19. The short plate has been replaced with a hemisphere of radius  $R_{OC} - R_{top}$ . The definition of  $CavLength$  now can be seen to go to the top of this hemisphere. This geometry change gives a slight improvement in efficiency and peak surface magnetic field, which can be seen in Table 3.4. This change will also improve the stiffness of the cavity, improving the mechanical performance.

The next parameter to sweep is  $R_{top}$ . This will be made large in an attempt to decrease

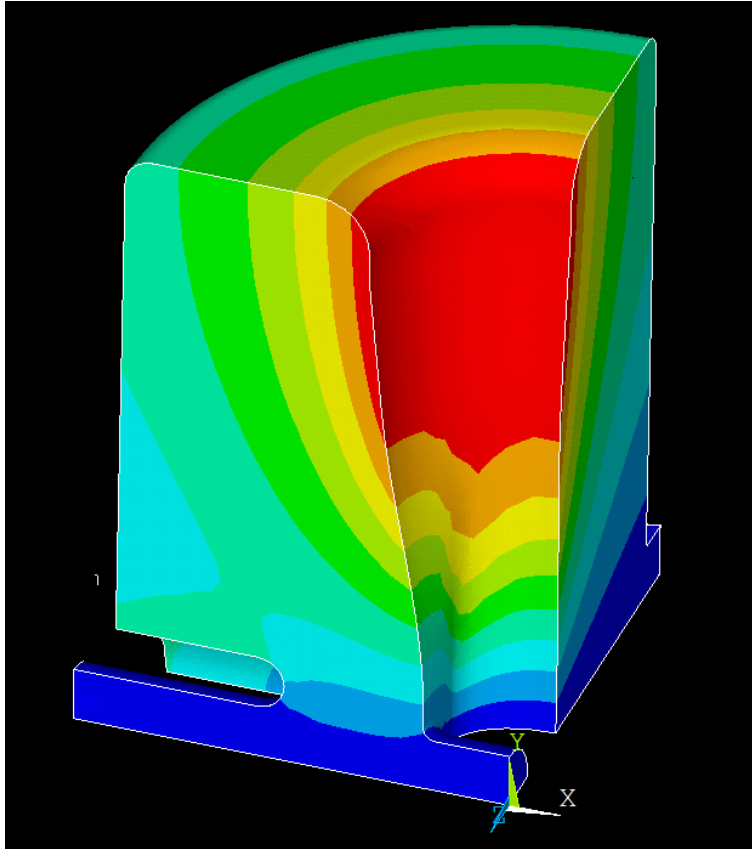


Figure 3.18: Contour plot of surface magnetic field magnitude. The peak magnetic field can be seen where the inner conductor meets the short plate. A change in geometry may improve the peak field value.

the peak surface magnetic field. The results of this sweep can be seen in Table 3.5. Increasing  $R_{top}$  does indeed decrease the peak surface magnetic field, but only to a point. As  $R_{top}$  increases, it can be seen that the efficiency of the cavity drops to the point that the peak surface magnetic field begins to climb again. The improvement in peak surface magnetic field from 65 mm to 75 mm is indeed so small, a final  $R_{top}$  of 65 mm is chosen to keep the efficiency figures of merit as high as possible. The final tier one parameter to sweep is  $R_{bottom}$ . The goal of this sweep is to improve the peak surface electric field, which to this point has been relatively high. The results of sweeping  $R_{bottom}$ , seen in Table 3.6, show a relatively weak dependence of cavity performance on this value. The increase in  $G$  with

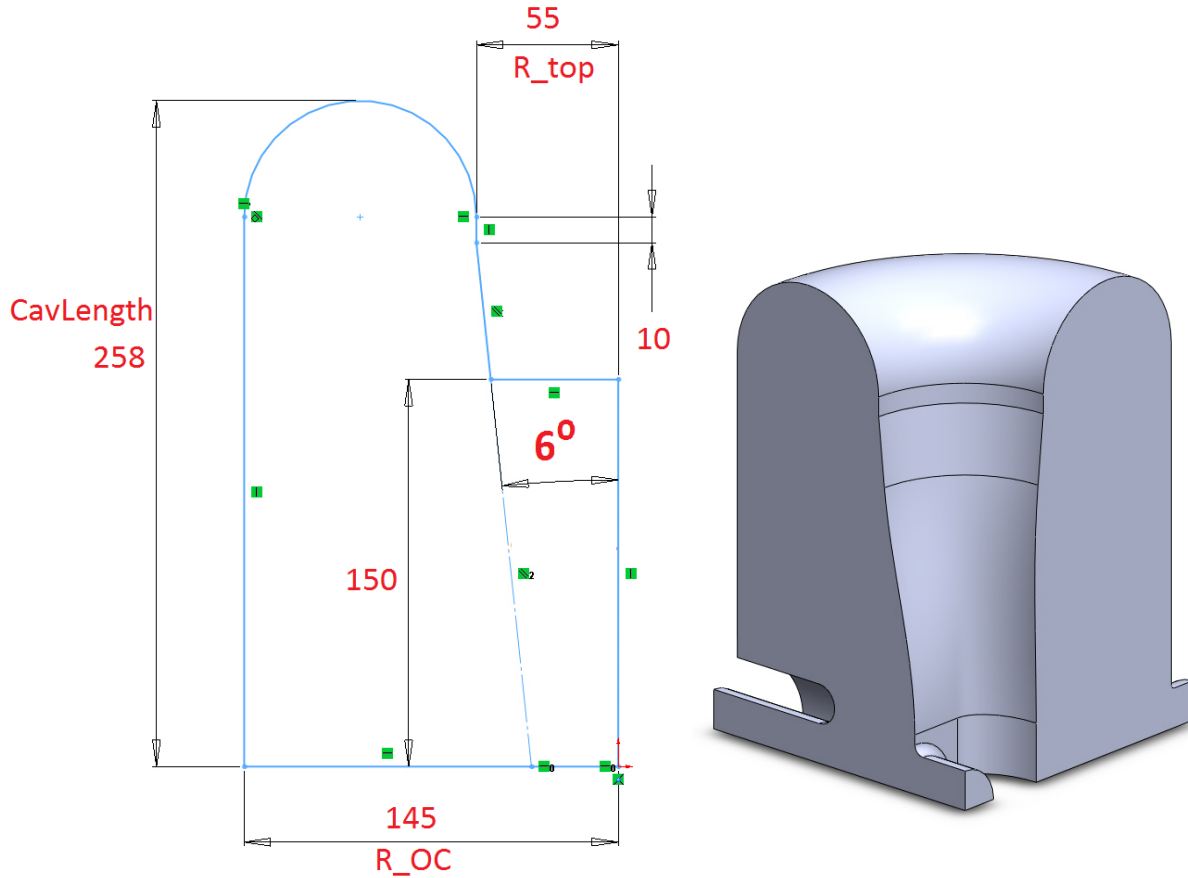


Figure 3.19: New cavity geometry with a hemisphere for the short plate profile.

increased gap size is believable when thought of as a change in capacitance. Increasing the gap size decreases the capacitance, thereby reducing the required current for a given voltage, decreasing losses. While the goal of this part of the optimization is to minimize the peak surface electric field, the increase in peak surface magnetic field and decrease in  $R/Q$  makes  $R_{bottom} = 30$  mm the most attractive value. This concludes the first tier of optimization, and a second round is unlikely to be necessary.  $R_{OC}$  is most certainly the correct size, i.e., as large as possible. The changes to  $R_{bottom}$  was a relatively minor adjustment, with little to no effect on the magnetic field region, making reoptimization of  $R_{top}$  unnecessary.



Table 3.4: Cavity Performance Change due to Hemispherical Short Plate Profile.

Cavity Version	CavLength mm	R_OC mm	R.cup,2 mm	G $\Omega$	R/Q $\Omega$	$E_{pk}$ MV/m	$B_{pk}$ mT	U J
Flat	233	145	62	78.4	264	39.7	57.9	6.75
Rounded	240	145	62	80.1	263	40.2	56.9	6.78

Table 3.5: Inner Conductor Magnetic Field Region Radius Parameter Scan Results.

CavLength mm	R_top mm	R.cup,2 mm	G $\Omega$	R/Q $\Omega$	$E_{pk}$ MV/m	$B_{pk}$ mT	U J
240	55	62	80.1	263	40.2	56.9	6.78
250	65	62	77.4	243	41.1	54.2	7.34
260	75	62	73.1	223	41.3	53.7	8.00
270	85	62	69.1	205	41.6	54.6	8.71

### 3.2.7 Cavity Refinement and Final Results

From here, the optimization falls to the second tier of adjustments, local refinement. From the field plots shown in Figure 3.20, it can be seen that, as the figures of merit would suggest, the most troubling spot remaining is the high electric field on the beam port cup. The final variables to optimize are on the beam port cup. The surface electric fields must be reduced, and this will be accomplished by spreading out the surface fields while keeping the accelerating electric field profile relatively undisturbed. Optimization of the beam port cup is quite complex because almost all variables are coupled strongly, so many rounds of fine scale adjustments are required to converge to the optimal solution. After this optimization process, the final beam port cup geometry can be seen in Figure 3.21 along with the final electric field distribution. The final figures of merit can be seen in Table 3.7. Most of the efficiency improvements came from the large scale changes to the cavity geometry, of which mostly came from  $R_{OC}$  and  $R_{top}$ . Once these changes were done, most of the refinement work came in the high electric field region. This is because most of the complex geometry

Table 3.6: Inner Conductor Electric Field Region Width Parameter Scan Results.

CavLength	R_bottom	R_cup,2	G	R/Q	$E_{pk}$	$B_{pk}$	U
mm	mm	mm	$\Omega$	$\Omega$	MV/m	mT	J
260	26	59	78.8	231	36.9	55.1	7.75
255	30	60	78.2	238	38.5	54.6	7.50
250	32	62	77.4	243	41.1	54.2	7.34
250	34	64	77.8	242	42.3	54.3	7.38

Table 3.7: Cavity Figures of Merit.

Figure of Merit	Initial Value	Final Value	Units
Frequency	322.5	321.8	MHz
$\beta_{opt}$	0.293	0.287	
$G$	66.5	77.7	$\Omega$
$R/Q$	219	231	$\Omega$
$V_{acc}$	1.90	1.90	MV
$E_{pk}$	34.7	30.4	MV/m
$B_{pk}$	69.7	55.8	mT
$U$	8.15	7.71	J

in the cavity is in the high electric field region, especially the beam port cup. Further improvement on the peak surface magnetic field is possible, but only at perhaps greater sacrifice in  $R/Q$  and  $G$ , so these adjustments are deemed unappealing unless the application calls for it. If efficiency is of prime importance, the  $R/Q$  and  $G$  could be improved even further by making  $R_{top}$  smaller, at the sacrifice of higher  $B_{pk}$ .

### 3.2.8 Coupling Power to the Cavity

An obvious but non-trivial feature of any cavity is a port for coupling power from an external generator into the cavity. Coupler design drives the size and positioning of the RF port. For FRIB, it was decided to use electric probe coupling for both input and pickup couplers, ninety degrees rotated from the beam axis, as can be seen in Figure 3.10. While each of

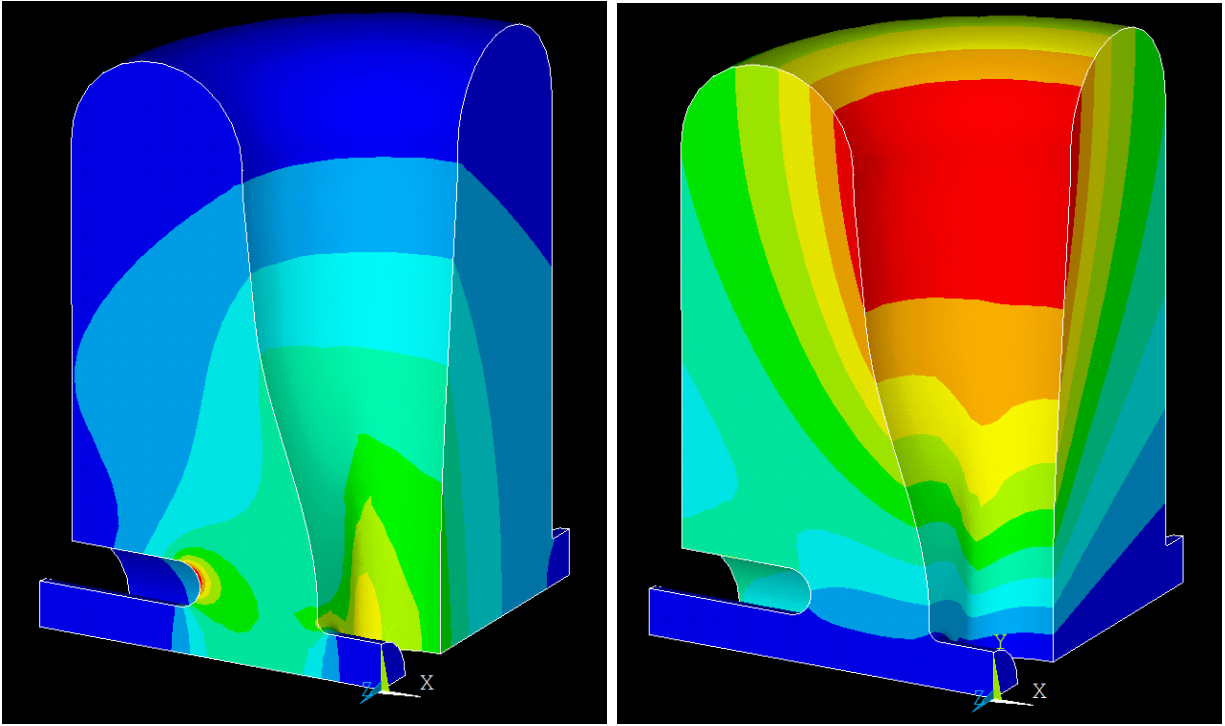


Figure 3.20: Contour plot of surface magnetic field magnitude. Left: Magnitude of the Electric Field after Tier 1 optimization. Right: Magnitude of the Magnetic Field after Tier 1 optimization. Note the high electric fields on the beam port cup.

these couplers will perturb the cavity fields, couplers designed for high power are often much larger than testing couplers, and will perturb the cavity more to achieve the desired stronger coupling. These disturbances will shift the resonant frequency of the cavity and must be taken into account during design, although the shift itself is often measured experimentally. Good coupler and cavity interface design also ensures that regions of high surface fields are not created around the coupler port, although the location of the RF port on the outer conductor means this is not generally challenging. Additionally, the coupling strength as a function of probe length can be simulated with a standing wave simulation. A typical geometry for this type of simulation can be seen in Figure 3.22. The coupling strength of the port can be simulated by solving the model with the termination of the coupler port (indicated by a red arrow in Figure 3.22) as both PEC and PMC, and extracting the fields

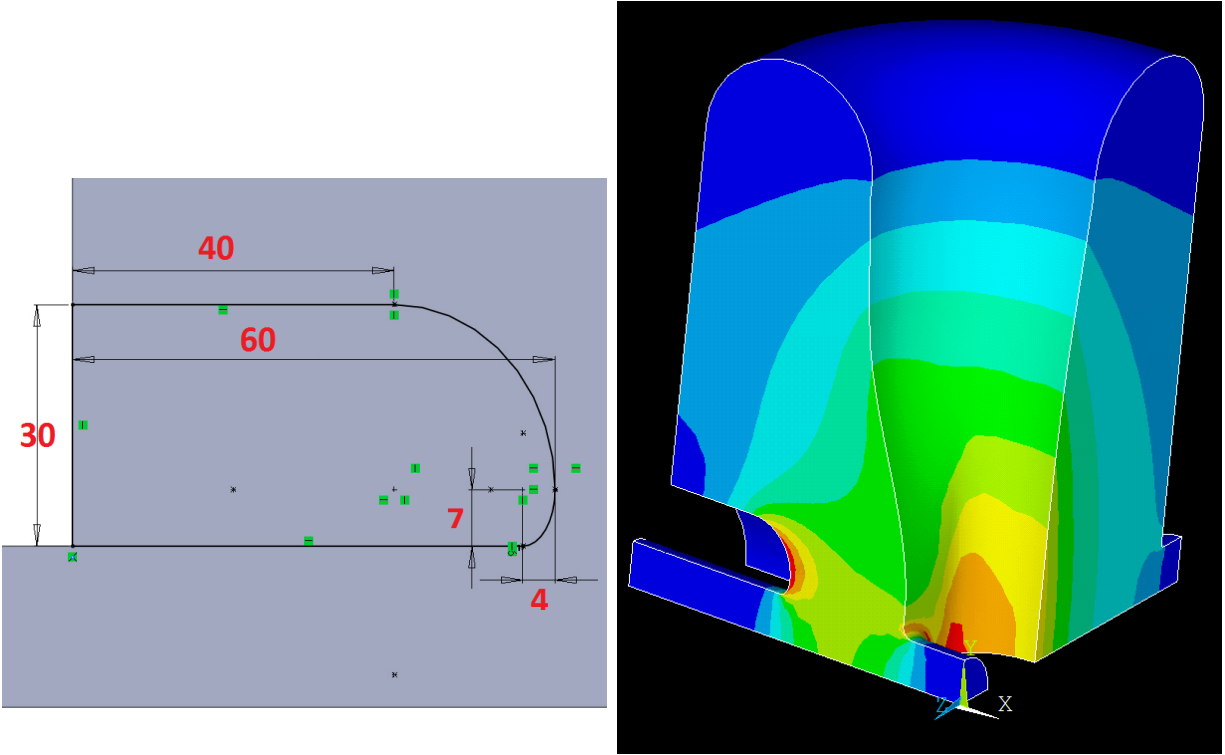


Figure 3.21: Left: Final beam port cup geometry. Right: Magnitude of the Electric Field after optimization.

on the boundary. This is called the Current-Voltage method [38, 39], and assumes that the fields in the coupler port are purely TEM at the termination. At the PEC termination, the electric field is zero because the TEM only allows fields transverse to the surface, but these are forced to zero by the PEC condition. The distribution of the magnetic fields can be seen in Figure 3.23, and it has the characteristic  $1/\rho$  dependence of a coaxial TEM mode. An identical distribution for the electric field is seen when the cavity is simulated with a PMC termination. The Current-Voltage method uses a lumped circuit for the coaxial transmission line, and calls for the calculation of the “voltage” between the inner and outer conductor on a PMC boundary and the “current” across the termination for a PEC boundary. Using this model, we can calculate  $Q_{ext}$  as

$$Q_{ext} = Q_i + Q_v \quad (3.11)$$

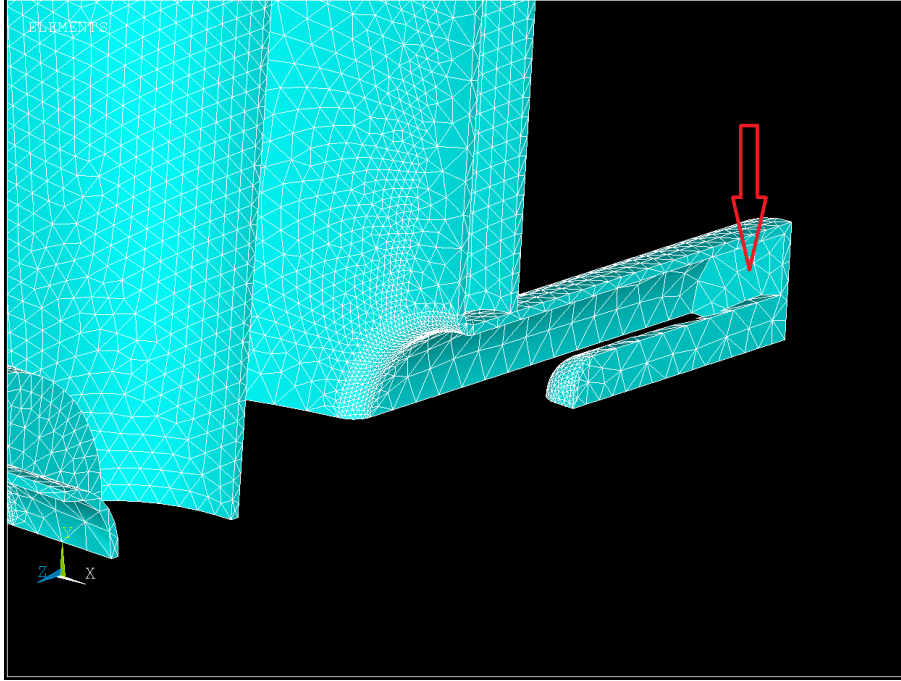


Figure 3.22: The coupler probe can be seen in the foreground connected to the RF port by the surface planes indicated by the red arrow. This is a quarter of the geometry cut on the symmetry planes.

where

$$P_i = \frac{\omega U}{Q_i} = \frac{1}{2\eta} \int_S |\vec{E}|^2 ds \quad (3.12)$$

and

$$P_v = \frac{\omega U}{Q_v} = \frac{\eta}{2} \int_S |\vec{H}|^2 ds \quad (3.13)$$

following the standard definition of a quality factor. The form of a TEM wave in a coaxial transmission line gives a relatively simple form for  $Q_{ext}$ :

$$Q_{ext} = \frac{\omega U}{\pi \ln\left(\frac{b}{a}\right)} \left( \frac{\eta}{(aE_{pk})^2} + \frac{1}{\eta(aH_{pk})^2} \right) \quad (3.14)$$

where  $a$  and  $b$  are the inner and outer conductor radii for the coupler port,  $\eta = 377 \Omega$  is the impedance of free space, and  $E_{pk}$  and  $H_{pk}$  are the peak fields on the termination for the

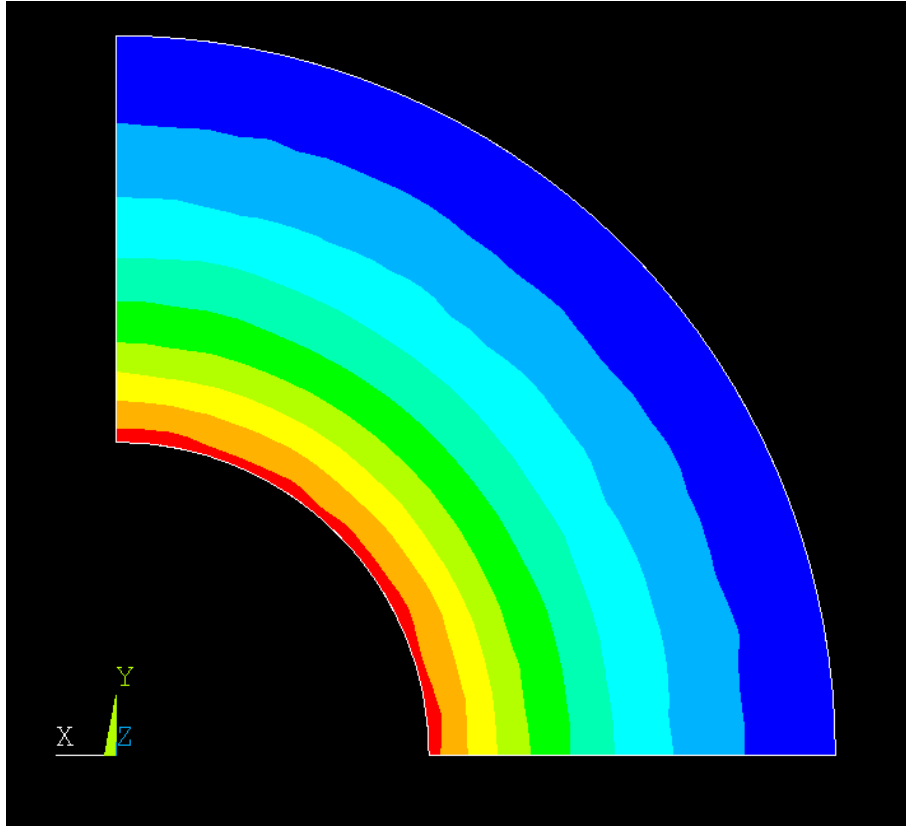


Figure 3.23: Plot of the magnitude of the magnetic field on the PEC termination of a coupler port. Simulated with planes of symmetry in  $x$  and  $y$ .

PMC and PEC boundary conditions, respectively.

Comparison of simulation and measured data for a prototype  $\beta = 0.53$  HWR can be seen in Figure 3.24. The details of measuring the  $Q_{ext}$  on a real cavity will be discussed in Chapter 4. The most error-prone part of this measurement is the transformation of a given coupler tip length to penetration into the cavity volume. While this is easy to do in a CAD model, errors in manufacturing and positioning add significant error to this part of the measurement. This can be seen in the data plotted in Figure 3.24, where the measured values (thin black trend lines) and the simulated data (large black squares) are offset from each other by as much as 5 mm. This can even be seen in the shift between different measurement runs which are a similar distance apart. The slope of the measured and simulated data agrees

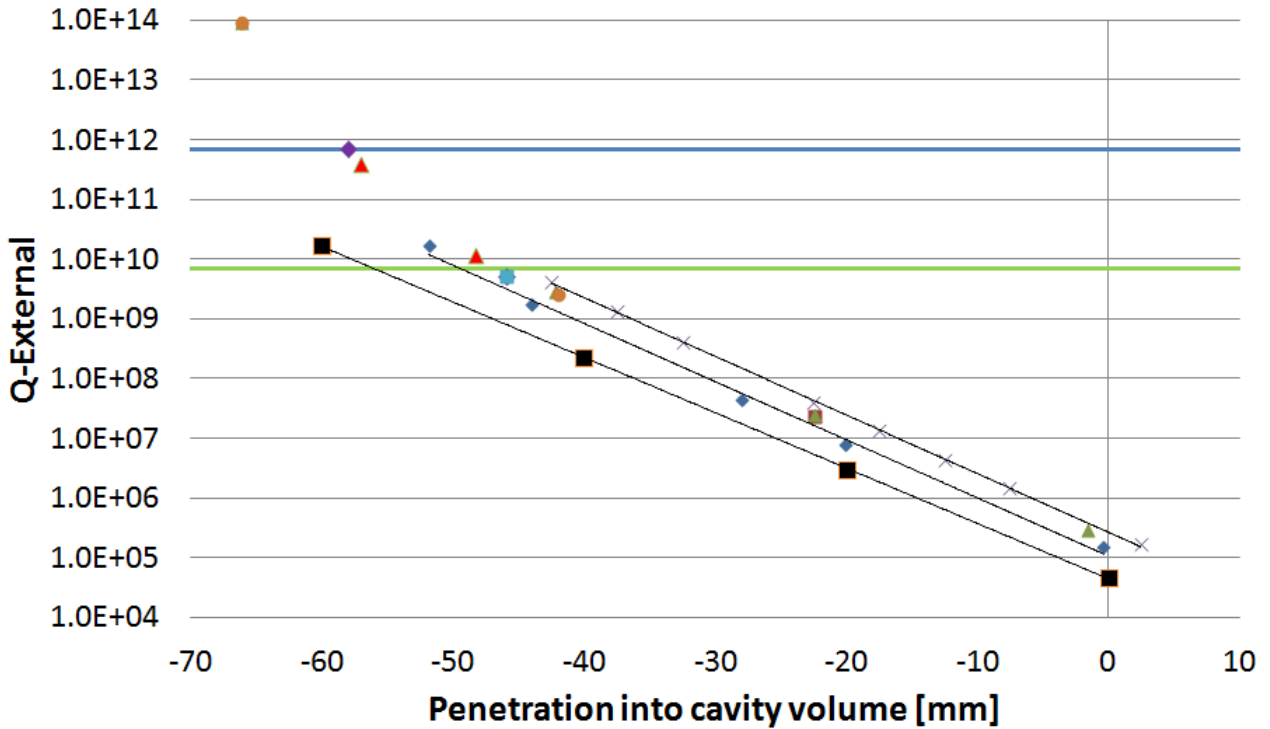


Figure 3.24: Plot of measured and simulated Q-externals for a 0.53 HWR prototype. The simulated data is represented by the large black squares. The rest are repeated rounds of measured data.

well, however. This is because the errors in fabricating the port diameter and measuring the coupler probe diameter are much smaller, and can be simulated accurately. It is important to notice that at very negative penetration into the cavity (very small probe lengths), the trend line changes significantly from both the measured and simulated data. This is because the approximation used in the simulation breaks down significantly for very small probe lengths, the modes no longer have enough space to transform into a pure TEM shape before reaching the termination plane of the RF flange. To accurately model this behavior, a more advanced theoretical method or a traveling wave simulation is required. These additionally require a much more accurate description of the geometry involved, including the coupler feed through and flange shape.

### 3.2.9 On the Subject of Rinse Ports

A practical concern for cavity manufacturing is access to the RF surface inside the cavity. While the RF and beam ports provide some access, additional ports have been added on one of the short plates to assist in cavity processing. While their addition does not significantly reduce cavity efficiency, these ports perturb the magnetic fields on the short plates, enhancing the magnetic fields in the region. The port must be blended into the short plate with a fillet with a radius large enough to ensure the surface magnetic fields in the region are lower than the peak surface fields in the rest of the cavity. A rinse port with fillet, as well as a study of surface magnetic field on the rinse port versus fillet radius can be seen in Figure 3.25. If increasing the port fillet does not reduce the surface magnetic field enough,

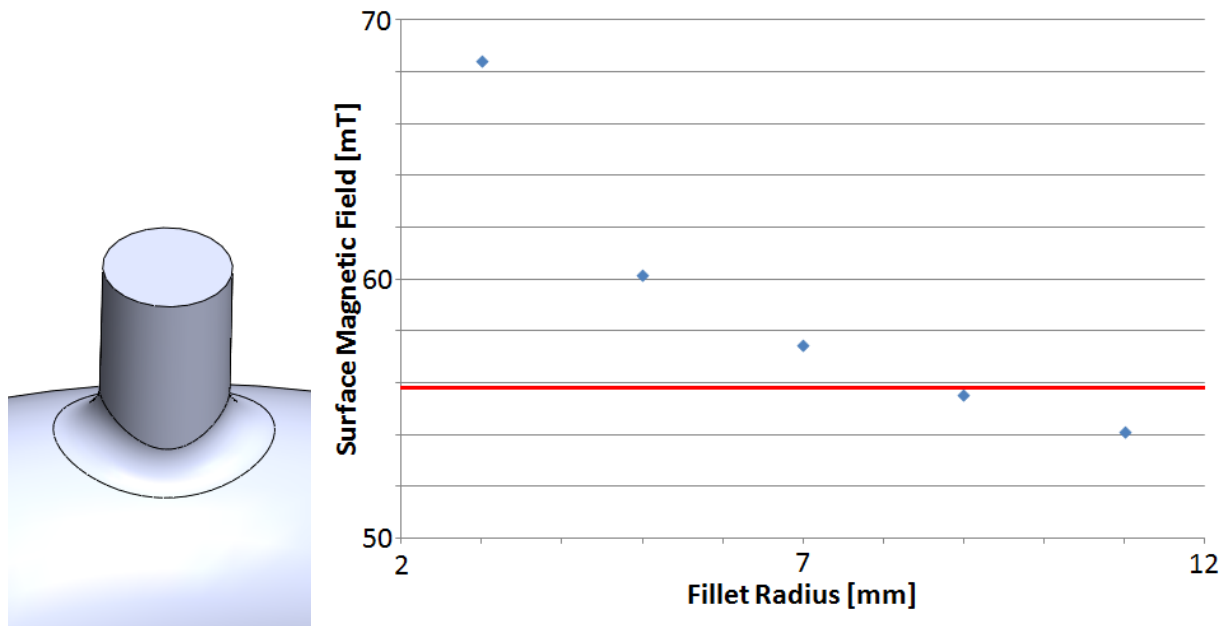


Figure 3.25: Left: Rinse port on a HWR short plate with fillet. Right: Plot of surface magnetic field on the rinse port versus radius of the fillet. The red line indicates the peak surface magnetic field in the rest of the cavity.

then the port can be moved radially outwards on the short plate. While the requirement for proper draining will limit how far the port can be moved in this way, the fields will be



reduced by taking advantage of the  $1/\rho$  scaling of the magnetic fields in coaxial resonators. If neither of these methods is satisfactory, then either the rinse port diameter must be reduced, or a serious redesign of the short plate geometry must be considered. This is perhaps, unappealing if the peak surface magnetic field is only increased by a very small amount, although this decision is very situational. The balance of improved cavity processing and increased complexity of manufacturing is something that must be done experimentally, it has not yet been demonstrated that cavities of this design style can be reliably processed without these rinse ports.

### **3.2.10 Beam Port Cup Positioning Sensitivity**

The last step in fabrication of a HWR of this style is the welding of the beam port cups. The freedom of positioning the cups gives a powerful tool for correcting other fabrication uncertainties which lead to frequency spread in manufactured cavities. Additionally, the cups can be moved with respect to the cavity inner conductor to achieve an acceptable field flatness in the cavity (both gaps having roughly equal field amplitude). This tool, however, has practical limits because of the sensitivity of other cavity figures of merit to the cup positioning. These sensitivities can be estimated by EM simulation quite easily, and the results of this study for this HWR design can be seen in Table 3.8. The figures of merit most sensitive to this displacement are the frequency and peak surface electric field, which is intuitive. For a relatively modest shift in beam port cup position, only a few millimeters in either direction, several megahertz of frequency shift can be achieved. The shift in other figures of merit should be manageable within this large range, although all reasonable effort should be made to fabricate the cavity to require as little of this mechanism as possible. A

Table 3.8: Cavity Figure of Merit Sensitivity to Beam Port Cup Position. Cup displacement ( $X$ ) is the distance each cup is symmetrically moved from nominal with the positive direction being towards the inner conductor.

$d\beta_{opt}/dX$	$df/dX$	$dG/dX$	$d(R/Q)/dX$	$dE_{pk}/dX$	$dB_{pk}/dX$
$\frac{1}{mm}$	$\frac{MHz}{mm}$	$\frac{\Omega}{mm}$	$\frac{\Omega}{mm}$	$\frac{MV}{m \cdot mm}$	$\frac{MV}{m \cdot mm}$
-0.0026	-0.82	0.075	-0.22	0.54	-0.077

more detailed optimization and error study for the accelerator lattice would be required to put more absolute limits on the deviation of  $\beta_{opt}$ .

### 3.2.11 Etching Coefficient Estimation

A major step in cavity processing is a bulk etching of the RF surfaces. The goal of this etching is to remove around 150  $\mu\text{m}$  of material from the RF surface that has been damaged by cavity fabrication, improving cavity performance. This etch generally changes the cavity frequency enough so as to require that this shift be well understood so that the correct final frequency can be repeatably achieved. Using Slater's Theorem (see Section 3.3.4)

$$\frac{\Delta f}{f_0} = \frac{1}{4U} \int_{\Delta V} (\epsilon_0 E^2 - \mu_0 H^2) dV \quad (3.15)$$

this shift can be perturbatively estimated. Because the simulation procedure requires the volume be broken into discrete elements, this formula requires modification to:

$$\frac{\Delta f}{\Delta T} = \frac{f_0}{4U} \sum_i (\epsilon_0 E_i^2 - \mu_0 H_i^2) dA_i \quad (3.16)$$

where  $\Delta T$  is the thickness of the etched layer,  $A_i$  is the area of the external face of element  $i$ , and the fields  $E_i$  and  $H_i$  are the fields from surface element  $i$ . For an ideal HWR, this can be calculated directly from Slater's theorem:  $-1383 \text{ Hz}/\mu\text{m}$ . This large negative shift is intuitive because etching of an ideal HWR effectively makes the cavity longer, directly lowering the cavity frequency. In the process of cavity optimization, the changes to the electric field region increase its contribution to this shift greatly, producing a less negative coefficient. For the HWR design being developed here, the simulated etching coefficient is  $-206 \text{ Hz}/\mu\text{m}$ . In reality, this calculation makes assumptions that are unlikely to be true. The most important one is that the etching is uniform over the cavity surface, but etching is a quite complex and dynamic process, involving both fluid dynamics and thermodynamical issues. What can be said is that, in an ideal etching setup with very good temperature and flow control, the achieved frequency shift should approach the simulated value. Of additional interest is using etching as a way to fine-tune the frequency of a cavity. This process is called differential etching, etching shift versus the acid fill level can be seen in Figure 3.26 for an example HWR. This process has been demonstrated and used for cavity production for QWRS at TRIUMF [40] and elsewhere. From this plot, it can be seen that a much more positive frequency shift can be achieved if the cavity is filled such that the full electric field region is etched while only one of the magnetic field regions are etched. Experience gained from fabricating a cavity design is required to determine if such a cavity tuning process would need to be developed.

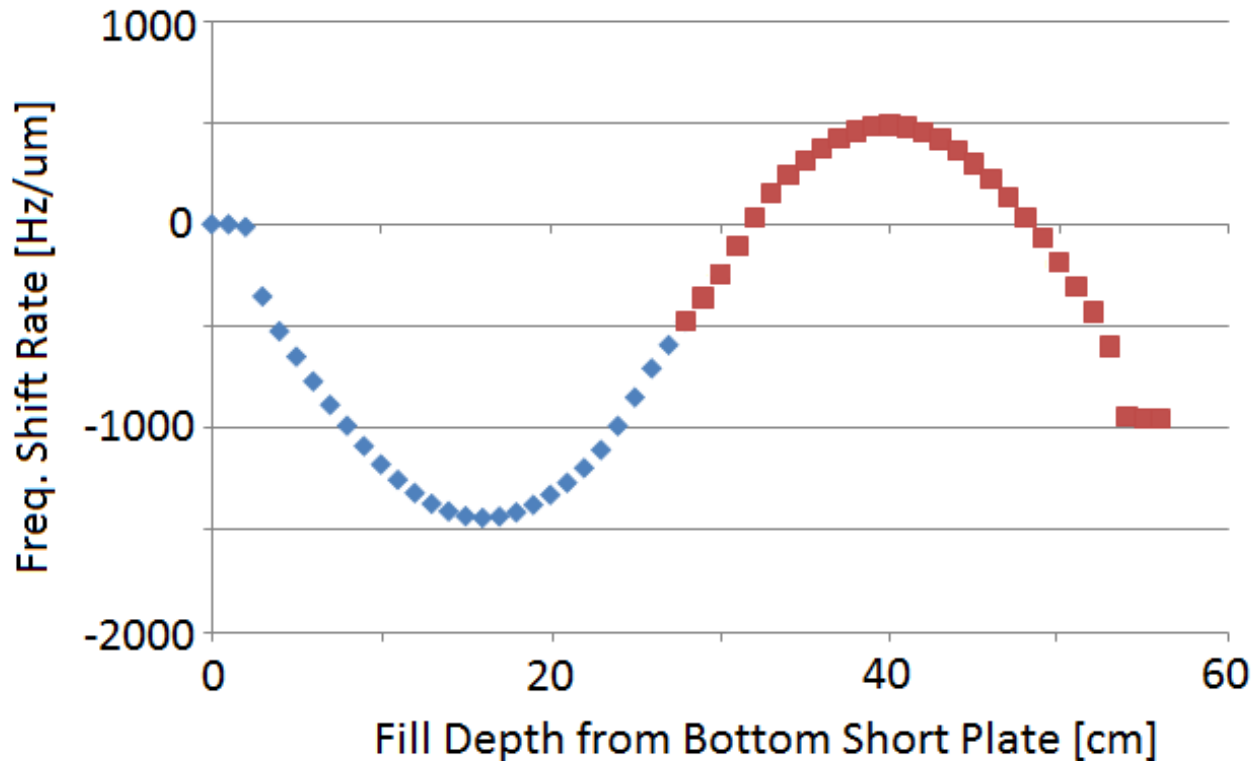


Figure 3.26: Plot of simulated etching coefficient for a prototype  $\beta = 0.53$  HWR filled with acid to different levels. The blue diamonds represent simulation data, and the red squares are this data mirrored assuming symmetry.

### 3.3 Coupled Electromagnetic and Mechanical Simulations

A mature cavity design starts with an electromagnetic model, but must account for various practical concerns. During normal operation, the cavity walls may be subjected to small forces, which will result in small perturbations to the shape of the cavity. This deformation will change the cavity vacuum space, and therefore the resonant frequency. This can have significant controls implications and must be evaluated and optimized before cavity production. Because matching the simulation setup to the exact conditions the cavity will see in operation is difficult, several rounds of simulation and prototyping can sometimes be

required to achieve the accuracy and performance desired. In this section, the procedure for this type of simulation, the types of pressures simulated, and the results of these simulations for the HWR developed in the last section will be discussed in detail.

### 3.3.1 Generalized Procedure

The mechanical simulation process has many parallels to the electromagnetic simulation procedure. The major steps remain Geometry Creation/Setup, Meshing, Solving, and Post-Processing. From the cavity vacuum geometry, the SHELL command in SolidWorks will create the niobium space that represents the cavity walls. This command has the option to shell with multiple thicknesses in different parts of the cavity, and this can be used to model cavities made from materials of various thicknesses. From this, the helium vessel can be constructed around the cavity, using different bodies for different materials. Once the material space has been generated, it is exported as a SAT (or other appropriate file type) file for importation into ANSYS. Once in ANSYS, the different bodies must be “glued” together. This command (“VGLUE”) takes different volumes that are next to each other and joins them for simulations purposes. Before this command is given, two volumes may be touching, but where they touch they both have their individual surfaces with no reference between them. After the command, the redundant surfaces are removed so that the different volumes *share* a common surface, meaning that the mesh and mechanical forces will be shared across the boundary, effectively binding them together. From the material space of the cavity, seen in Figure 3.27, the vacuum space must be recreated. This is done by using the existing geometry as the base for the remaining areas needed to create the continuous set of areas that define the vacuum space: symmetry faces and ends of ports. Once these are created and

the vacuum space has been created, all volumes must be meshed. Because there are volumes that share the same areas, most notably the vacuum space and the cavity space, special care must be taken to mesh in the correct order with the correct refinement to give a satisfactory mechanical and electromagnetic solution. For this purpose, it is highly recommended to use second order elements for the electromagnetic simulation. Using the very fine mesh required for a satisfactory electromagnetic solution will almost certainly force there to be an extremely high number of elements in the mechanical simulations, unnecessarily stretching the limits of even a very high powered computer. Other than this caveat, the procedure for performing the electromagnetic simulation is the same as described at the beginning of this chapter. Once the frequency is simulated, the next step is the setup of the mechanical simulation. This includes giving all volumes the appropriate material properties, including the vacuum space. This may seem counter-intuitive, but treating the vacuum space like a material is essential for accuracy. This is because this process preserves the meshing in the vacuum space, allowing it to be perturbed by the mechanical deformation, providing a far more accurate result than remeshing after the mechanical simulation. The material properties used for the various mechanical simulations can be seen in Table 3.9, all of which are for cryogenic temperatures.

Table 3.9: Material Properties used for Simulation.

	Elastic Moduli	Major Poisson's Ratio	Mass Density
	Pa	-	kg/m <sup>3</sup>
“Vacuum-ium”	1	0.38	0.01
titanium	1.23E11	0.338	4510
niobium	1.25E11	0.301	8570
304 Stainless Steel	2.00E11	0.33	7860
niobium titanium	1.24E11	0.32	5700

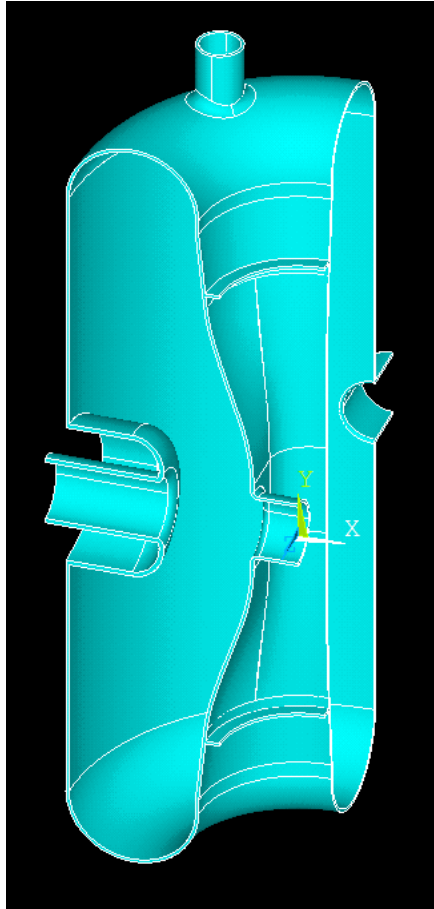


Figure 3.27: Material space after importation into ANSYS-APDL.

The remaining steps before starting the simulation are applying the pressure to be studied and the boundary conditions. The forms of the pressures will be discussed later in this section. The boundary conditions are of critical importance for this type of simulation. First, any faces on symmetry planes must be constrained to stay in that plane, i.e. fixing the variable defining the plane while letting the two other degrees of freedom float. Then the simulation must be fixed in space. If you are using three symmetry planes, then this is automatically done. If two or less planes of symmetry are being used, at least one part of the cavity (a point that is on *all* symmetry planes used) must be fixed. While this will not change the simulation result, it will prevent the solution from diverging if the applied

force isn't symmetric. Additionally, other parts of the geometry can be fixed, based on the situation you are trying to simulate. An example of this is the relationship between a HWR and its tuner. While simulating how much force the tuning will require, the beam ports cannot be fixed, but when doing some other simulation that assumes the tuner is in place, fixing the beam port flanges in their normal direction is a good approximation. If more detailed studies are required an effective spring boundary condition can be applied to simulate, for instance, a weakly compliant tuner. After solving for the deformation, the meshing in the material space can be discarded, and the vacuum space material should be reset to true vacuum. The deformation should be kept by updating the coordinates of the mesh nodes. Once the simulation is switched back to modal from structural, the standard electromagnetic simulation procedure should be used to get the new frequency. The difference between the first and second frequency is the frequency shift for the applied pressure.

### **3.3.2 Geometry Modification for Simulation**

Without careful consideration of the geometry, the number of elements in a mechanical simulation can become needlessly large. Therefore, serious thought must be put into a cavity solid model before simulations can proceed. A mechanically designed model will include many small surfaces/features that are required for fabrication, but will make accurate simulation effectively impossible. It is necessary to make certain geometrical changes to the model before it is simulated to ensure both accuracy as well as efficiency. Some of these geometry features will not exist in the finished cavity, but are required for fabrication. An example of this would be a small cut in preparation for welding of two subassemblies that will be obliterated by the welding process, leaving a much smoother surface. This type of feature must



be modified to accurately represent the final geometry as well as possible. In non-sensitive areas, this type of feature can be safely removed entirely, which will give great benefit in simulation performance with almost no sacrifice in the result's accuracy. The second type of geometry feature that can be changed are small details that are totally unrelated to electromagnetic performance and have little to no impact on mechanical performance. Excellent examples of this type of feature are bolt holes and chamfers on parts of the cavity vessel. These features will exist in the finished cavity, but do not affect the cavity vacuum and do not change the mechanical properties of the cavity assembly. These features are often quite small as well, leading to dense local mesh that is not required. Removing these two types of features can drastically improve simulation efficiency by reducing meshing requirements, an example of this process can be seen in Figure 3.28. It is, indeed, even common for these types of features to forestall any simulation because of the complexity of meshing them. Many of these features can include overlapping volumes or other small/non-physical features that will need to be fixed before any work can be done. Additionally, even if they can be meshed, the density required may be so high as to exceed the limits of the available simulation hardware. Additionally, simplifications can be made to allow estimates of less critical figures of merit. An excellent example of this is the removal of bellows from a mechanical simulation. Their removal greatly simplifies the model by removing all of the associated small/delicate features while allowing relatively accurate simulations. This is achieved by replacing the bellows with a contact body with an effectively equivalent spring constant, or depending on the level of deformation under study, they can be safely removed all together. This modification must include more careful deliberation of the consequences involved, and the increased error of this modification. Additionally, small gaps between volumes must be

removed to allow “gluing” during meshing.

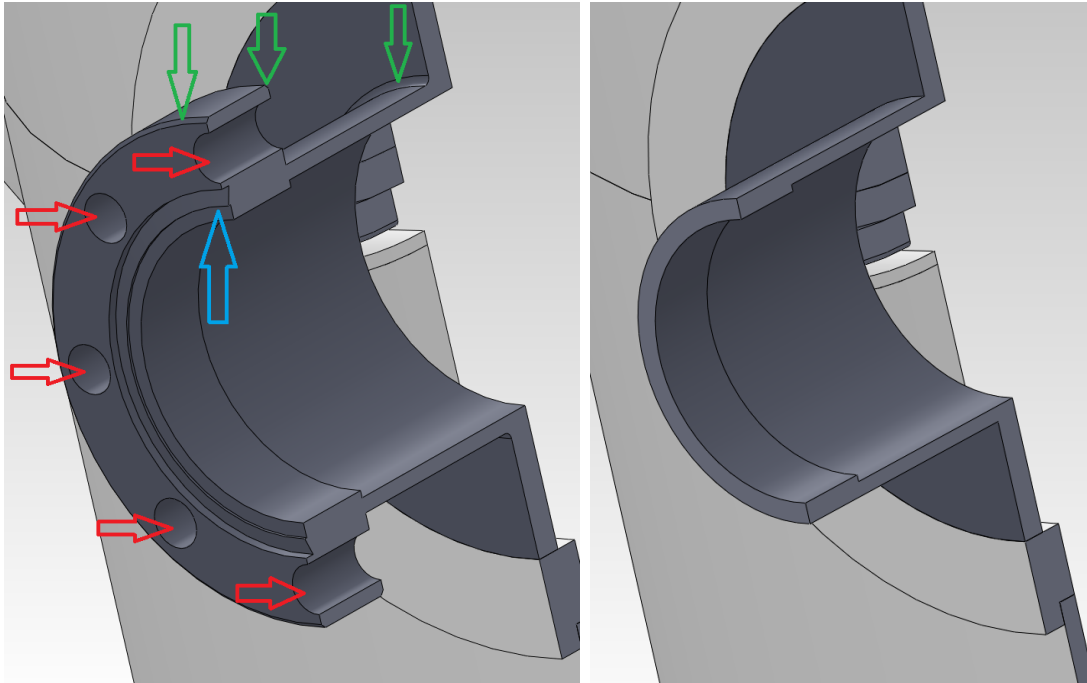


Figure 3.28: Left: Flange before simplification for simulation. Bolt holes are indicated by red arrows, fillets and chamfers by green arrows, and a complex feature (vacuum seal knife edge) is indicated by a blue arrow. Right: Simplified flange ready for inclusion in a simulation.

### 3.3.3 Accuracy Level

Because the mesh is kept during the mechanical simulation, the simulated frequency shift is extremely accurate. This is crucial because some of the effects being simulated only shift the frequency by tens to hundreds of hertz. As can be seen in Figure 3.29, these types of shifts can be accurately simulated to and below this level.

### 3.3.4 An Aside: Slater’s Theorem

Cavity perturbation analysis is an extremely powerful technique for cavity design and simulation. An analytical description of perturbations in resonant frequency due to perturbations

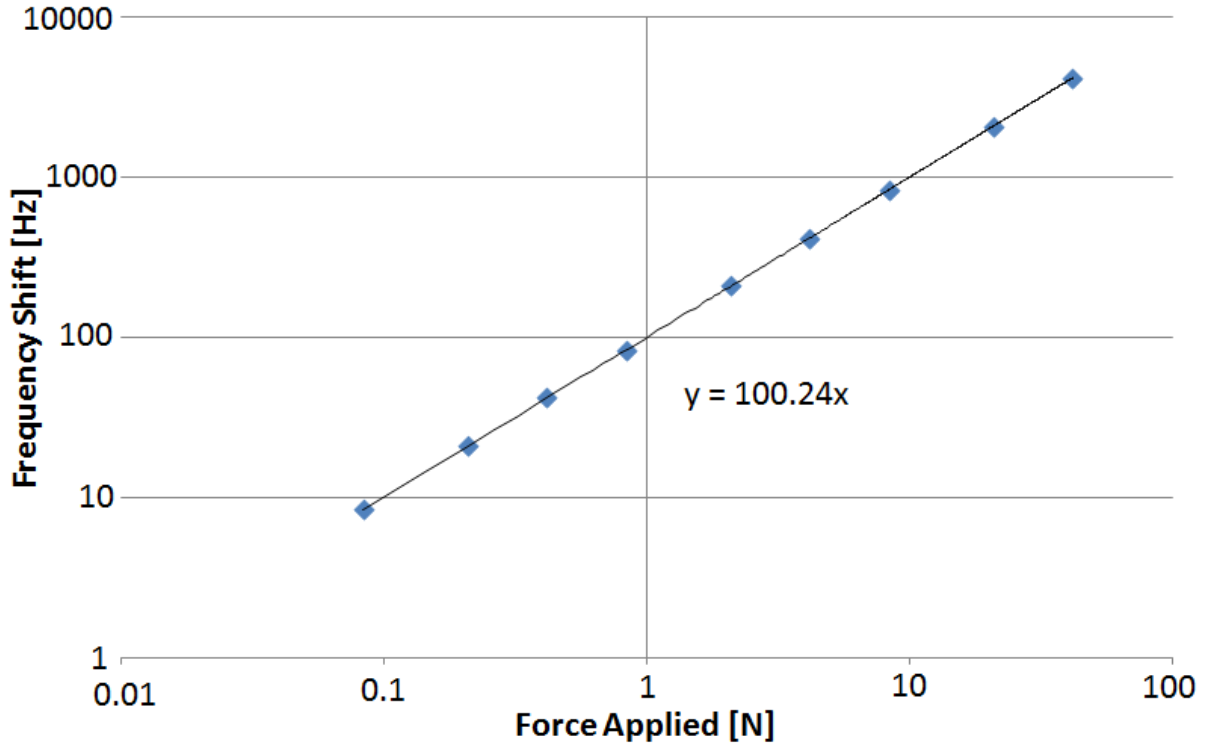


Figure 3.29: Frequency shift versus applied pressure for a mechanical simulation. Note the linearity down to very small frequency shifts.

in cavity geometry was first developed by Slater [43]. His description is built on classical resonator invariants which are constant under adiabatic changes to the resonator. This assumption is valid under almost all cavity design considerations where the time scale of the changes to be studied are at least five orders of magnitude longer than the RF period. For the classical harmonic oscillator, the stored energy at any time is given by

$$U = \frac{\omega^2 m x^2}{2} + \frac{p^2}{2m} \quad (3.17)$$

where  $p$  and  $x$  are canonical variables. This means that the area of the ellipse described by this equation is an adiabatic invariant. Modifying this equation into the standard form of

the ellipse

$$1 = \frac{x^2}{a^2} + \frac{p^2}{b^2} = \frac{x^2}{\frac{2U}{\omega^2 m}} + \frac{p^2}{2mU} \quad (3.18)$$

we find the area of the ellipse is

$$A = \pi ab = \frac{U}{f} \quad (3.19)$$

where  $f$  is the resonant frequency. Given that  $A$  is constant, we find that

$$dU = (A)df = \frac{Udf}{f}. \quad (3.20)$$

Using the known form of  $dU$  from Maxwell's Equations and assuming a finite (if small) change in volume ( $\Delta V$ ), we get Slater's Theorem:

$$\frac{\Delta f}{f_0} = \frac{\Delta U}{U} = \frac{1}{4U} \int_{\Delta V} (\epsilon_0 E^2 - \mu_0 H^2) dV. \quad (3.21)$$

### 3.3.5 Pressure Sensitivity

During operation, the cavity will have a pressure differential across its walls. This is because, while the vacuum space is at extremely low pressure, the helium space is at  $\sim 28$  torr (the pressure of 2 K liquid helium). This pressure differential deforms the cavity, shifting the cavity frequency. The deformation can be seen in Figure 3.30. As expected, the largest deformation occurs in the weakest places, the outer conductor between the RF and beam ports and the inner conductor just above the beam port. Immediately applying Slater's Theorem we can see that deformation in the electric field region will give an opposite contribution to the frequency shift to the shift from deformation in the magnetic field region. The LC circuit model of the cavity gives an intuitive reason for this scaling. In this model, the frequency of

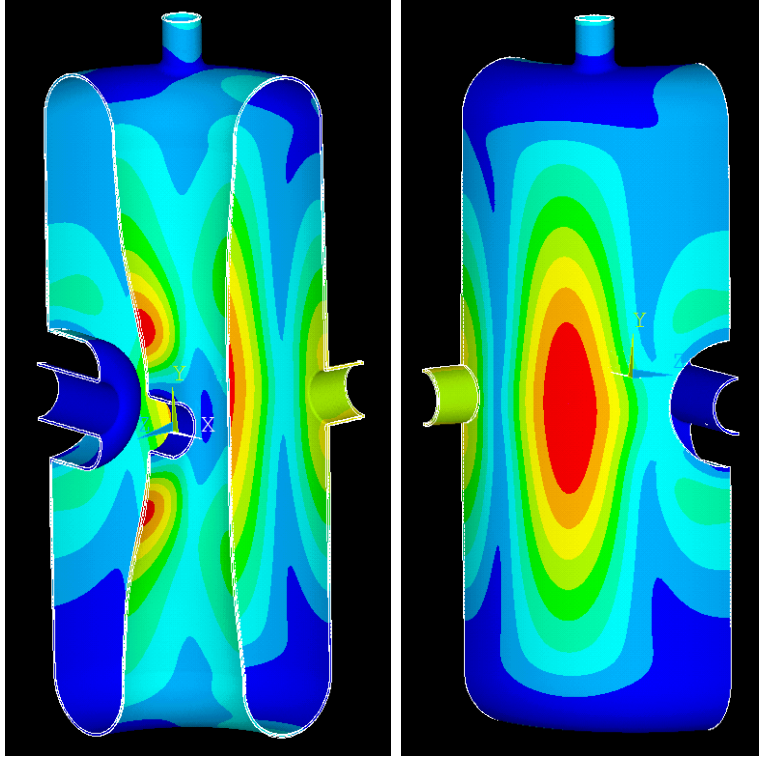


Figure 3.30: Left: Deformation of the inner conductor due to pressure differential. Right: Deformation of the outer conductor due to a pressure differential (5000 Pa).

the cavity is given by

$$\omega^2 = \frac{1}{LC} \quad (3.22)$$

where  $L$  is the inductance and  $C$  is the capacitance. Removing a small volume in the high magnetic field region will decrease the inductance, increasing the resonant frequency. Removing a small volume in the high electric field region will *increase* the capacitance, reducing the cavity frequency.

This behavior means that, if modification is necessary, stiffening can be used to balance these two contributions, resulting in a near-zero frequency shift coefficient. While a fixed frequency shift can be accounted for, the helium pressure can only be maintained to  $\sim \pm 1$  torr at a frequency of 1 Hz. This fast varying pressure must not vary the cavity frequency

too much, or controlling the cavity in operation becomes quite difficult. This is why the FRIB specifications require that the final coefficient  $|df/dP|$  be below 2 Hz/torr. The bare cavity gives a shift of  $-4.07$  Hz/torr. This agrees with what would be predicted by Slater's Theorem because most of the loss in volume ( $-dV$ ) is in the electric field region.

### 3.3.6 Lorentz Force Detuning

The fields in the cavity will interact with the induced charges and currents on the RF surfaces. The detuning from these forces is therefore called Lorentz Force Detuning (LFD) [44]. Again using Slater's Theorem, we find that

$$\frac{\Delta f}{f_0} = \frac{1}{4U} \int_{\Delta V} (\epsilon_0 E^2 - \mu_0 H^2) dV = -\frac{1}{U} \int_{\Delta V} (P) dV \quad (3.23)$$

where  $P$  is the LFD pressure. It is worth noting that the term  $(P)dV$  is always a positive quantity, a change in sign of the pressure  $P$  changes the direction of deformation, changing the sign of  $dV$ . This means that any contribution to this frequency shift will be negative. This means that the compensation techniques that could be used for correcting the pressure sensitivity do not apply here, so we must rely on straightforward stiffening of the cavity. The LFD frequency shift scales with the stored energy in the cavity, and therefore the field level squared. Thus, the LFD coefficient,  $K_L$ , is defined as

$$K_L = \frac{\Delta f}{(\Delta E_{acc})^2}; E_{acc} = \frac{V_{acc, \beta_{opt}}}{\beta_{opt} \lambda}. \quad (3.24)$$

This type of detuning is well modeled by the Duffing Equation, discussed in Chapter 2 along with the basic controls implications of this effect. Because the FRIB HWRs are to

be run with a duty factor of 1, this effect is not the dominant concern it can be for pulsed machines [45, 46], so the use of advanced compensation methods and control systems is not anticipated for FRIB. FRIB specifications do, however, call for  $|K_L|$  to be below 3 Hz/(MV/m)<sup>2</sup> for the HWRs. The bare cavity, as designed earlier, gives an initial  $K_L = -3.06$  Hz/(MV/m)<sup>2</sup>. The deformation resulting from this force can be seen in Figure 3.31.

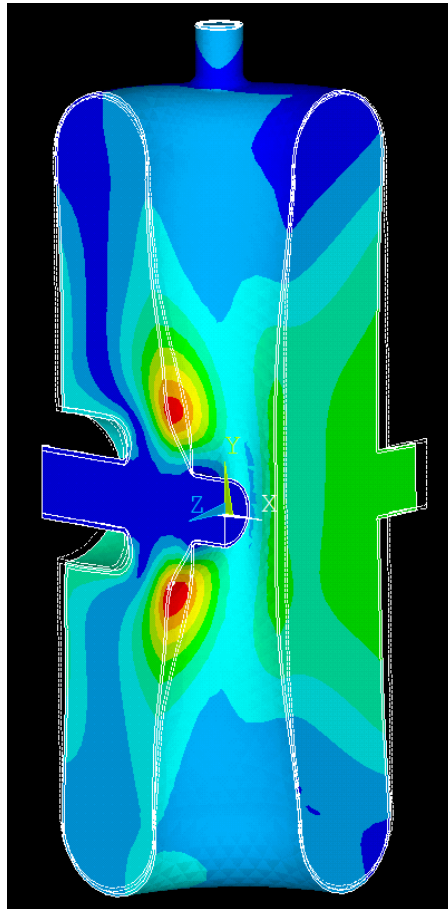


Figure 3.31: Deformation of the cavity with the Lorentz Force applied at full accelerating voltage.

### 3.3.7 Cavity Tuning

For the  $\beta = 0.29$  and  $0.53$  HWRs, it was decided to tune the cavity in operation by deforming the beam port cups by application of pressure on the beam ports themselves. The design of this tuner requires an estimate of the physical range and force required to give the FRIB specified tuning range of 150 kHz. For tuning measurements, all distances and forces given are for movement of *one* port while the frequency shift is for *both* ports moves symmetrically. Simulation of this effect is done by applying force to the beam port flange, and gives coefficients of  $df/dF = -126$  kHz/kN and  $df/dx = 599$  kHz/mm for full tuning range parameters of 150 kHz, 0.25 mm, and 1.185 kN. While this does provide a potentially large tuning range, the resolution of the tuner is also of great importance. For the controls, the desired frequency resolution of the tuner is 1 Hz, meaning that the tuner must have a resolution of  $\sim 2$  nm or  $\sim 8$  mN. It should be noted that this frequency sensitivity could have been estimated from the earlier beam port cup sensitivity study. This predicted a frequency sensitivity of 820 kHz/mm, and it is expected that a deformed, as opposed to fully moved, beam port cup would be slightly less sensitive. The deformation from the applied tuning pressure can be seen in Figure 3.32.

### 3.3.8 Cavity Stiffening

The mechanical figures of merit, especially the pressure sensitivity, could be improved by strategic stiffening of the cavity. The most mechanically weak part of the cavity is the beam port cups. The most simple method of increasing their stiffness would be to use a thicker sheet stock for their fabrication. A comparison between the electromechanical figures of merit for beam ports made with 2, 3, and 4 mm thick material can be seen in Table 3.10.



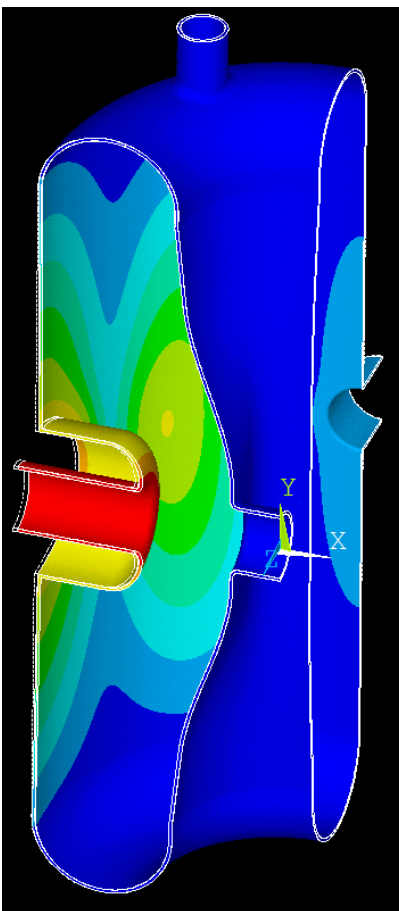


Figure 3.32: Simulation of cavity deformation for an applied tuning force.

As the thickness of the beam port cup increases, so does the stiffness. This decreases the

Table 3.10: Electromechanical Properties for different beam port cup thicknesses.

	$df/dF$	$df/dx$	$K_L$	$df/dP$
	kHz/kN	kHz/mm	Hz/(MV/m) <sup>2</sup>	Hz/torr
2 mm	-126	-599	-3.1	-4.1
3 mm	-96.2	-637	-2.2	-3.1
4 mm	-83.6	-656	-1.9	-3.8

deformation of the cup itself, and improves the electromechanical figures of merit. However, at 4 mm, the cup becomes so stiff that the movement of the surrounding, unstiffened, cavity walls increases, increasing  $df/dP$ . This leads to the decision to use 3 mm material for the beam port cup instead of the stiffer 4 mm material. Some other stiffening must be

done, however, and the most logical location is the inner conductor. The least complex stiffening is to add a thin metal ring to the inner conductor, seen in Figure 3.33. This will be relatively straight-forward to manufacture and install, and the positioning allows the desired optimization. The main figure of merit being optimized with this is the pressure sensitivity.

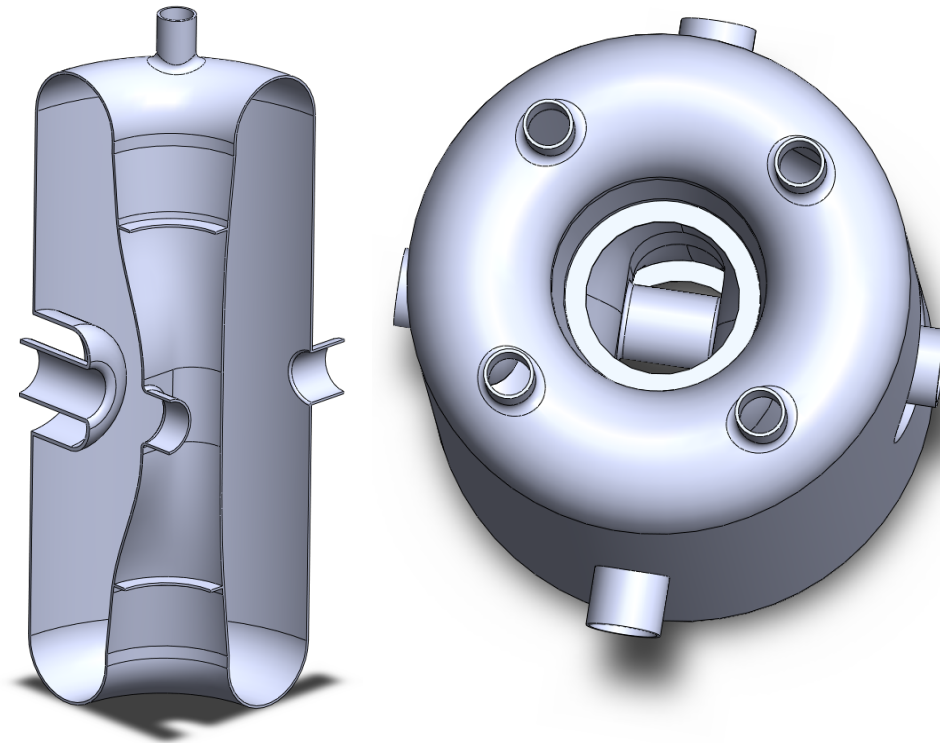


Figure 3.33: Left: Stiffening ring added to the inner conductor in section view. Right: Top down view of the stiffening ring with full cavity.

The tuning figures of merit should be essentially unaffected by the addition of the stiffening ring, and the Lorentz Force Detuning should improve with the addition of any stiffening. With this stiffening ring placed  $\pm 145$  mm from the median plane of the cavity, the pressure sensitivity and LFD coefficients improve even more, giving us a final set of optimized figures of merit, seen in Table 3.11. While further stiffening of the beam port cup may be required for the tuning resolution, the ring position could be reoptimized to provide adequate pressure sensitivity and Lorentz Force Detuning.

Table 3.11: Optimized Electromechanical Properties.

$df/dF$	$df/dx$	$K_L$	$df/dP$
kHz/kN	kHz/mm	Hz/(MV/m) <sup>2</sup>	Hz/torr
-96.6	-637	-1.73	-0.98

# Chapter 4

## Prototyping and Testing of Advanced Half Wave Resonators at Michigan State University

In this chapter, we will discuss the fabrication, assembly, and testing of advanced Half Wave Resonator designs at Michigan State University. First, the process chosen for fabrication of HWRs at MSU will be detailed in the context of the cavity designed in the previous chapter. Next, the mathematical formalisms used for cavity testing will be presented as well as the process of interpreting testing data. Data from an HWR test will then be described and results presented with comments about common issues encountered during testing. The cavity tested was a prototype HWR with  $\beta = 0.53$ , the design of which can be seen in Figure 4.1.

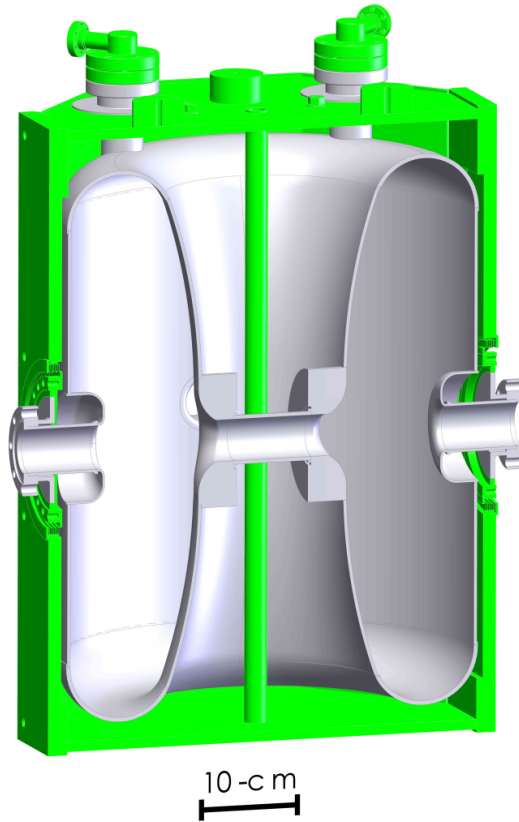


Figure 4.1: Prototype  $\beta = 0.53$  HWR manufactured and tested at MSU with helium vessel.

## 4.1 Cavity Fabrication and Processing

In this section, I will discuss the process of fabricating an HWR. This includes material selection, subassembly fabrication, cavity welding, cavity tuning, and preparation for testing. For a broader discussion and description of the state of the art for cavity processing and fabrication (mostly directed toward the International Linear Collider (ILC)), the reader is directed to either of H. Padamsee’s books “RF Superconductivity for Accelerators” [7] or “RF Superconductivity” [41], or for more recent developments, to the proceedings of the SRF conferences [42].

### 4.1.1 Material Selection through Subassembly Fabrication

For most HWR designs, the cavity itself is formed from high purity ( $RRR < 300$ ) niobium sheet. This comes in either 2 or 3 mm thickness, and is either rolled or stamped to form the various subassemblies. The inner conductor is formed from two pieces, each formed to the appropriate shape. The drift tube fillet is then coined in the appropriate place, and the two halves of the inner conductor are welded together with the drift tube. All welding must be done in a manner that preserves the high purity of the niobium. It also must be done in a non-oxygen environment to prevent oxidation of the niobium around the weld. This means that all cavity welds are done with an electron beam in a vacuum. Additionally, subassemblies are cleaned, degreased, and lightly etched before welding to improve weld quality. The various stages of IC preparation can be seen in Figure 4.2.

The outer conductor is rolled from sheet niobium and seam welded into a straight cylinder of the appropriate height. The short plates are also formed from sheet niobium, with one having the holes for the rinse ports cut in it. The rinse ports must be machined out of a billet of niobium. A Computer Numerical Control (CNC) milling machine is needed to achieve the proper curvature. Then the rinse ports are welded into one of the formed short plates. These subassemblies can be seen in Figure 4.3.

This is an appropriate time to check the tolerances of the subassemblies. By stacking the short plates, inner conductor, and outer conductor, gaps can be found between the parts depending on the errors in trimming of these parts. Because the inner conductor was designed with a short straight section at the place where it meets the short plate, the parts can be trimmed such that the subassemblies stack with little or no gap. This significantly eases welding tolerances by reducing the force needed to hold the weld joints together and

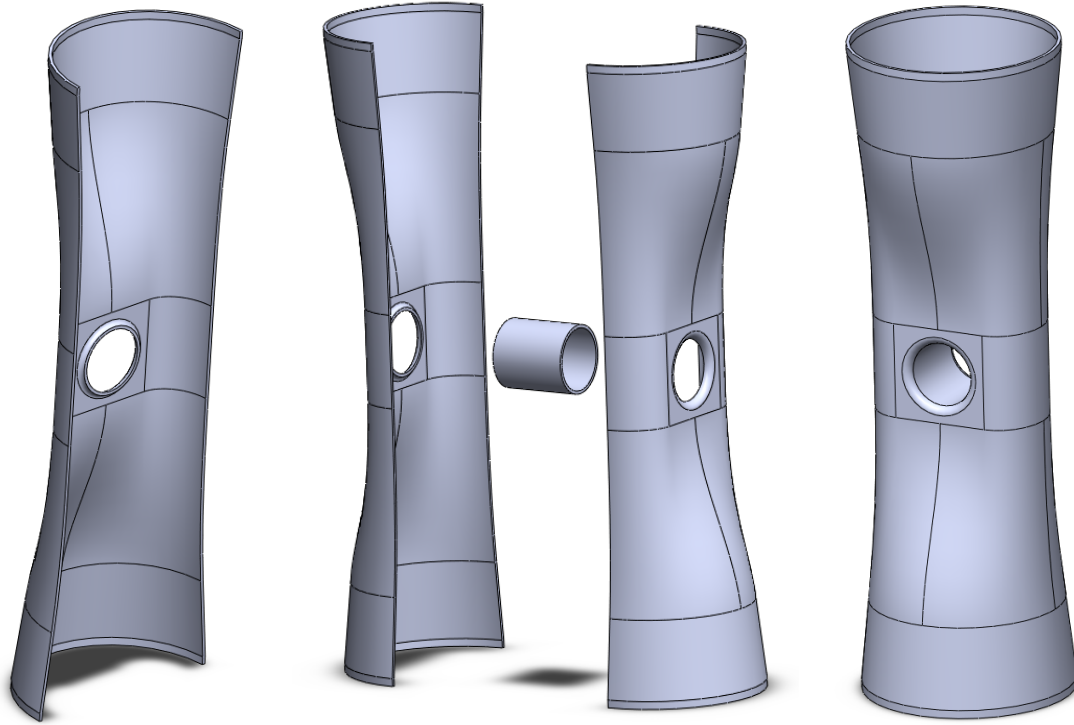


Figure 4.2: Left: Half of an inner conductor after forming with coined drift tube fillet. Middle: Two inner conductor halves ready to be welded to a drift tube. Right: Fully fabricated inner conductor.

should produce more repeatable and higher quality welds. Holes are then cut on the outer conductor's midplane for the beam port cups and RF ports, and the RF ports are welded into place. At this point, the subassemblies are combined into two major pieces, which can be seen in Figure 4.4.

This step involves the first challenging weld of fabrication. Ideally, all welds would be made from the RF side because this does not require the weld to penetrate through the full thickness of the material. The quality of these welds is generally higher because of the control this method allows. To weld the outer conductor to a short plate, the weld must be done from the outside, penetrating all the way through the material in what is called a "full penetration" weld. While all electron beam welding is challenging, this type of weld requires

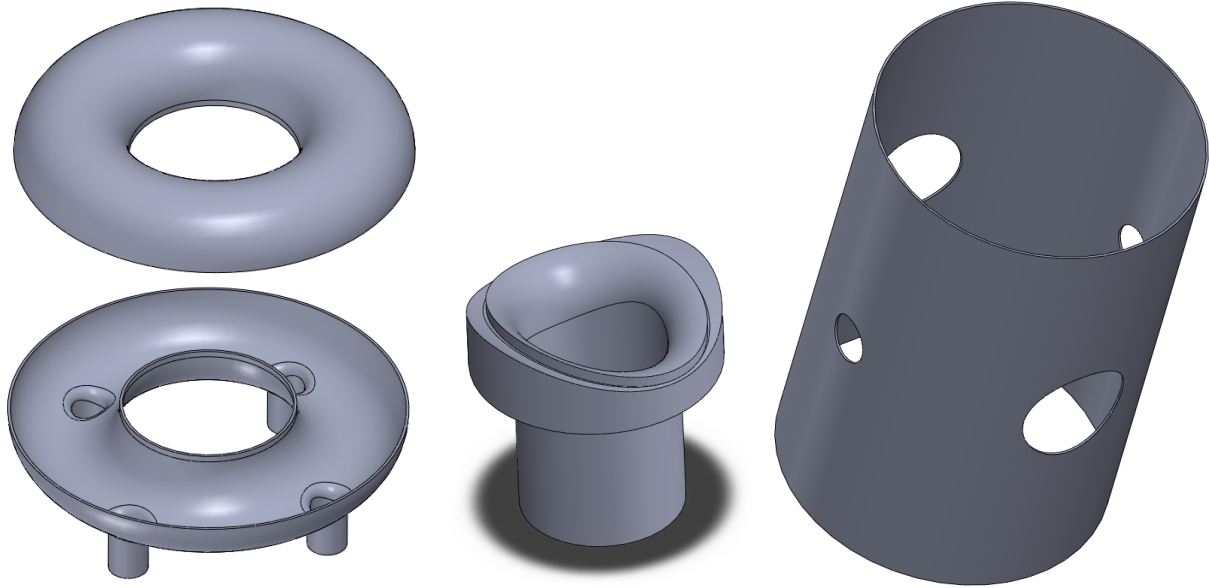


Figure 4.3: Left: Completed short plate subassemblies, with and without rinse ports. Middle: Rinse port milled from a niobium billet, ready to be welded to the short plate. Right: Fully fabricated outer conductor.

experience to perform reliably. When the two large subassemblies are combined to form the bulk of the cavity, it also requires two more full penetration welds. The most dangerous is the weld of the inner conductor to the second short plate, because this is the only weld in a high field region that is required to be full penetration. The final parts of the cavity to be welded are the beam port cups. The cup is formed in one piece with the beam tube welded inside. These are positioned to achieve the desired frequency, although ideally this position would also be the designed position. This weld step can be seen in Figure 4.5.

After welding, all parts are “degassed” at  $800^{\circ}\text{C}$  to drive out hydrogen and prevent Q-Disease (discussed in a later section). The interior of the cavity is also etched using a Buffered Chemical Polishing (BCP) acid blend. This etch, which can be up to  $150\ \mu\text{m}$ , removes the mechanically damaged layer of material from the RF surface of the cavity, improving cavity performance [47]. The cavity is then rinsed with high pressure jets of



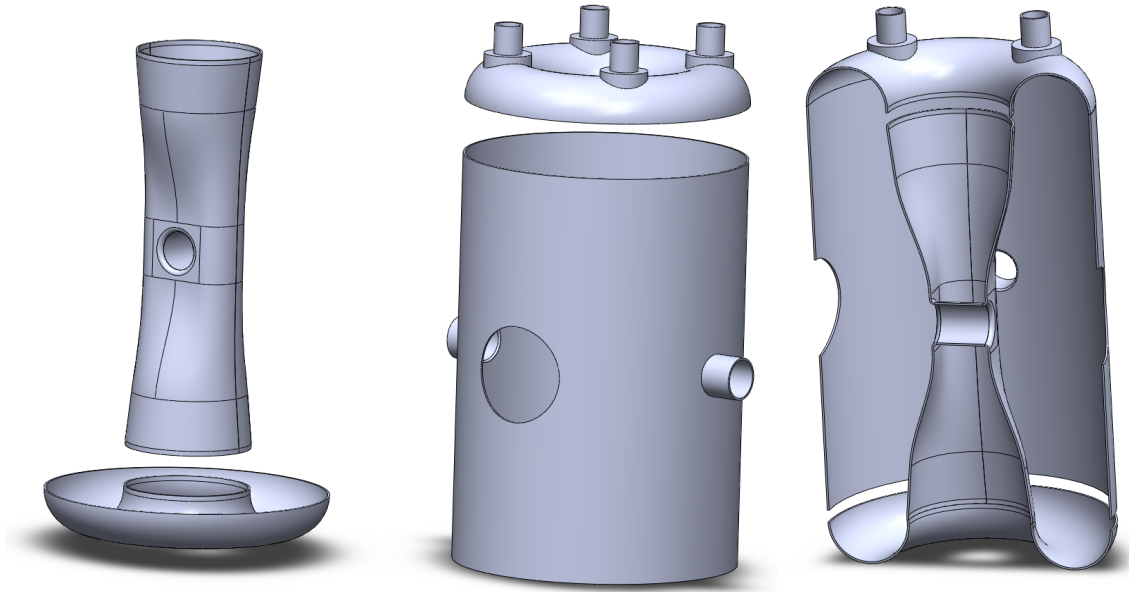


Figure 4.4: Left: The inner conductor is welded to a short plate. Middle: The outer conductor with RF ports is welded to the opposite short plate. Right: The final two large subassemblies ready to be welded together.

ultra-pure water to remove particulate from the surface that could cause field emission. The now clean and prepared cavity is dried and assembled in a clean room (Class 10-100) to ensure the integrity of the clean RF surfaces. Finally, the cavity is baked at  $120^{\circ}\text{C}$  to improve high field performance.

## 4.2 Cavity Testing Theory and Setup

A critical part of cavity design is feedback from prototyping and testing of realistic cavities. This is because cavity performance is a combination of RF design, material selection and handling, fabrication technique, cavity processing, and other, more subtle effects. There are many steps in the fabrication process that must be taken into account in the design process that can only be quantified on a real cavity, such as weld shrinkage, coupling strengths, superconducting surface resistance (and therefore quality of cavity processing), and many

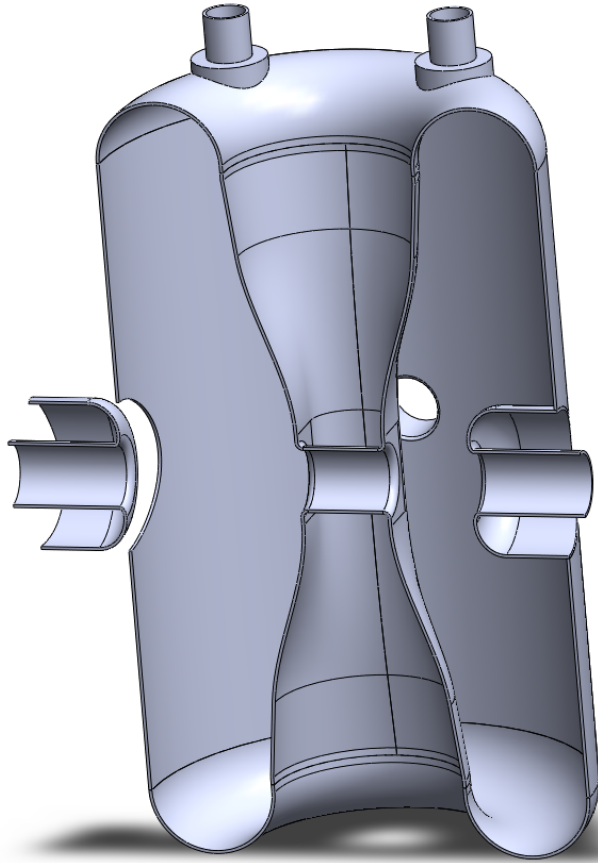


Figure 4.5: The beam port cups are positioned to achieve the final frequency. The cup on the right is in the ideal (design) position.

others. Cavity testing measures the cumulative effect of all of these factors. In this section, the theory and setup of a cavity test will be discussed. Additionally the data measured during a specific HWR test will be examined along with the details of translating this data into relevant cavity parameters.

#### 4.2.1 Testing Theory

The basic theory of a cavity test centers around measuring the quality factor of the cavity at a variety of stored energies. While the cavity is designed to optimize many figures of merit, most of them cannot be directly measured during a cavity test. These include peak surface

fields,  $R/Q$ ,  $\beta_{opt}$ , and the Geometry Factor, which must be inferred using simulation data. A cavity test is performed with two power couplers, one close to matched to minimize the required forward power (“input” coupler) and one very weakly coupled (“pickup” coupler). Power is coupled to the cavity with the input coupler, while the pickup coupler is used strictly as a diagnostic tool. Cavity tests are done with a phase lock loop matching the driving frequency to the cavity resonance. The basic testing phase lock loop arrangement can be seen in Figures 4.13 and 4.14.

This RF circuit allows a signal generator to track the cavity resonant frequency by mixing the transmitted power signal with the forward power signal, giving a DC signal whose amplitude is based on the difference between the driving frequency and the cavity resonant frequency. With the cavity driven in steady-state on resonance, only the cavity frequency ( $f$ ), forward power ( $P_f$ ), reverse power ( $P_r$ , vector sum of the reflected and emitted traveling waves from the input coupler), and the transmitted power ( $P_t$ , from the pickup coupler) can be measured. Using equations from Chapter 2

$$|S_{11}|^2 = \frac{P_r}{P_f} \quad (4.1)$$

$$|S_{21}|^2 = \frac{P_t}{P_f} \quad (4.2)$$

$$\beta_2 = \frac{|S_{21}|^2}{1 - |S_{11}|^2 - |S_{21}|^2} = \frac{Q_0}{Q_{ext,2}} = \frac{P_t}{P_d} \quad (4.3)$$

$$\beta_1 = \frac{1 \pm |S_{11}|}{1 \mp |S_{11}|} = \frac{Q_0}{Q_{ext,1}} = \frac{P_r}{P_d} \quad (4.4)$$

and

$$Q_0 = Q_L(1 + \beta_1 + \beta_2) \quad (4.5)$$

we see that we don't have enough information to calculate  $Q_0$  and  $U$ . To do this, we must determine the  $Q_L$  and the coupling (whether  $\beta_1$  is greater or less than 1). Both of these can be obtained from modulating the forward power. The most straightforward method is to suddenly shut off the forward power, so that the equation for the stored energy in the cavity becomes

$$\frac{dU}{dt} = -P_L = -\frac{\omega U}{Q_L} \quad (4.6)$$

which gives

$$U(t) = U_0 \exp\left(-\frac{\omega t}{Q_L}\right). \quad (4.7)$$

For a sufficiently large  $Q_L$  (true for most Dewar tests), a decay time  $\tau_L$  can be measured for

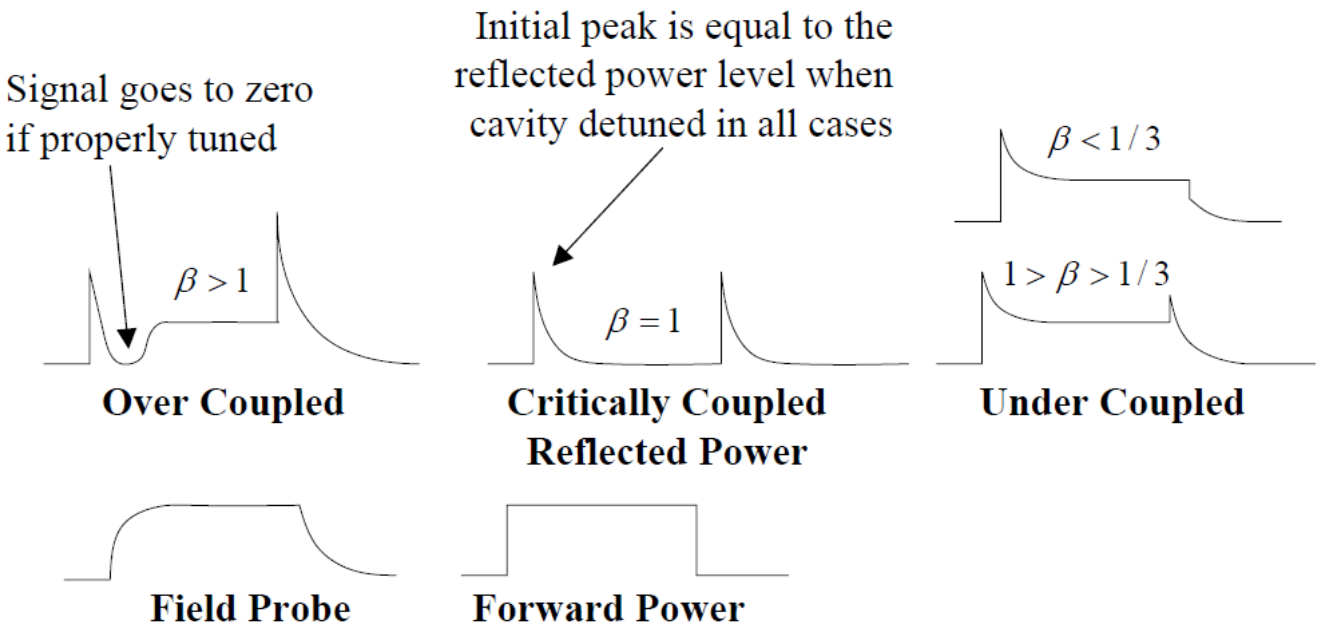


Figure 4.6: Transient behavior of the reverse power for different coupling strengths. All curves are in response to the shown forward power behavior. Image credit to Tom Powers, TJNAF.

a given  $U/U_0$  (usually about a  $-6$  dB fall), giving  $Q_L$ . Additionally, the transitory response of  $P_r$  determines whether the cavity is over or under coupled. This effect can be seen in

Figure 4.6. In this way, we have enough information to calculate not only  $\beta_1$  and  $\beta_2$ , but also  $Q_0$ . Given this, we can calculate  $Q_{ext,2}$ , allowing us to transform our measurement of  $P_t$  into a measurement of  $U$ . While it is often assumed that  $Q_{ext,1}$  and  $Q_{ext,2}$  do not change dramatically over the course of a Dewar test, it is recommended to periodically repeat the modulated measurements to ensure these values have not drifted during testing. With knowledge of  $Q_{ext,2}$ , every set of power measurements can be used to directly calculate  $Q_0$  and  $U$ :

$$P_d = P_f - P_r - P_t; \quad U = \frac{Q_{ext,2}}{\omega} P_t \quad (4.8)$$

where the first equation is the cavity energy balance, and

$$Q_0 = \frac{\omega U}{P_d}. \quad (4.9)$$

This method, known as the “direct” method, has the disadvantage of using  $P_r$  extensively. Especially far from unity coupling,  $P_f - P_r$  is likely to be quite small, and error prone. Fortunately, there is another method for calculating  $Q_0$  and  $U$ . While the first method does not require the use of  $Q_{ext,1}$ , this method uses this previously measured number in place of  $P_r$ . This method is known as the “indirect” method, because, while measuring  $Q_{ext,1}$  involves  $P_r$ , this usage makes it less sensitive to the uncertainty of its measurement. Plugging the definition of  $Q_{ext,1}$  into our equations, and making the usual assumption that  $\beta_2 \ll 1$ , we find that

$$Q_0 \approx \frac{Q_{ext,1}}{2\sqrt{\frac{Q_{ext,1}}{Q_{ext,2}} \cdot \frac{P_f}{P_t} - 1}}. \quad (4.10)$$

It should be noted that once  $Q_{ext,2}$  and  $Q_{ext,1}$  are calculated with modulated measure-

ments, they are assumed to be constant for following measurements. This, however, makes each CW measurement over-specified, and this can be used to check the measurement's accuracy. In principle, both the direct and indirect methods should give the same answer.

Starting from

$$\frac{Q_{ext,2}}{Q_{ext,1}} = \frac{\beta_1}{\beta_2}. \quad (4.11)$$

it is straight-forward to derive (assuming, as usual, that  $P_t$  is small compared to  $P_f$ )

$$\sqrt{\frac{Q_{ext,2}}{Q_{ext,1}}} |S_{21}| = 1 \pm |S_{11}|. \quad (4.12)$$

Plotting the left side of this equation versus the right side of the equation using the data ( $|S_{21}|$  and  $|S_{11}|$ ) and the assumed values for  $Q_{ext,2}$  and  $Q_{ext,1}$  gives an easy graphical method of checking the consistency of the measured values. Depending on the coupling,  $|S_{11}|$  will vary from 1 to  $-1$ , so the plotted data should, ideally, lay on a simple triangle. Thus, the plot of these quantities is an excellent way to test whether the values of  $Q_{ext,1}$ ,  $Q_{ext,2}$ ,  $P_r$ ,  $P_f$ , and  $P_t$  are consistent. Any systematic deviation between the plotted data and this “Duality Triangle” indicates a problem with the data. This generally happens when the assumption of constant coupling is invalid, which is the case for the test presented in Section 4.4, a dramatic shift in coupling between test day 1 and test day 2 had to be accounted for.

### 4.2.2 Measurement Procedure

For a given cavity configuration, there are generally two phases to measuring the cavity's parameters. The first consists of the modulated measurements required to calibrate the CW

measurement, and this is generally done at low field levels to avoid dynamic behavior that can occur at higher fields. After the field level is set, generally around  $E_{pk} \sim 1$  MV/m, the phase of the transmitted power signal going to the mixer is adjusted to maximize  $P_t$ . This is important because, while there is a phase shift from driving the cavity off resonance, there is also a phase shift from the cable and devices used to do the measurement. Having a mechanism for shifting this phase (physical or electronic) is crucial not only for compensating the overall phase difference between  $P_t$  and the signal sampled from  $P_f$  (modulo  $2\pi$ ), but also for fine-tuning before every measurement. This is because the phase of the circuit can (and will) drift during the course of the cavity test because of thermal or mechanical changes in the components and transmission lines. For a perfectly adjusted circuit, the cavity is driven directly on resonance, maximizing  $U$  and therefore  $P_t$  for a given  $P_f$ . Having properly adjusted the phase, the forward power is shut off, and the dissipated power is plotted versus time, generally on a spectrum analyser. The decay time is recorded for a given power difference (generally  $-6$  dB), and the initial  $P_t$  is recorded. It is important to accurately correlate this measurement with a set of CW measurements taken immediately after the modulated measurement. Combining these modulated and CW measurements allows the calculation of  $Q_{ext,1}$  and  $Q_{ext,2}$  as detailed in the previous subsection, and these are used to interpret the following CW measurements.

The second phase of measurement is to perform CW measurements at different  $P_f$ . The forward power is increased in steps of  $1 - 3$  dB, and several CW data points are recorded at every step, after adjusting the phase shift. The higher the cavity fields, the smaller the steps in  $P_f$  should be, to get the best resolution in this region. This is because the most dynamic behavior happens here, and sudden shifts in  $Q_0$  can occur. This is generally continued

until limited either by cavity quench, maximum available  $P_f$ , or high radiation levels from field emission. It should be noted that many values are recorded with each data point, not just power levels. This includes data such as date and time, readings from temperature and pressure sensors, liquid helium level, and more. Any interesting phenomena are then investigated, time permitting, such as the detailed behavior of sudden drops in  $Q_0$ , field emission onset levels, quench field level, etc. If desired, time can be spent conditioning the cavity at high fields in an attempt to improve performance. This is most generally done when there is high radiation levels in an attempt to destroy or otherwise shut off the serious field emission sites causing the radiation. In cases of high radiation, staying at high power or pulsing to even higher power can be successful in improving performance, allowing access to higher field levels. Once all of the desired data are collected for a given cavity configuration, then the configuration is changed and the process is repeated. The nature of the cavity configurations depends strongly on the exact phenomenon being studied, but a common example of this would be measurement at different temperatures as the cavity is pumped down to 2 K.

### 4.2.3 Calibration of the RF Network

It is important to remember that the RF circuit has losses at almost every point. This means that the powers measured by the power meters (Cal Points E, F, and G, seen in Figure 4.7) have additional losses in them from the RF circuit compared to the values we need to calculate the cavity parameters. These power values would, ideally, be recorded at the cavity (Cal Points B and C). Calibrating the RF circuit is the process of measuring the effective losses between these locations. Calibration measurements are all done using a Vector



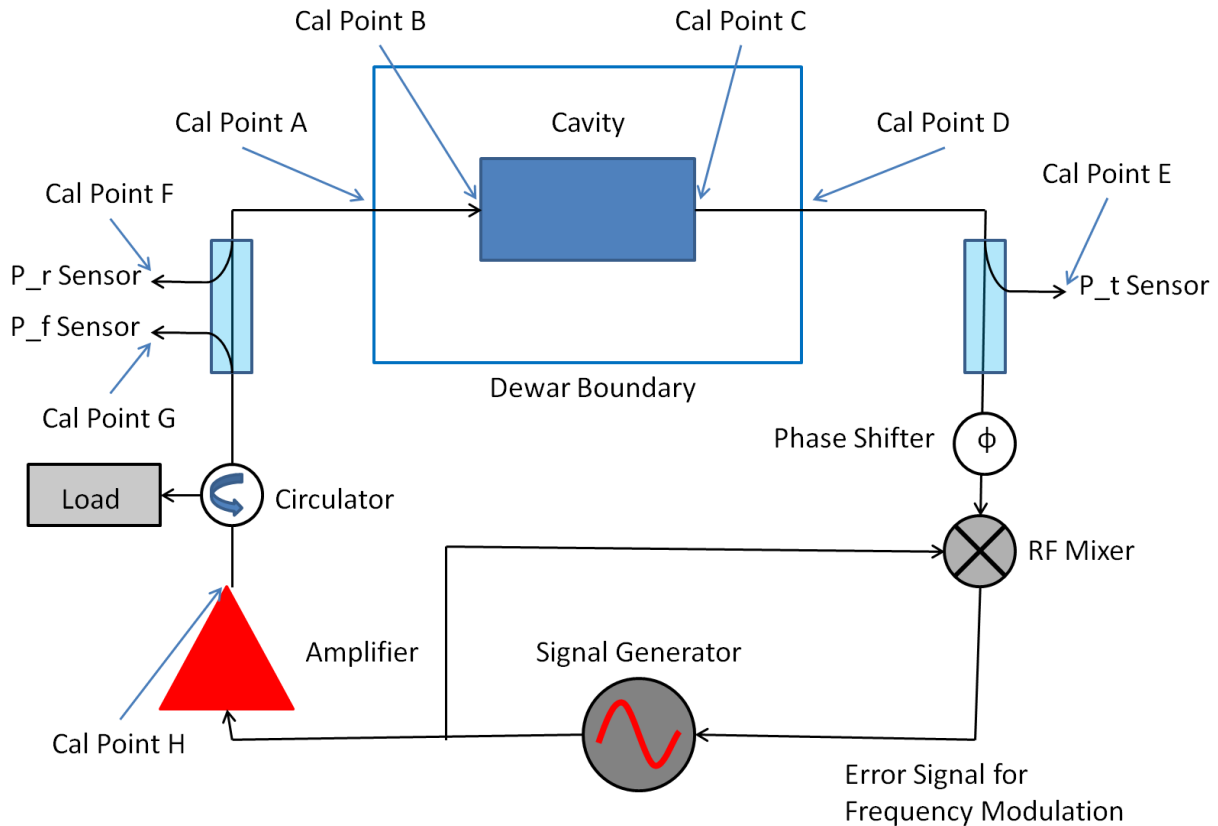


Figure 4.7: Basic RF circuit for a phase lock loop for cavity testing with the calibration points marked.

Network Analyzer (VNA), carefully calibrating the measurement equipment at each step. All measurements are done at four frequencies: the design frequency, the design frequency  $\pm 0.5$  MHz, and the cavity frequency as measured during the cavity test. It should also be noted that all losses should be measured in decibels, this allows direct addition of losses in series. This allows interpolation of the calibration for the test data as required. This calibration takes place in two phases for logistical reasons. While all parts of the RF circuit outside the Dewar are room temperature and can be considered relatively stable if left in place, the transmission lines and connections inside the Dewar must be calibrated while the cavity is cold because of the significant thermal shifts. This is generally measured directly

after the completion of a cavity test, while the circuit is as thermally stable as possible. This is done by connecting Cal Point A to Port 1 of a VNA through a calibrated cable, then measuring the round-trip losses ( $S_{11}$ ), repeating for Cal Point D. These values are called the “Cold Calibration”. The rest of the process is called the “Warm Calibration” because it involves measurement of the rest of the RF circuit, which is at room temperature. The first step for this is calibration of the  $P_t$  and  $P_r$  power sensors. Because we have already measured the losses inside the Dewar, all that remains is measuring the losses from Cal Point D to Cal Point E for  $P_t$  and from Cal Point A to Cal Point F for  $P_r$ . These losses will include the cable losses as well as the attenuation from the directional couplers used to sample these signals. This measurement is done by connecting the Dewar end to Port 1 of the VNA and the power sensor end to Port 2 of the VNA, and measuring the losses (S21). The final calibration for these power sensors is the warm losses plus *half* of the appropriate round-trip cold losses. The most complex calibration is for  $P_f$ . This is because what we desire is the forward power at Cal Point B (again, what the cavity actually sees) as measured at Cal Point G for a given power at Cal Point H (right out of the amplifier). The first step accounts for the losses from the amplifier to the cavity by connecting Cal Point H to Port 1 of the VNA and Cal Port A to Port 2 of the VNA, then *calibrating out* the through losses. Port 2 of the VNA is then moved *without changing the calibration* to Cal Point G while terminating Cal Point A with a  $50\ \Omega$  load, where the power loss (S21) is measured. The power measured, though, is the forward power at Cal Point A seen at Cal Point G. This means that, for the final calibration of  $P_f$ , the warm calibration number must have half the appropriate cold calibration *subtracted* to properly reflect the forward power at the cavity.

## 4.3 Challenges for Cavities in Testing and Operation

There are many practical concerns to take into account when designing a cavity besides the standard figures of merit. Based on the geometry, it is possible (almost impossible to suppress entirely, in practice) to have stable resonant trajectories for stray electrons in the cavity (themselves almost impossible to suppress). This behavior can severely complicate machine operation and even limit achievable field and quality factor. Beyond this, processing and fabrication are imperfect processes, and can introduce their own operational complications. This section will discuss these more common challenges that are often encountered while testing or operating a cavity and their mitigation.

### 4.3.1 Multipacting

The name multipacting is a compound word used to shorten “multiple impacting”, and this name is a good description of this phenomenon. Stray electrons in the cavity vacuum space interact with the cavity fields and strike the cavity walls. The impact can generate more electrons emitted from the surface, which will also have some trajectory based on their energy, angle of emission, and RF phase. The number of electrons emitted is quantified by the Secondary Emission Yield (SEY), which depends on many factors including electron energy, surface preparation, and impact angle. The electron’s trajectory also extracts energy from the cavity, depositing it into the cavity walls. Based on the surface it strikes, the energy of impact, and the angle of impact, the average number of ejected electrons varies, and can be over 1.4 [49], even in a well processed cavity. The energy this cascade extracts is trivial, in principle, until it is sustained for many generations. If the trajectories of the electrons becomes closed, i.e. return to near the original emission point (and RF phase), the cascade

continues, eventually consuming all additional RF power injected into the cavity.

### 4.3.2 Avoiding Multipacting Before Testing/Operation

There are multipacting considerations both in design and operation. In the design, care must be taken not to introduce the conditions for strong multipacting, mostly characterized by regions of parallel surfaces, especially items like couplers, plungers, and stub tuners. The strongest multipacting occurs when there is a wide range of trajectories in location, energy, and RF phase that satisfy the resonant condition. These barriers are called “hard” barriers because they are extremely difficult to get beyond in testing/operation. Particle tracking simulations [49, 50] for predicting multipacting have been increasing in accuracy in recent years, and have become reliable for predicting and avoiding strong multipacting barriers in cavity designs. However, because of the perfection of the models used, these simulations often find far more barriers than will present themselves in practice. Fabrication errors are often beneficial, in this case. The random errors added to the surface often break the resonant condition for the weaker multipacting bands, although this is not a strong enough benefit to loosen manufacturing tolerances. Additionally, careful surface preparation during cavity fabrication and processing can reduce the SEY, automatically narrowing multipacting bands. For HWRs of this geometrical type, multipacting studies have been done [49] and found no significant barriers (besides the rinse port plungers, which were later removed from the design). This has been born out in testing where no significant multipacting has been encountered.

### **4.3.3 Dealing with Multipacting During Testing/Operation**

Once encountered in operation, there are two common strategies to overcome this limitation. The first involves rapidly adjusting the RF phase, frequency, or forward power to try to “jump” past the barrier. Because multipacting is a resonant behavior, perturbations to the conditions in the cavity can disturb the electron cascade long enough for the cavity to be brought to a higher power, ending the resonant condition. This is easier in operation than in testing because the much higher coupling available means that the cavity field can be ramped much more rapidly. It is uncommon to have significant multipacting barriers at high fields, so this method will often allow testing of the cavity high field behavior. Care must be taken to not reduce the cavity fields below the barrier, or risk becoming trapped in the barrier again. The second strategy for multipacting is reducing the local SEY. This is achieved by allowing the multipacting barrier to condition itself. The electron bombardment will cause gasses to desorb from the surface, generally decreasing the strength of the multipacting band. While this process has obvious limits, strong barriers encountered at the beginning of testing can be significantly weakened to allow testing to proceed. Any venting of the cavity or further processing includes the danger of reintroducing these barriers.

### **4.3.4 Field Emission**

Field emission is caused by a stray electron in the cavity gaining energy from the cavity fields and impacting the cavity wall with enough energy to generate an X-Ray instead of more electrons. Because this is not a resonant behavior, it requires a different source of electrons, usually particulate (“field emitters”) on the cavity surface not removed by processing. These field emitters locally enhance the electric field, causing a stream of electrons to flow into the

cavity at high fields. Because of this behavior, field emission is a problem at high fields, unlike multipacting. At low fields, the fields on the emitters aren't enough to generate large numbers of electrons, and they don't gain enough energy from their trajectory to generate significant numbers of X-Rays. As the fields in the cavity increase, both the number of electrons and the energy they gain increase until cavity performance begins to suffer. The energy extracted by the electrons during their transit can significantly reduce the cavity quality factor, and can limit achievable fields by requiring more RF power, both from extracted energy and increased coupler mismatch to the cavity. If the field emission is strong enough, the energy deposited by the electrons on the cavity wall can be enough to cause a local thermal quench. Once the superconductivity is broken locally, the cavity stored energy is rapidly dissipated there, turning the field emission off. Field in the cavity can be restored once the wall has cooled and become superconducting again. There are several common ways of mitigating this problem. During processing, high-pressure rinsing with ultra-pure water forceably removes larger particulate from the surface, significantly reducing the sources for electrons at high fields, while clean room preparation and assembly reduces reintroduction of these particulate after cleaning. During operation, the field emitters can be used to process themselves. By operating close to the limit of operation (limited by available power or radiation limits), often pulsing to higher fields as well, enough power can sometimes be introduced to strong emitters to cause their destruction. This process works best for small numbers of strong emitters, and has obvious limits. While strong emitters can be suppressed by careful fabrication, processing, and testing, stray electrons can never be eliminated from the cavity. With a non-zero population of electrons in the cavity from things such as residual gas, cosmic rays, and weak field emitters, it is common to see minor field emission at very high fields. Care

must be taken during design of testing facilities to include adequate radiation shielding to allow testing of even the worst cavities.

### 4.3.5 Q-Disease

Hydrogen is introduced into the cavity material at many points along the cavity processing. The strongest source is etching, especially if the temperature of the acid blend used isn't well controlled. The hydrogen itself is not thought to degrade cavity performance. However, between 40 K and 120 K [51], niobium reacts with hydrogen to form several kinds of hydrides on the surface of the cavity. These hydrides are dielectric, and extremely lossy. In operation, the quality factor of the cavity is severely reduced, and degrades further as the field is increased. The formation process of these hydrides is relatively slow; if the dangerous temperature region is passed through in under an hour [51], little to no degradation is seen. This results in interesting requirements for the design of cryomodule cryogenic systems, a balance between efficient use of cryogenics and rapid cooling of the cavities through the dangerous temperature region. Additionally, a degassing bake can be used to drive off the hydrogen from the material, significantly reducing the danger of Q-Disease. This bake is generally done at 600°C for roughly 10 hours in high vacuum. Once observed in testing or operation, there is no known remedy for Q-Disease besides a warming to 200 K and more rapid cooling cycle.

## 4.4 The Testing of a Prototype $\beta = 0.53$ HWR

On October 11th and 12th of 2011, a cavity test was performed on a prototype  $\beta = 0.53$  HWR. This section will describe the goals and results of this test along with the challenges

encountered, as well as implications of this and other tests on HWR design and fabrication.

#### 4.4.1 Cavity Description

The cavity that was tested can be seen in Figure 4.8. This is an earlier cavity design

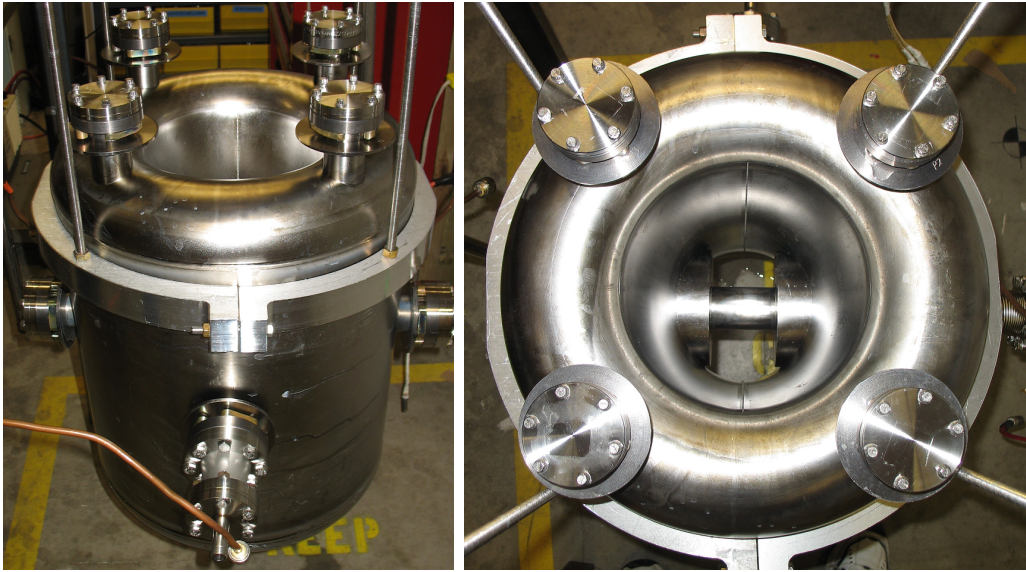


Figure 4.8: Prototype  $\beta = 0.53$  HWR manufactured and tested at MSU.

that has several important differences from the one presented in this document. A graphical comparison of the design being tested and a design of  $\beta = 0.53$  HWR more in line with the design choices presented in this document can be seen in Figure 4.9. Most major design differences are related to the inner conductor geometry, which is smoothly tapered to the short plates. While this design gives a smoother magnetic field region, especially though the high magnetic field region, significant drawbacks were discovered during prototyping. This short plate is difficult to form properly, especially achieving the diameter and taper required at the interface with the short plates, making welding quite challenging. The tolerances required on the fabrication of these parts was eased by the introduction of a short straight section at the interface between the inner conductor and short plate. This allows a



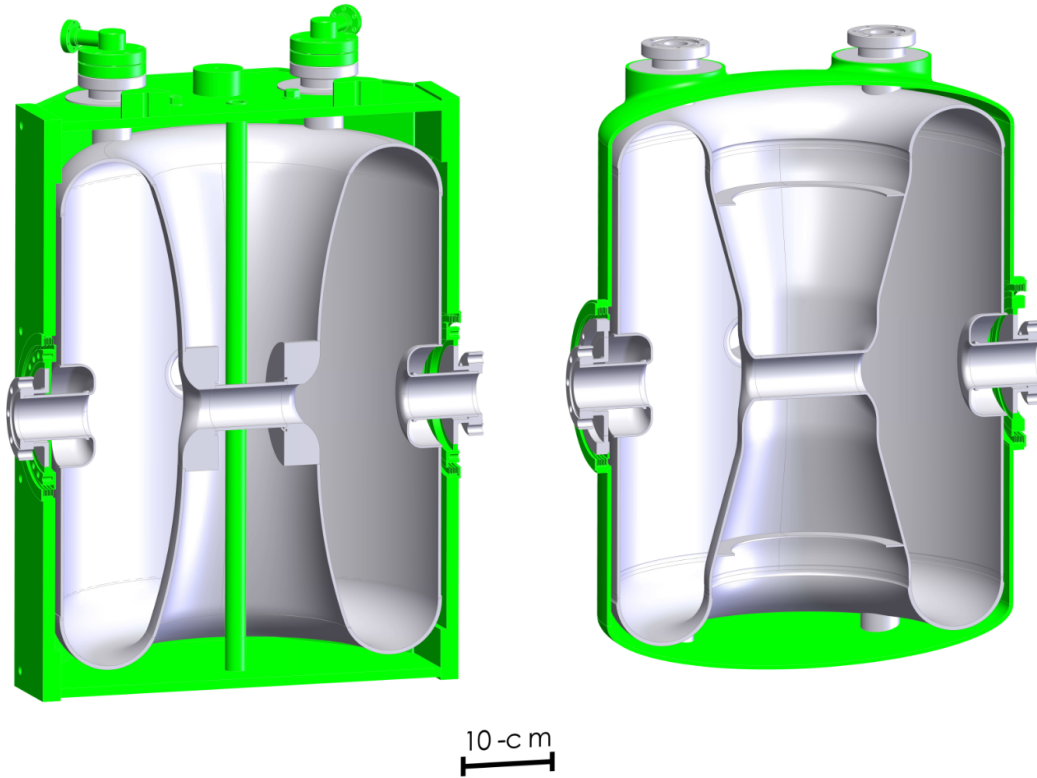


Figure 4.9: Left: Mechanical design of the prototype  $\beta = 0.53$  HWR, manufactured and tested at MSU. Right: More recent mechanical design of a  $\beta = 0.53$  HWR that shares many design features with the HWR designed in this document.

trimming and stacking step to ensure proper alignment during welding, hopefully improving the reliability of the welds. The formation of the drift tube has also been changed. On the design tested, the drift tube is machined out of a billet of solid niobium, then welded into the inner conductor. In the new design, the inner conductor is coined to provide the proper inner conductor curvature, then a niobium tube is welded in to connect one side to the other. This will greatly simplify fabrication of this region while not sacrificing too much in accuracy. The design presented in this document intentionally designs the drift tube region in such a way to be less sensitive to this increased manufacturing error.

### 4.4.2 Test Goals

In addition to verifying electromagnetic performance, the purpose of this test was to verify the effectiveness of the  $\sim 10$  hour,  $600^\circ\text{C}$  degassing bake procedure used on the cavity. The purpose of this bake is to drive out hydrogen from the cavity that was introduced during etching and other processing steps that could cause Q-Disease if the initial cooling of the cavity is not rapid enough. To this end, a two day test was scheduled. The first day would be used for initial cooling and electromagnetic testing, then a warming overnight to  $\sim 100\text{K}$  in an attempt to induce Q-Disease. The second day, the cavity would be re-cooled and retested to verify the effectiveness of the degassing bake.

### 4.4.3 Test Results and Implications

At the time of the test, the NSCL cryoplant was undergoing repairs, so the test had to be performed with purchased 500 L Dewars of liquid Helium. After precooling the test Dewar's liquid nitrogen jacket (seen in Figure 4.10), two of the purchased containers of liquid helium were used to cool the cavity/test Dewar and produce enough liquid to allow testing. The frequency increased from 321.3851 MHz warm to 321.9035 MHz cold. If frequency scaled like the ideal HWR, this ratio would be directly related to the thermal length contraction of niobium from 300 K to 4 K, giving a contraction of  $\sim -0.16\%$ . This compares favorably to the measured amount of  $\sim -0.14\%$ . Once the level of liquid helium was high enough, the cavity was disconnected from the purchased liquid helium, and pumping to 2 K began. The testing procedure was to measure the  $Q_0$  at  $E_{pk} = 1$  and 10 MV/m at different temperatures (4.2, 3.5, 3.0, 2.75, 2.5, 2.25, and 2 K) as the liquid helium pressure was reduced. Once the cavity reached 2 K, a full  $Q_0$  v.  $E_{pk}$  curve was to be measured and calibrations made. The

cavity was then returned to atmospheric pressure by reconnecting the NSCL cryoplant and heated (with resistive heater in the Dewar) to  $\sim 100$  K for an overnight soak. The next day, the purchased liquid helium was reconnected to recool the cavity and test Dewar and fill with liquid helium. The pumping process and measurements taken along the way were identical for direct comparison with the previous day's measurements, with warm and cold calibrations done after testing was completed.

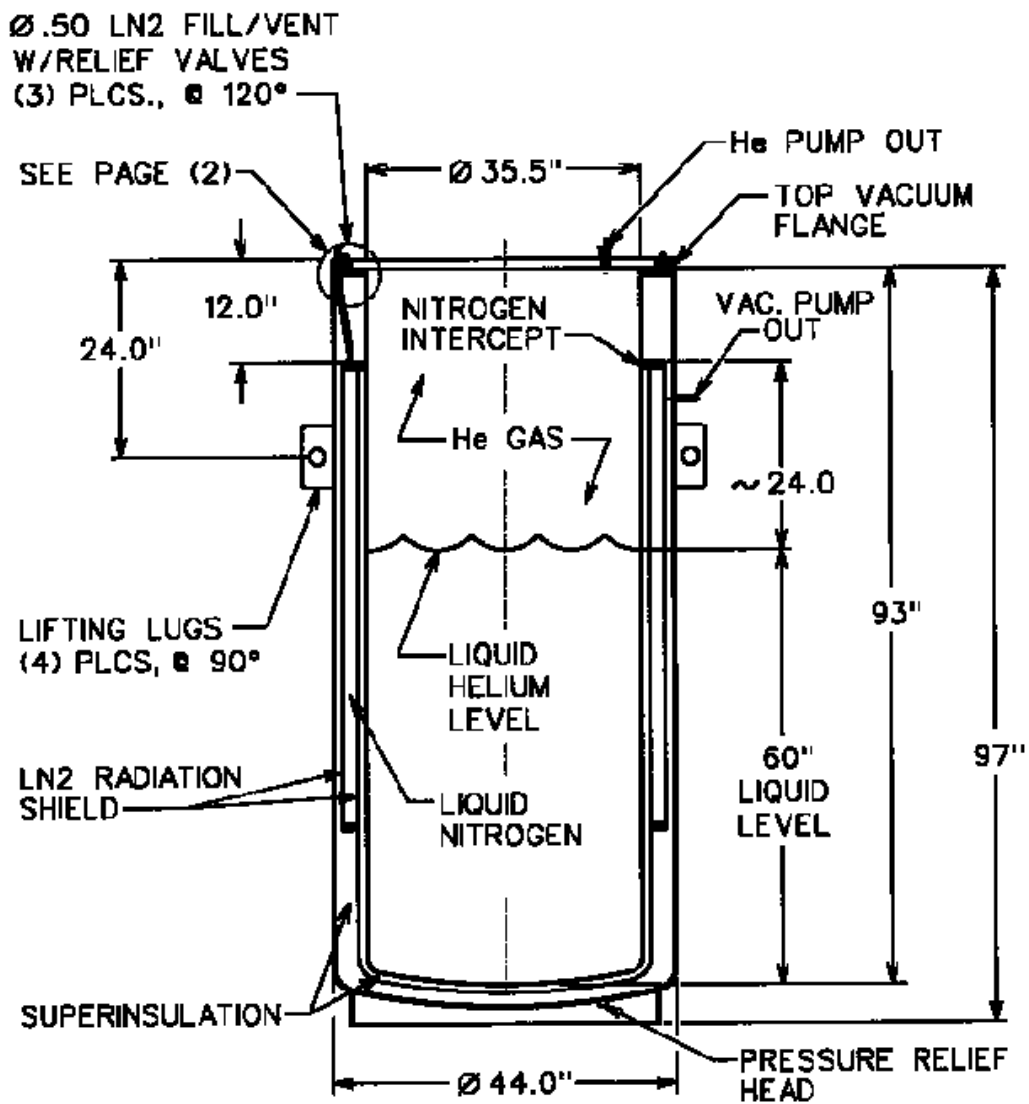


Figure 4.10: Mechanical Drawing of the NSCL large test Dewar, where this cavity test was performed.

The first important phenomenon to note was the sudden shifts in  $Q_{ext,2}$ . At the beginning of testing, the measured values of  $Q_{ext,2}$  were much higher, and suddenly shifted between the first and second day. It is thought that a connection or cable in the transmitted power circuit shifted or was damaged by thermal cycling during the night between testing days, although this could not be verified. The two days data is analyzed with the different measured values of  $Q_{ext,1}$  and  $Q_{ext,2}$ , which can be seen in Table 4.1. While the factor

Table 4.1: External Quality Factors used during Testing.

	$Q_{ext,1}$	$Q_{ext,2}$
Day 1	$6.2 \times 10^9$	$1.7 \times 10^{12}$
Day 2	$7.0 \times 10^9$	$1.7 \times 10^{11}$

of ten difference from one day to another is not typical, the validation of these values can be seen in Figure 4.11, where the proximity of the data to the Duality Triangle indicates internal consistency of the CW and modulated data.

The major conclusion is that the cavity performance did not change significantly as a result of the 100 K soak, indicating that the degassing bake was effective in preventing Q-Disease. The cavity also exceeded the FRIB field and quality factor goal on both days, further validating the cavity design and processing procedures used. These results also agree well with the cavity performance before the degassing bake [52]. This cavity design presented some challenges during fabrication. Because of the continuous taper of the inner conductor, the amount of force required to weld the cavity subassemblies was substantial. It is thought that the relatively sharp drop in quality factor above the FRIB field goal is related to the geometric features resulting from the poor quality of this weld, leading to the steps being taken to improve the quality of this welding which have already been discussed.

The testing data from both days, as well as the relationship between cavity performance and temperature, can be seen in Figure 4.12.

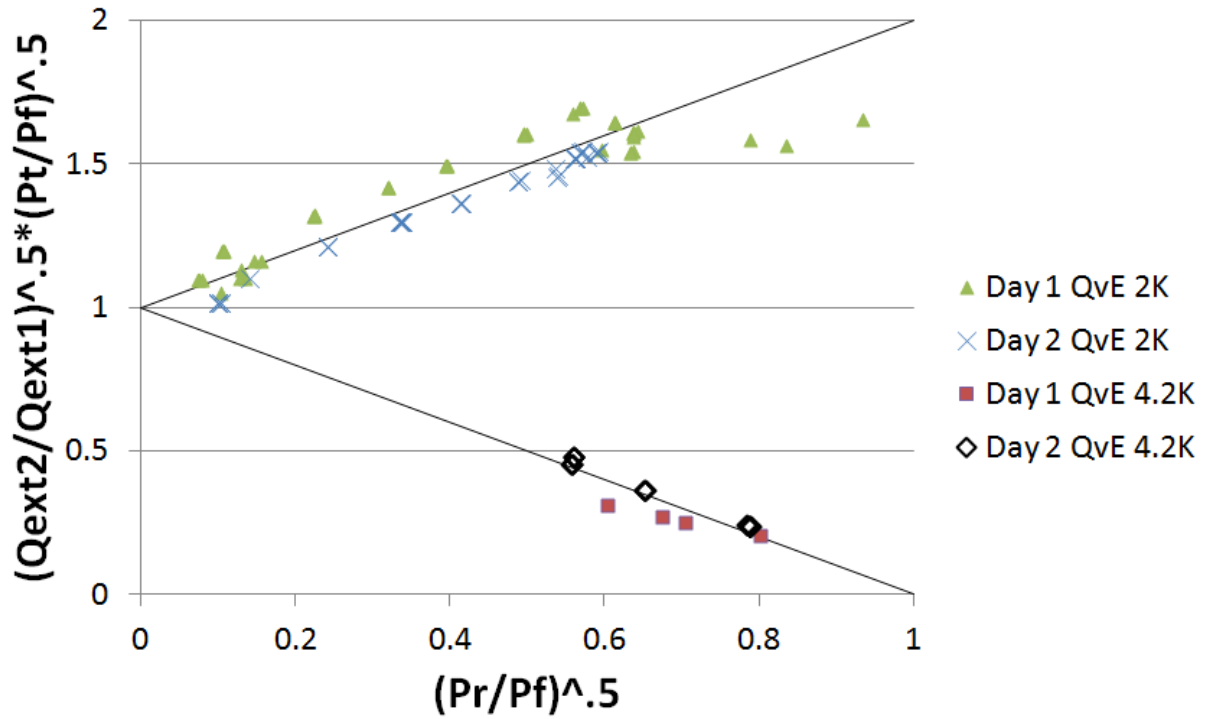


Figure 4.11: Both days of testing data plotted on the Duality Triangle to verify self consistency.

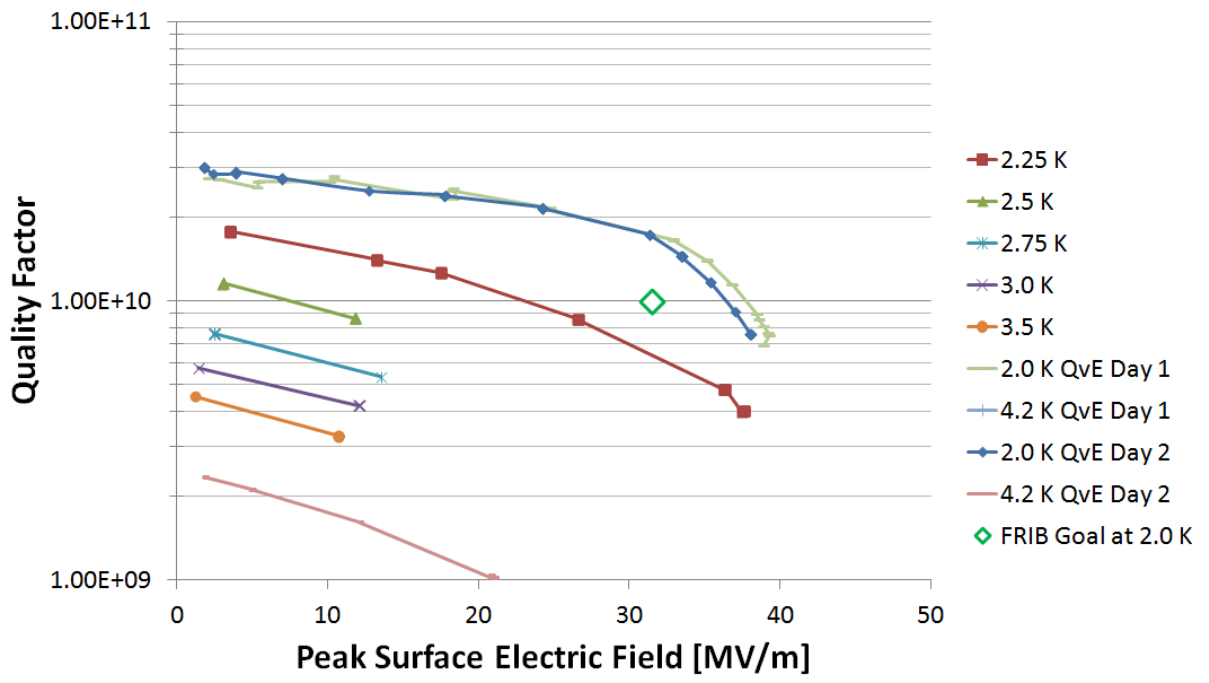


Figure 4.12: Cavity Quality Factor ( $Q_0$ ) plotted versus Peak Surface Electric Field for both testing days.

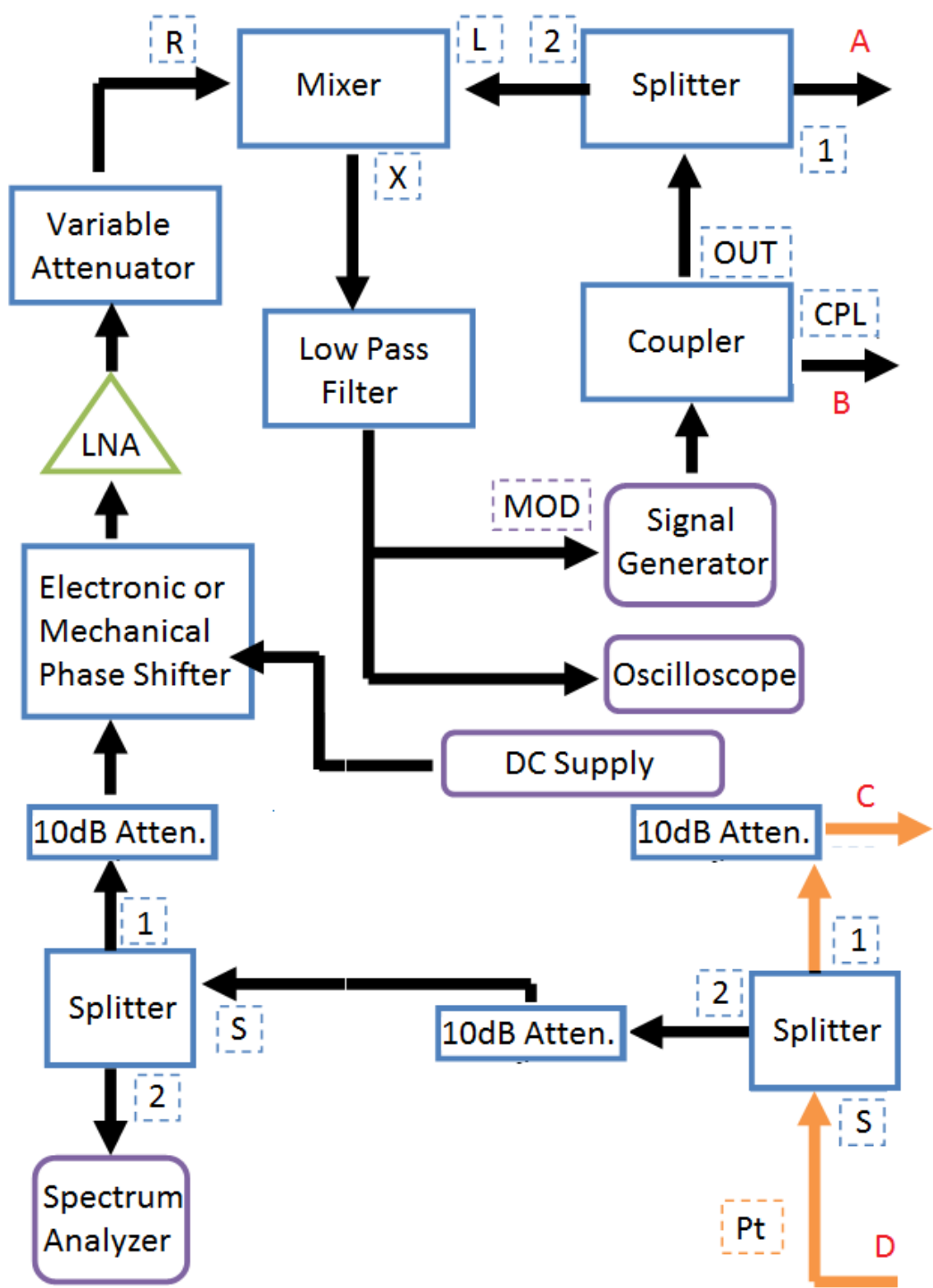


Figure 4.13: One half of the RF circuit for a phase lock loop for cavity testing (circulator, isolators, and RF diodes excluded). Letters in Red connect to the other half of the RF circuit, seen on the next page.

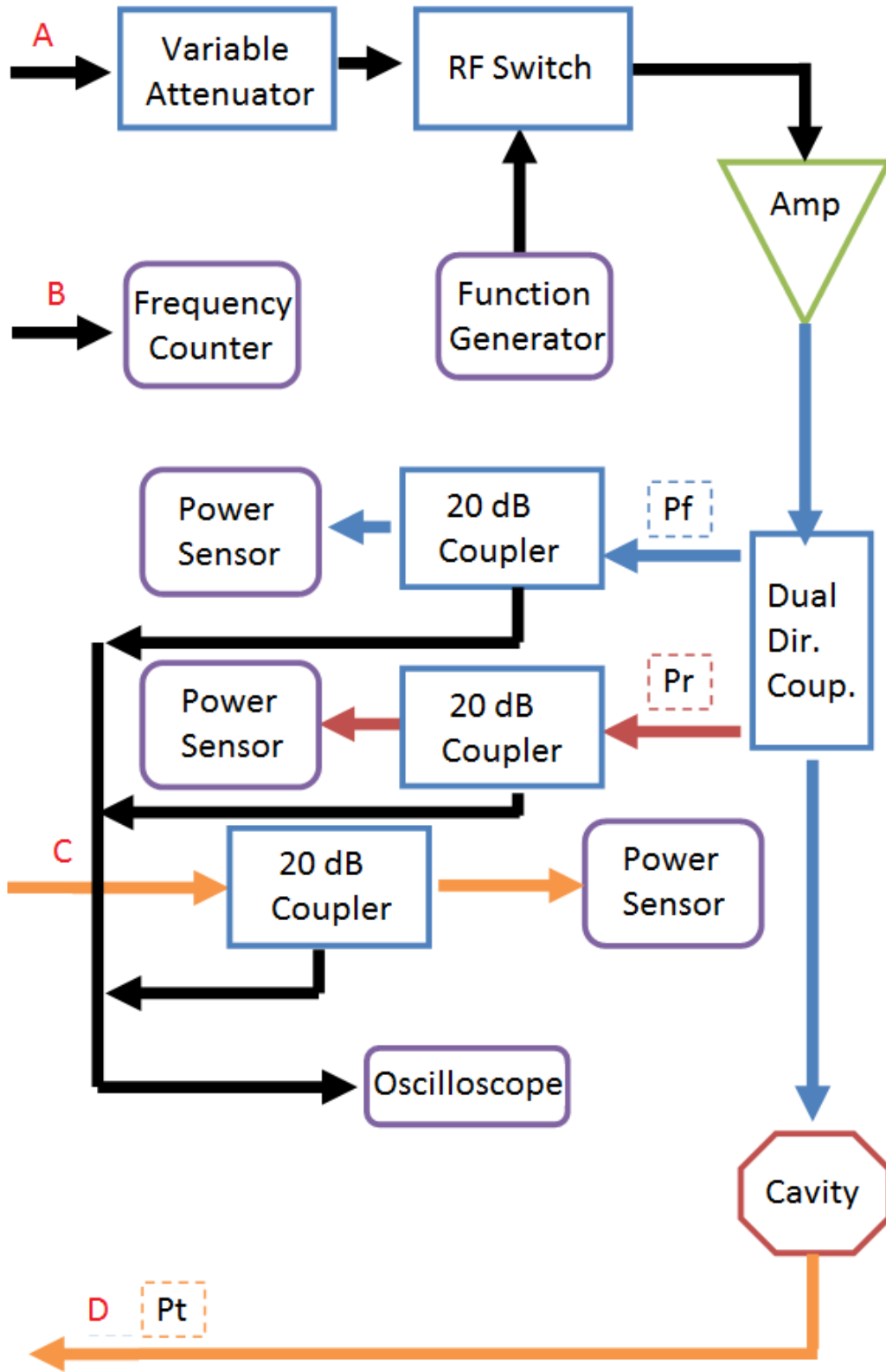


Figure 4.14: One half of the RF circuit for a phase lock loop for cavity testing (circulator, isolators, and RF diodes excluded). Letters in Red connect to the other half of the RF circuit, seen on the previous page.



# Chapter 5

## Conclusions

Through the course of this document, a theoretical and practical foundation has been laid for the design and usage of Half Wave Resonators for heavy ion linear accelerators. In this last chapter, this case will be summarized and extended to further potential applications.

### 5.1 Electromagnetic and Mechanical Simulations

Three dimensional computational simulation provides a powerful tool during the design of accelerating resonators. Properly done, both electromagnetic and mechanical simulations can be performed to great accuracy, allowing exploration of different designs and their implications before prototyping. Most problems can even be solved on a modern, powerful desktop computer, although more powerful codes and computer infrastructure exists when needed. However, the interconnection of simulation and prototyping in the design of a resonator cannot be overlooked, nor overstated. As the interface between powerful three dimensional geometry creation programs and flexible simulation software is improved, the design of these complex structures will become more rapid and accurate. The strength of simulations lies

in the rapid design optimization, the cost-effective analysis of many options. This relies, however, on the relative simplicity and exactness of the computerized model. Many real life considerations cannot be simulated, and prototyping must inform these decisions. This interaction becomes even more important during the design of complex geometries like HWRs. This is because the analytical formulas and simple two-dimensional simulations traditionally used for cavity design are not powerful enough to guide this type of design. The new generation of powerful simulation software must be matched with the human experience of prototyping and testing these new, complex geometries for future projects that will rely on them to succeed.

## **5.2 On Simulation Scripting and Optimization**

Cavity design requires a solid understanding of both the electromagnetic behavior of a design and the mechanical complexities of fabrication. This knowledge can be used to design the cavity geometry with the proper variables and features required to efficiently optimize the design while allowing practical and reliable fabrication. While prototyping almost invariably uncover unexpected factors and problems that require further cavity design iterations, proper parameterization greatly speeds cavity optimization. The optimization time itself can be greatly reduced with simulation scripting and automation. The scripts seen in the Appendices required significant time and effort to create, but once completed they greatly facilitated rapid simulation and optimization. This scripting is possible because ANSYS-APDL is designed to make geometric references consistent and allows very flexible geometric reference operations. An excellent example of this flexibility can be seen in this section from Appendix A:

```

!Calculates Volume parameters

vsum

!Select volume 1

vsel,s,,1

!Define cavity vacuum as "cavity"

cm,cavity,volu

!Select "cavity"

cmsel,s,cavity

!Select areas associated with cavity vacuum

aslv,s

!Unselect symmetry planes

asel,u,loc,x,0

!asel,u,loc,y,0

asel,u,loc,z,0

!asel,u,,4

!Define PEC walls

cm,cavwall,area

aplot

```

This section of code defines two objects for use later in the script: the cavity vacuum volume *cavity* and the cavity RF surfaces *cavwall*. These references are used extensively through the rest of the scripts to set boundary conditions and for post-processing. It is important to note the extreme flexibility of the code used to do this. For essentially any cavity type, this code will work properly if the correct volume number is used in line 4 and the appropriate

symmetry planes are selected in lines 12-14, an almost trivial amount of work. This is just one example of this scripting philosophy that can be seen in the Appendices, and it allows rapid generation of the appropriate scripts for a wide variety of cavity designs, greatly speeding simulation. This means that the time required for parameter scans used to optimize cavity performance can be reduced to the time it takes for the computation. Proper scripting of the meshing can also reliably reduce this time as well. Some code systems like ACE3P are being designed to be fully scriptable, from geometry creation to post-processing, using high-power computing clusters to speed simulation time. This suite of software shows great promise for allowing rapid simulation and optimization of even the most complex geometries. Simulation software that allows scripting and optimization like this is understandably preferable for serious optimization projects.

### **5.3 On the Practicality of Half Wave Resonators**

HWRs as described in this document provide a large amount of flexibility and reliability, perfectly suited to the needs of a project such as FRIB. The combination of the geometry's two-gap structure and relatively compact, low-frequency nature make it ideal for accelerating particles from the upper end of practical QWR velocities ( $\beta \sim 0.2$ ) to the lower end of elliptical cavity velocities ( $\beta \sim 0.7$ ) while requiring a minimum number of different designs. Additionally, the design choices advocated in this document result in a relatively simple and mechanically robust geometry, straight-forward to fabricate, process, and operate reliably. To be sure, an active research and development program will be required to realize the HWR's potential, but almost all of this work will be an extension of existing technology applied in a new environment rather than completely new technology. Much of this work will involve

characterization of frequency shifts during fabrication in order to reliably achieve the design frequency. These shifts can come from variations in subassembly fabrication, the welding of the subassemblies into a finished cavity, and chemical processing. Prototyping of the HWR design will allow the repeatable shifts to be taken into account beforehand, and design features like the short straight section on the inner conductor and the beam port cup allow any drift in frequency to be tracked and corrected for during fabrication. The reliability of RF performance is assisted by the addition of the rinse ports for processing and the intentional lack of complex RF joints near high field regions. The cavity design can also be made very mechanically robust. The choice of a straight outer conductor, and hemispherical short plates created a very stiff cavity, insensitive to pressure fluctuations. This greatly simplifies the design of the cavity stiffening because the extensive fine-tuning of field compensation is not required, with the additional benefit of making the mechanical properties of the cavity quite insensitive to manufacturing error. The complexity (and hopefully cost) of fabrication can therefore be minimized by forming most of the cavity from standard thickness stock sheet material whenever possible, including the stiffening ring, and minimizing the linear inches of electron beam welding required.

## **5.4 Future Designs and Applications of Half Wave Resonators**

Because of the flexibility of the HWR, many future accelerators could benefit from their inclusion. For this style of HWR, many heavy ion/rare isotope facilities currently running could use this technology as a relatively low cost option for boosting available energies. Pro-

ton/light ion accelerators would benefit from the efficient, high-current acceleration possible with HWRs. These accelerators would likely require a HWR design optimized for the highest gradient possible, likely increasing the peak surface fields to make the accelerator as compact as possible. From the research and development performed at MSU, adaptation of the HWR for these different applications will be significantly less expensive and more reliable, in the same way ATLAS at Argonne laid the foundation for QWR technology.

# Chapter 6

## ANSYS-APDL Scripting and Discussion

### 6.1 ANSYS-APDL Electromagnetic Script

This section is a basic script for the simulation of the resonant frequency and mode structure of a cavity geometry. The geometry is generated using SolidWorks and imported as a SAT file. This script includes mesh refinement and use of symmetry planes.

```
/UNITS,SI  
  
!Set place for simulation files  
  
!/CWD,'c:\Holzbauer\Simulations'  
  
!/MKDIR,'053rinsetest'  
  
!/CWD,'c:\Holzbauer\Simulations\HWR29f'  
  
!/FILENAME,053rinsetest,1  
  
fini
```

```
!Clears ANSYS databases

/CLEAR

!Suppress Popup messages

/UIS,msgpop,3

/OUTPUT,HWR29f,log

!Use this for 32 bit machines to avoid file size limit

!/config,fsplit

!Enter Setup command stage

/prep7

!Input SAT file from SolidWorks

~SATIN,HWR29fmodel_1,'SAT',

'I:\projects\accelerator\holzbaue\SRF Work\New HWR29f\'',SOLIDS,0

!Changes to solid plotting

/facet,norm

!Sets area numbering to true

/pnum,area,1

!Plot Areas

aplot

!Merge areas/numbers

nummrg,all

numcmp,all

/replot
```



```

!Calculates Volume parameters

vsum

!Select volume 1

vsel,s,,1

!Define cavity vacuum as "cavity"

cm,cavity,volu

!Select "cavity"

cmsel,s,cavity

!Select areas associated with cavity vacuum

aslv,s

!Unselect symmetry planes

asel,u,loc,x,0

!asel,u,loc,y,0

asel,u,loc,z,0

!asel,u,,4

!Define PEC walls

cm,cavwall,area

aplot

!Define constants

!Max global element size

*SET,fine , .04

```

```

*SET,freq0 , 322e6 !design frequency
!*SET,beta1 , .285 !optimum particle velocity guess
*SET,pi , acos(-1) !
*SET,c0 , 2.998e8 !
*SET,mu0 , 4*pi*1e-7 !Permeability
*SET,eps0 , 8.85*1e-12 !Permittivity
!*SET,cond ,9.8e5 !SS conductivity
!*SET,cond , 5.8e7 !copper conductivity
!*SET,rs_1 , (pi*freq0*mu0/cond)**.5 !surface resistance
!Calculate SRF conductivity and surface resistance
*SET,rs_1, 10E-9
*SET,cond, (pi*freq0*mu0/rs_1**2)

cmsel,s,cavity,volume

!Attach element type 1 to cavity and make it HF199 elements
vatt,1,,1

!Second order elements (the last number)
et,1,119,2

!Define material parameters as vacuum
mp,murx,1,1
mp,perx,1,1

!Automatic meshing settings (1 to 10, 1 is finest)
smrtsize,1

```

```
!Set global max meshing size to fine

!vsel,s,,1

!esize,fine

!Refinement on specific areas and lines

asel,s,,15

lsla,s

asll,s

asel,u,loc,x,0

!asel,u,loc,y,0

asel,u,loc,z,0

aesize,all,.002

allsel

!aesize,32,.004

!aesize,23,.001

!aesize,14,.001

!aesize,7,.001

!aesize,16,.001

!aesize,6,.001

!lesize,20,.001

!Actual meshing command

vmesh,all
```

```

!Select all components
allsel

cmsel,s,cavity,volume

FINISH

!Enter solving process
/sol

!Select Cavity wall areas
cmsel,s,cavwall

!asel,u,,7

!Select Cavity wall nodes
nsla,s,1

!Define cavity wall as PEC, all else defaults to PMC
d,all,ax,0

!Add loss condition to cav walls with previously defined cond
sfa,all,,shld,cond,1.0

cm,pecnodes,node

allsel

!Solve type is eigenmodal
antype,modal

!Set freq search range, number of modes to solve for in that range
modopt,lanb,1,.9*freq0,1.1*freq0,,on

```

```

mxpand,, ,yes

solve

!Save frequency value for later

*get,f_nd1,mode,1,freq

FINISH

!Enter post processing

/post1

!Read lowest mode solution data

SET, FIRST

!Plot mag-efield

plnsol,ef,sum,0

!plnsol,h,sum,0

cmsel,s,cavity

!Read surface losses and stored energy into element table

etable,surflo1,nmisc,8

etable,energy1,nmisc,6

!etable,volume1,volume

!cmsel,s,cavwall

!Get cavity volume (from vsum earlier)

*GET,vol_1,VOLU,1,VOLU

!Get element mag of electric fields

etable,ef_mags,ef,sum

```

```

allsel

ssum

!Sum stored energy and multiply for symmetry
*get,u_1,ssum,0,item,energy1

u_1=4*u_1

!Same for dissipated power
*get,pd_1,ssum,0,item,surflo1

pd_1=4*pd_1

!*get,vol_1,ssum,0,item,volume1

!Same for volume

vol_1=4*vol_1

!Calculate Quality Factor and Geometry Factor
qual_1=2*pi*freq0*u_1/pd_1
geom_1=rs_1*qual_1

!etable,ef_mags,ef,sum

!Get peak electric field and normalize to the stored energy
esort,etab,ef_mags,,1,10

*get,e_pk1,sort,ef_mags,max

epksqru=e_pk1/(u_1)**.5

!Repeat for magnetic field

etable,hf_mags,h,sum

allsel

```

```

esort,etab,hf_mags,,1,10

*get,h_pk1,sort,hf_mags,max

hpksqru=h_pk1/(u_1)**.5

!define beam axis

path,vaxi,2,30,500

ppath,1,,0.170,0.000,0.000

ppath,2,,0.000,0.000,0.000

!Extract accelerating electric field

pdef,e_x0,ef,x

!Integrate Eacc to get V_0

pcalc,intg,v_0,e_x0,xg

pcalc,exp,v_0,v_0,,2

pcalc,exp,v_0,v_0,,0.5

*get,v01,path,0,last,v_0

!Calculate beta optimum

v_max=0

betaopt=0

*DIM,ttfplot,table,1000,1

*DIM,betaplot,table,1000,1

!step beta by .001

```

```

*D0,i,.001,1,.001

!Calculate time varying factor along path
fact1=2*pi*freq0/(i*c0)

pcalc,sin,sinx,xg,,fact1

!Multiply by field along path and integrate
pcalc,mult,v_xi,e_x0,sinx

pcalc,intg,v_acc,v_xi,xg

pcalc,exp,v_acc,v_acc,,2

pcalc,exp,v_acc,v_acc,,0.5

!Get accelerating voltage
*get,vacc1,path,0,last,v_acc

ttf=vacc1/v01

!Ratchet function to get beta and voltage optimum
*IF,vacc1,GT,v_max,THEN

*SET,v_max,vacc1

betaopt=i

*ENDIF

*SET,ttfplot(i*1000,1),ttf

*SET,betaplot(i*1000,1),i

*ENDDO

!Plot TTF curve

!*vplot,betaplot,ttfplot

```



```

!Repeat calculation for Vacc optimum
fact1=2*pi*freq0/(betaopt*c0)
pcalc,sin,sinx,xg,,fact1
pcalc,mult,v_xi,e_x0,sinx
pcalc,intg,v_acc,v_xi,xg
pcalc,exp,v_acc,v_acc,,2
pcalc,exp,v_acc,v_acc,,0.5
*get,vacc1,path,0,last,v_acc
ttf=vacc1/v01
!Normalize all figures of merit to 1 J stored energy and to 1.9MV accelerating
vaccu1=2*(vacc1*vacc1/u_1)**.5
v0u1=2*(v01*v01/u_1)**.5
U19=(1.9e6/vaccu1)**2
Bpk19=hpksqru*U19**.5/795.775
Epk19=epksqru*U19**.5
RoverQ = 1.9e6**2/(2*pi*freq0*U19)
Bpksqru=hpksqru/795.775
Eacc19=1.9e6/(betaopt*3e8/f_nd1)
!Read values to screen
*status
!Plot E-field again
plnsol,ef,sum,0
!plpath,e_x0

```

```
!Get local peak field

!lsl,s,,20

!nsl,s

!esln,s

!etable,h_joint,h,sum

!allsel

!esort,etab,h_joint,,1,10

!*get,j_pk1,sort,h_joint,max

!jointPK19=j_pk1*(U19/u_1)**.5/795.775

!*status,jointPK19

!Get losses on specific part of the cavity

!asel,s,,13

!asel,s,,28

!lsla,s

!asll,s

!lsla,s

!asll,s

!lsla,s

!asll,s

!nsla,s
```

```

!esln,s

!etable,surflo2,nmisc,8

!ssum

!*get,pd_2,ssum,0,item,surflo2

!pd_2=4*pd_2

!pd_plung=pd_2*U19/u_1

!*status,pd_plung

!Qext measurements

!asel,s,,7

!nsla,s

!esln,s

!etable,qextemag,ef,sum

!!etable,qexthmag,h,sum

!esort,etab,qextemag,,1,10

!*get,qextpk1,sort,qextemag,max

!qextpk1=qextpk1*(U19/u_1)**.5

!*status,qextpk1

```

## 6.2 ANSYS-APDL Mechanical Script

This section is an extension of the scripting used in the previous chapter. This script takes a solid model of the *Niobium* space of a cavity, generates the vacuum space, then simulates the resonant frequency of the cavity. The cavity is then deformed based on some applied pressure. The deformed vacuum space is used to simulated the shifted resonant frequency, and the difference in frequency is calculated.

```
!Import vacuum space

/UNITS,SI

/CWD,'f:\Holzbauer\Simulations'

/MKDIR,'29fHWRhevLFD'

/CWD,'f:\Holzbauer\Simulations\29fHWRhevLFD'

/FILNAME,29fHWRhevLFD,1

!/CWD,'c:\Holzbauer\Simulations'

!/MKDIR,'29fHWRhevLFD'

!/CWD,'c:\Holzbauer\Simulations\29fHWRhevLFD'

!/FILNAME,29fHWRhevLFD,1

fini

/cle

/UIS,msgpop,3

/OUTPUT,29fHWRhevLFD,log
```

```
/config,fsplit

/prep7

!/title, 29fHWRhevLFD_2 J.P. Holzbauer

~SATIN,HWR29ffull_1,'SAT',

'I:\projects\accelerator\holzbaue\SRF Work\New HWR29f',SOLIDS,0

/facet,norm

/pnum,area,1

aplot

vglue,all

nummrg,all

numcmp,all

/replot

!Forces solve even upon errors

/NERR,200,99999999

asel,s,loc,x,0

!asel,a,loc,y,0

asel,a,loc,z,0

asel,a,,198 !Coupler1

asel,a,,48 !Coupler2

asel,a,,51 !beam1
```

```

asel,a,,,197 !beam2
asel,a,,,204
asel,a,,,195
asel,a,,,176
!asel,a,,,99 !gap in HeV
!asel,a,,,15 !gap in HeV
!asel,a,,,140 !gap in HeV
!asel,a,,,5 !gap in HeV
cm,edges,area

vsel,s,,,2
aslv,s
vsel,s,,,1
vsel,a,,,3
aslv,r
aplot

cm,common,area

!Create missing Keypoints and generate lines
!*get,kmx,kp,,num,max !get max kp
!*set,k1,kmx+1
!k,k1,0,0,0 !set origin as kp=k1

```

```
!*get,cex,kp,69,loc,x
!*set,k2,kmx+2
!*get,cez,kp,112,loc,z
!*set,k3,kmx+3
!k,k2,cex,0,0
!k,k3,0,0,cez
!l,k1,48
!l,k2,69
!l,k1,114
!l,k1,66
!l,k2,86
!l,k3,112
!l,k3,116

!Seed area for cavity wall
asel,s,,40
aplot
*D0,q,1,20,1
lsla,s
asll,s
asel,u,,edges
cmsel,u,common
aplot
```

\*ENDDO

cm,cavwall,area

lsla,s

lsel,r,loc,x,0

lsel,u,,2

lsel,u,,,96

1,36,91

al,all

lsel,s,,2

lsel,a,,,96

1,3,84

al,all

cmsel,cavwall,area

lsla,s

lsel,r,loc,z,0

1,12,71

al,all

!Seed area for pressure wall

asel,s,,,17



```
aplot
*D0,q,1,25,1
lsla,s
asll,s
asel,u,,edges
cmsel,u,common
aplot
*ENDD0
cm,presswall,area

allsel
al,12,95,556
al,163,32
al,554,28,167

cmsel,s,cavwall
lsla,s
asll,s
asel,u,,edges
cmsel,u,common
va,all

cm,vacuum,volume
```

```

*SET,coars , .01

*SET,freq0 , 322e6 !design frequency

!*SET,beta1 , .285 !optimum particle velocity guess

*SET,pi , acos(-1) !

*SET,c0 , 2.998e8 !

*SET,mu0 , 4*pi*1e-7 !Permeability

*SET,eps0 , 8.85*1e-12 !Permittivity

*SET,cond , 5.8e7 !copper conductivity

*SET,rs_1 , (pi*freq0*mu0/cond)**.5 !surface resistance

*DIM,tffplot,table,1000,1

*DIM,betaplot,table,1000,1

!Fine-tuning mesh

allsel

et,1,119,1

et,2,187

!Rinse Port Stub

!E type 2 = SS

smrtsize,6

```

```
vsel,s,,1
```

```
vatt,2,,2
```

```
vmesh,all
```

```
!Helium Vessel
```

```
!E type 2 = SS
```

```
smrtsize,6
```

```
vsel,s,,3
```

```
vatt,2,,2
```

```
vmesh,all
```

```
!Cavity Wall
```

```
!E type 4 = Nb
```

```
smrtsize,4
```

```
vsel,s,,2
```

```
!asel,s,,20,21
```

```
!aesize,all,.002
```

```
vatt,4,,2
```

```
vmesh,all
```

```
!Cavity Vacuum
```

```
!E type 1 = vacuum
```

```
vsel,s,,4
```

```
smrtsize,4
vatt,1,,1
mp,murx,1,1
mp,perx,1,1
vmesh,all
!esize,coars
!smrtsize,1

!asel,s,,94
!*D0,q,1,5,1
!lsla,s
!asll,s
!*ENDDO
!aesize,all,.003
!allsel

et,2,0

FINISH

!Defining losses on walls and solving for f_nd freq
/sol
cmsel,s,cavwall
```

```
nsla,s,1
d,all,ax,0
sfa,all,,shld,cond,1.0
cm,pecnodes,node
allsel
vsel,s,,4
eslv,s
antype,modal
modopt,lanb,1,.9*freq0,1.1*freq0,,on
mxpand,,,,yes
solve
*get,f_nd1,mode,1,freq
FINISH

/post1
allsel
SET,FIRST
cmsel,s,cavwall
nsla,s
esln,s
etable,sef_mags,ef,sum
etable,shf_mags,h,sum
allsel
```

```

etable,energy1,nmisc,6
etable,surflo1,nmisc,8
etable,ef_mags,ef,sum
etable,hf_mags,h,sum

ssum

*get,u_1,ssum,0,item,energy1
u_1=4*u_1

*get,pd_1,ssum,0,item,surflo1
pd_1=4*pd_1

*GET,vol_1,VOLU,6,VOLU
vol_1=4*vol_1

qual_1=2*pi*f_nd1*u_1/pd_1
geom_1=rs_1*qual_1
esort,etab,ef_mags,,1,10
*get,e_pk1,sort,ef_mags,max
epksqru=e_pk1/(u_1)**.5
esort,etab,hf_mags,,1,10
*get,h_pk1,sort,hf_mags,max
hpksqru=h_pk1/(u_1)**.5

!Define beam axis
path,vaxi,2,30,500

```

```

ppath,1,,0.000,0.000,0.000
ppath,2,,0.170,0.000,0.000
pdef,e_x0,ef,x
pcalc,intg,v_0,e_x0,xg
pcalc,exp,v_0,v_0,,2
pcalc,exp,v_0,v_0,,0.5
!Calculating integrated voltage with no time dependence
*get,v01,path,0,last,v_0

!Calculate TTFplot and find betaopt
v_max=0
betaopt=0

*D0,i,.001,1,.001
fact1=2*pi*f_nd1/(i*c0)
pcalc,sin,sinx,xg,,fact1
pcalc,mult,v_xi,e_x0,sinx
pcalc,intg,v_acc,v_xi,xg
pcalc,exp,v_acc,v_acc,,2
pcalc,exp,v_acc,v_acc,,0.5
*get,vacc1,path,0,last,v_acc
ttf=vacc1/v01
*IF,vacc1,GT,v_max,THEN

```

```

*SET,v_max,vacc1

betaopt=i

*ENDIF

*SET,ttfplot(i*1000,1),ttf

*SET,betaplot(i*1000,1),i

*ENDDO

!*vplot,betaplot,ttfplot

!Integrate accelerating voltage
fact1=2*pi*f_nd1/(betaopt*c0)
pcalc,sin,sinx,xg,,fact1
pcalc,mult,v_xi,e_x0,sinx
pcalc,intg,v_acc,v_xi,xg
pcalc,exp,v_acc,v_acc,,2
pcalc,exp,v_acc,v_acc,,0.5
*get,vacc1,path,0,last,v_acc
ttf=vacc1/v01
vaccu1=2*(vacc1*vacc1/u_1)**.5
v0u1=2*(v01*v01/u_1)**.5

!Normalize figures of merit to 1.9MV accelerating
FieldU=(1.9e6/vaccu1)**2
FieldBpk=hpksqru*FieldU**.5/795.775
FieldEpk=epksqru*FieldU**.5

```



```
RoverQ = 1.9e6**2/(2*pi*f_nd1*FieldU)
```

```
Bpksqru=hpksqru/795.775
```

```
!WATCH SIGN, IS SET WITH FORCE INWARD
```

```
!Uncomment to do LFD
```

```
smult,e_1,sef_mags,,(FieldU/u_1)**.5
```

```
smult,h_1,shf_mags,,(FieldU/u_1)**.5
```

```
smult,e_sqr,e_1,e_1,.25,8.85418e-12
```

```
smult,h_sqr,h_1,h_1,-.25,12.5664e-7
```

```
sadd,LFDP,h_sqr,e_sqr
```

```
FINISH
```

```
!Prepare loading for df/dp
```

```
/prep7
```

```
!cmsel,s,cavity,volume
```

```
!Redefining vacuum space material/element
```

```
et,1,187 !Solid element type as material 1
```

```
et,2,187
```

```
mp,ex,1,1 !weak elastic moduli
```

```

mp,nuxy,1,.38 !Major Poisson's ratios
mp,dens,1,.01 !Mass Density

!titanium

!mp,ex,2,1.23e11 !elastic moduli
!mp,nuxy,2,.338 !Major Poisson's Ratio
!mp,dens,2,4510 !Mass Density
!mp,alpx,2,8.5e-6 !Secant coefficients of thermal expansion

!304 Stainless Steel for the helium vessel
mp,ex,2,2e11 !elastic moduli
mp,nuxy,2,.33 !Major Poisson's Ratio
mp,dens,2,7860 !Mass Density
mp,alpx,2,1e-7 !Secant coefficients of thermal expansion

!niobium titanium (guesses!)
mp,ex,3,1.24e11 !elastic moduli
mp,nuxy,3,.32 !Major Poisson's Ratio
mp,dens,3,5700 !Mass Density
mp,alpx,3,7.5e-6 !Secant coefficients of thermal expansion

!niobium
mp,ex,4,1.25e11 !elastic moduli

```

```
mp,nuxy,4,.301 !Major Poisson's Ratio
mp,dens,4,8570 !Mass Density
mp,alpx,4,7e-6 !Secant coefficients of thermal expansion
!r,1,.002 !thickness?
```

```
!Adding pressure load on walls
```

```
cmsel,s,presswall
```

```
!vsel,s,,all
```

```
!aslv,s
```

```
!nsla,s
```

```
!esln,s
```

```
!This line applies force for df/dP
```

```
!sfa,all,1,pres,5000
```

```
!Applies Tuning force
```

```
!asel,s,,197
```

```
!asel,a,,51
```

```
!sfa,all,1,pres,5000
```

```
!asum
```

```
!*get,forcearea,AREA,197,AREA
```

```
!*get,forcearea2,AREA,51,AREA
```

```
!forcearea3 = forcearea+forcearea2
```

```

!force=5000*forcearea3*2

allsel

!This section applies LFD forces

vsel,s,,6

eslv,s

*GET,minelem,ELEM,0,NUM,MIN

*GET,maxelem,ETAB,0,NLENG,MAX

cmsel,s,cavwall

*DO,k,minelem,maxelem,1

*GET,press,ETAB,11,ELEM,k

*IF,press,NE,0,THEN

esel,s,,k

nsle,s

cmsel,r,pecnodes

nsla,r

sf,ALL,PRES,press

*ENDIF

*ENDDO

!Setting symmetric conditions

```

```
allsel
nset,s,loc,x,0
dsym,symm,x
nset,s,loc,z,0
dsym,symm,z
!nset,s,loc,y,0
!dsym,symm,y

!Fixing drift tube center
aset,s,,15

!Fixing beam port
aset,a,,197
aset,a,,51

!Fixing Tuning plate
!aset,s,,205
nsla,s
!lset,s,,658
!nsl1,s
d,all,all,0

!nset,all
allsel
```

```
!esel,s,type,,3
```

```
!nsle,s
```

```
FINISH
```

```
/sol
```

```
antype,static
```

```
solve
```

```
FINISH
```

```
!Plotting and updating coordinate systems for next solve
```

```
/post1
```

```
plnsol,u,sum,2,1.0
```

```
upcoord,1
```

```
FINISH
```

```
!get shifted frequency
```

```
/prep7
```

```
et,1,119,1
```

```
et,2,0
```

```
mp,murx,1,1
```

```
mp,perx,1,1
```

```
vsel,s,,,1,3
```

```
vclear,all
vdele,all
allsel
FINISH

/sol

cmsel,s,cavwall
nsla,s,1
d,all,ax,0
sfa,all,,shld,cond,1.0
esel,s,type,,1
nsle,s
antype,modal
modopt,lanb,1,.9*freq0,1.1*freq0,,on
mxpand,,,yes
solve
*get,f_nd2,mode,1,freq
FINISH

/post1
*SET,fshift,(f_nd2-f_nd1)
*STATUS, fshift
FINISH
```

# BIBLIOGRAPHY



# BIBLIOGRAPHY

- [1] E. N. da C. Andrade (1964), “Rutherford and the Nature of the Atom”, p. 111
- [2] LHC Design Report, <http://lhc.web.cern.ch/lhc/LHC-DesignReport.html>
- [3] D.A. Edwards, M.J. Syphers, “An Introduction to the Physics of High Energy Accelerators”, John Wiley and Sons Inc.
- [4] G. Stupakov, “Lecture notes on Classical Mechanics and Electromagnetism in Accelerator Physics”, United States Particle Accelerator School, Revision 20, 2011
- [5] B. Van der Pol, J. Van der Mark, “Frequency demultiplication”, *Nature*, 120, 363-364, (1927)
- [6] J.D. Jackson (1999), “Classical Electrodynamics, 3rd Edition”, John Wiley and Sons Inc.
- [7] H. Padamsee, J. Knobloch, T. Hayes (2008), “RF Superconductivity for Accelerators, 2nd Edition”, John Wiley and Sons Inc.
- [8] J.D. Jackson (1999), “Classical Electrodynamics, 3rd Edition”, John Wiley and Sons Inc., p. 298
- [9] A. Facco, V. Zvyagintsev, “Beam Steering in Superconducting Quarter-Wave Resonators: An Analytical Approach”, *Phys. Rev. ST Accel. Beams* 14, 070101 (2011)
- [10] E. Zaplatin et al., “Low-Beta Superconducting RF Three-Quarter Wavelength Cavities”, ESS 02-125-L, April 2002, Juelich

- [11] M. Tinkham, "Introduction to Superconductivity, 2nd Edition", Dover Publications, Inc., p. 44
- [12] M. Tinkham, "Introduction to Superconductivity, 2nd Edition", Dover Publications, Inc., Chapter 3
- [13] J. Bardeen, L. N. Cooper, and J. R. Schrieffer, Phys. Rev. 108, 1175 (1957)
- [14] H. Padamsee, J. Knobloch, T. Hayes (2008), "RF Superconductivity for Accelerators, 2nd Edition", John Wiley and Sons Inc., p. 88
- [15] W. Hartung, "Introduction to Superconducting Cavities: Lecture Notes for USPAS Course on Beam Measurements and Experiments at NSCL", Lecture notes, US Particle Accelerator School, Michigan State University, June 2007
- [16] A. Facco, "SRF Low-beta Accelerating Cavities for FRIB", Lecture notes, Phys 905 - The Accelerator Physics of FRIB, Michigan State University, October 2011
- [17] F. and H. London, Proc. Roy. Soc. (London) A149, 71 (1935)
- [18] M. Tinkham, "Introduction to Superconductivity, 2nd Edition", Dover Publications, Inc., Chapter 1
- [19] W. Meissner and R. Ochsenfeld, Naturwissenschaften 21, 787 (1933)
- [20] The Argonne Accelerator History Document Collection, [www.aai.anl.gov/history/project\\_pages/atlas.html](http://www.aai.anl.gov/history/project_pages/atlas.html)
- [21] ATLAS Home Page, [www.phy.anl.gov/atlas/](http://www.phy.anl.gov/atlas/)
- [22] Laboratori Nazional de Legnaro Home Page, [www.lnl.infn.it](http://www.lnl.infn.it)
- [23] TRIUMF National Laboratory Accelerator Physics, [www.triumf.ca/research/research-topics/accelerator-physics](http://www.triumf.ca/research/research-topics/accelerator-physics)
- [24] SPIRAL-2 at GANIL homepage, <http://www.ganil-spiral2.eu/spiral2>
- [25] Stopped and reaccelerated beams at NSCL, [www.nscl.msu.edu/exp/sr](http://www.nscl.msu.edu/exp/sr)
- [26] Soreq Applied Research Accelerator Facility, [http://www.soreq.gov.il/default\\_EN.asp](http://www.soreq.gov.il/default_EN.asp)

- [27] C. Piel et. al., “Phase 1 Commissioning Status of the 40 MeV Proton/Deuteron Accelerator SARAF”, Proceedings of EPAC08, Genoa, Italy, THPP038
- [28] H. Padamsee, J. Knobloch, T. Hayes (2008), “RF Superconductivity for Accelerators, 2nd Edition”, John Wiley and Sons Inc., p. 48
- [29] N. Ida, J.P.A. Bastos, “Electromagnetics and calculation of fields”, Second Edition, Springer Verlag, N.Y., 1996
- [30] S. Humphries, “Finite-Element Methods for Electromagnetics”, [www.fieldp.com/femethods.html](http://www.fieldp.com/femethods.html)
- [31] SolidWorks Corp., Dassault Systems, [www.solidworks.com/default.htm](http://www.solidworks.com/default.htm)
- [32] Developed by Spatial Corporation, [www.spatial.com](http://www.spatial.com)
- [33] ANSYS Inc., [www.ansys.com](http://www.ansys.com)
- [34] CST Computer Simulation Technology AG, [www.cst.com](http://www.cst.com)
- [35] AWR Corp., [www.awrcorp.com](http://www.awrcorp.com)
- [36] ANSYS HFSS, [www.ansoft.com/products/hf/hfss](http://www.ansoft.com/products/hf/hfss)
- [37] Advanced Computations Department, SLAC National Accelerator Laboratory, [https://slacportal.slac.stanford.edu/sites/ard\\_public/acd/Pages/Default.aspx](https://slacportal.slac.stanford.edu/sites/ard_public/acd/Pages/Default.aspx)
- [38] W. Hartung, “LEP 1500 Plans Collapse and Other Stories or What I Learned on my CERN Vacation,” Report NS/RF-92-1701, National Superconductor, 160000 Lincoln Avenue, Brentwood, Colorado 80523 (1992).
- [39] W. Hartung and E. Haebel, “In Search of Trapped Modes in the Single-Cell Cavity Prototype for CESR-B,” Proceedings of the 1993 Particle Accelerator Conference, Washington, D.C., May 1993, Vol. 2, pp. 898-900.
- [40] V. Zvyagintsev, et. al., “SCRF Development at TRIUMF”, RUPAC 2010, Protvino, Russia
- [41] H. Padamsee (2009), “RF Superconductivity: Volume II: Science, Technology, and Applications”, John Wiley and Sons Inc.

- [42] SRF2011, [conferences.fnal.gov/srf2011](http://conferences.fnal.gov/srf2011), 15th International Conference of RF Superconductivity, July 25-29, 2011, Chicago IL, USA
- [43] J.C. Slater, "Microwave Electronics", D. Van Nostrand Company, New York, 1950, pp. 80-81.
- [44] "Handbook of Accelerator Physics and Engineering", edited by A. Chao and M. Tigner, 3rd Printing (2006), World Scientific Publishing Co. Pte. Ltd., p. 580
- [45] M. Grecki et. al., "Compensation of Lorentz Force Detuning for SC Linacs (with Piezo Tuners)", Proceedings of EPAC08, Genoa, Italy, MOPP129
- [46] R. Carcagno et. al., "First Fermilab Results of SRF Cavity Lorentz Force Detuning Compensation Using a Piezo Tuner", Proceedings of SRF2007, Peking University, Beijing, China, TUP57
- [47] H. Padamsee, J. Knobloch, T. Hayes (2008), "RF Superconductivity for Accelerators, 2nd Edition", John Wiley and Sons Inc., p. 120
- [48] T. Powers, "Theory and Practice of Cavity RF Test Systems", Technical Document, Thomas Jefferson National Accelerator Facility
- [49] L. Ge et. al., "Multipacting Simulation and Analysis for the FRIB Superconducting Resonators Using TRACK-3P", Proceeding of LINAC10, Tsukuba, Japan, September 12 - 17, 2010, THP092
- [50] R.L. Geng, "Multipacting Simulations for Superconducting Cavities and RF Coupler Waveguides", Proceedings of the 2003 Particle Accelerator Conference, Portland, OR, May 12-16, 2003
- [51] K. Saito, "Cavity Preparation", Lecture notes from ILC School 2009
- [52] J. Popielarski, FRIB, Private Communications, November, 2011